

**UNIVERSIDAD DE INVESTIGACIÓN DE TECNOLOGÍA
EXPERIMENTAL YACHAY**

Escuela de Ciencias Físicas y Nanotecnología

**TÍTULO: First Principles studies of noble metal (Au, Ag, Pt, Pd)
multicomponent nanoclusters supported on Anatase TiO₂ (101)
surface.**

Trabajo de integración curricular presentado como requisito para la
obtención del título de Ingeniería en Nanotecnología

Autor:

Cedeño Manrique Melanie Alexandra

Tutor:

Prof. Dr. Henry Pinto Esparza.

Co-Tutor:

Prof. Dr. Alicja Mikołajczyk.

Urcuquí, Julio del 2024

AUTORÍA

Yo, **Cedeño Manrique Melanie Alexandra**, con cédula de identidad 1316368487, declaro que las ideas, juicios, valoraciones, interpretaciones, consultas bibliográficas, definiciones y conceptualizaciones expuestas en el presente trabajo; así cómo, los procedimientos y herramientas utilizadas en la investigación, son de absoluta responsabilidad de el/la autora (a) del trabajo de integración curricular. Así mismo, me acojo a los reglamentos internos de la Universidad de Investigación de Tecnología Experimental Yachay.

Urcuquí, Julio del 2024.

Melanie Alexandra Cedeño Manrique
CI: 1316368487

AUTORIZACIÓN DE PUBLICACIÓN

Yo, **Cedeño Manrique Melanie Alexandra**, con cédula de identidad 1316368487, cedo a la Universidad de Investigación de Tecnología Experimental Yachay, los derechos de publicación de la presente obra, sin que deba haber un reconocimiento económico por este concepto. Declaro además que el texto del presente trabajo de titulación no podrá ser cedido a ninguna empresa editorial para su publicación u otros fines, sin contar previamente con la autorización escrita de la Universidad.

Asimismo, autorizo a la Universidad que realice la digitalización y publicación de este trabajo de integración curricular en el repositorio virtual, de conformidad a lo dispuesto en el Art. 144 de la Ley Orgánica de Educación Superior

Urcuquí, Julio del 2024.

Melanie Alexandra Cedeño Manrique
CI: 1316368487

Dedication

To Helen, Jorge, Mariela, and Alfredo. This thesis is dedicated to you, with deep gratitude and love.

Acknowledgements

Me resulta difícil expresar con palabras lo agradecida que estoy con Yachay Tech por despertar en mí la pasión por la ciencia, pero sobre todo me haberme dado el regalo de conocer personas maravillosas que me inspiran cada día.

Este trabajo está dedicado a las personas más importantes de mi vida, mis padres Helen y Jorge, con la esperanza de haber logrado plasmar aquí un poco de lo que han sembrado en mí. A mi mami Helen, quien es mi mayor ejemplo de valentía y determinación; gracias por tu amor incondicional, por los incontables abrazos que me han calmado en los momentos difíciles y por todos los sacrificios que has hecho para que yo pueda cumplir mis sueños. A mi papi Jorge, por siempre estar para mí, por tus valiosas palabras de aliento que han dejado una huella indeleble en mi corazón, por ser mi alarma todos los días durante los últimos años, pero sobre todo, por ser el padre perfecto para mí. Los amo, admiro y llevo conmigo donde quiera que voy.

A mi mami Mariela, Narcisa y Rosalyn, por ser pilares fundamentales y acompañarme en cada etapa de mi vida. A Sergio, Gina y Dayana, por su cariño y apoyo incondicional.

A mis hermanos Naomi y Miguel Ángel, quienes me han regalado los mejores y más especiales momentos. Naomi, no hay palabras suficientes para describir todo lo que significas para mí. Eres mi fuente de inspiración, mi calma y mi tesoro más valioso. Gracias por ser mi mejor amiga, por compartir mis sueños y por ayudarme a cumplirlos, incluso cuando la distancia nos separa. Miguel, tu compañía ha sido un regalo invaluable a lo largo de estos años y ha hecho más bonita mi existencia. A los dos, les dedico este trabajo y les agradezco por toda la felicidad que han traído a mi vida.

A todos con quienes tuve el privilegio de coincidir en esta travesía, quiero agradecerles por sus palabras de aliento y por demostrarme con acciones que este camino no se construye solo. A los amigos que se convirtieron en familia: Guido, Jerry, Alejandro, Cristian Ch., Eder, Francis, Sasha, Mafer y Lennys. Con especial cariño, a Fernando Vega, cuya presencia hizo que estos años sean memorables.

Quiero expresar mi más profundo agradecimiento al Dr. Henry Pinto por haber confiado en mí e introducirme a este fascinante campo, por ser un mentor excepcional y un gran amigo. De la misma manera, agradezco a la Dra. Alicja Mikołajczyk por permitirme ser parte de este proyecto y por mostrarme, con su ejemplo, que las mujeres tienen el poder de transformar la ciencia.

Por último, agradezco el generoso apoyo del Task Supercomputer Center de Gdańsk y de la Universidad de Gdańsk por proporcionar los recursos computacionales necesarios para llevar a cabo esta investigación.

Resumen

Recientemente, los nanomateriales multicomponentes basados en TiO_2 (TiO_2 -MCNM) han ganado gran interés entre los materiales fotocatalíticos. Por lo tanto, estudios teóricos y computacionales son cruciales para comprender los mecanismos implicados. En este trabajo, se analiza la estructura electrónica y propiedades de adsorción de clústeres multicomponentes de metales nobles y su interacción con la superficie Anatasa $TiO_2(101)$ combinando métodos ab initio de Density Functional Theory (DFT) y de Density-Functional Tight-Binding (DFTB). Se simulan sistemas con clústeres monocomponentes y multicomponentes de metales nobles (Au, Ag, Pd, Pt) en diferentes composiciones atómicas. También incluyendo el efecto de una vacante superficial de oxígeno. Dentro del marco DFT se emplearon funcionales metal-GGA SCAN y r^2SCAN junto un funcional de densidad no local de van der Waals rVV10. La limitación de la subestimación de la brecha de banda en DFT se abordó utilizando la corrección Hubbard-U (DFT+U, enfoque de Dudarev). En DFTB, se empleó la parametrización semiempírica GFN1-xBT. Los cálculos DFTB muestran que la combinación de metales da lugar a energías de adsorción sinérgicas. Todos los clústeres estudiados se adsorben mediante quimisorción, y los sistemas que presentan las energías de adsorción más elevadas son los soportados sobre anatasa oxígeno defectuosa. El clúster de Ag se adsorbe más fuertemente a la superficie que el de Pt. Los resultados DFT indican las funciones de trabajo más alta y más baja para los clústeres Au_8Pd_3 y $Au_2Pt_2Ag_2Pd_2$, respectivamente. La transición de banda de semiconductor a metálico sigue la secuencia: $Au_8 > Au_8Pd_3 > Pd_{11} > Au_2Pt_2Ag_2Pd_2$.

Palabras Clave: Teoría Funcional de la Densidad, Método de Enlace Fuerte, Anatasa, Adsorción, clústeres multicomponentes.

Abstract

Recently, TiO_2 -based Multicomponent Nanomaterials (TiO_2 -MCNMs) have gained significant interest as photocatalytic materials. Therefore, theoretical and computational studies of the energetic descriptors are crucial to understanding the mechanisms involved. In the present work, we analyzed the electronic structure and adsorption properties of selected noble metal multicomponent clusters and their interaction with Anatase $TiO_2(101)$ surface by using a cutting-edge combination of ab initio Density Functional Theory (DFT) and Density-Functional Tight-Binding (DFTB) methods. Systems with single and multicomponent clusters of noble metals (Au, Ag, Pd, Pt) at different atomic compositions are considered. The effect of an oxygen surface vacancy was also included. The DFT calculations employed state-of-the-art functionals like metal-GGA SCAN and r^2SCAN combined with a non-local van der Waals density functional rVV10 that accounts for dispersion interactions. Moreover, the known limitation of the band gap underestimation in DFT was addressed using the Hubbard-U correction (DFT+U, within Dudarev's approach). For DFTB implementation, a semi-empirical GFN1-xBT parametrization was employed. DFTB calculations show that combining metals results in synergistic adsorption energies. All studied clusters are adsorbed via chemisorption, with the systems exhibiting the highest adsorption energies being those supported on oxygen-defective anatase. The Ag cluster binds more tightly to the surface than the Pt cluster, reducing desorption. DFT results indicate the highest and lowest work functions for the Au_8Pd_3 and $Au_2Pt_2Ag_2Pd_2$ clusters, respectively. The band gap transition from semiconductor to metallic follows the sequence: $Au_8 > Au_8Pd_3 > Pd_{11} > Au_2Pt_2Ag_2Pd_2$.

Keywords: Density Functional Theory, Density Functional Tight Binding, Anatase, Adsorption, multicomponent clusters.

Contents

List of Figures	9
List of Tables	12
List of Papers	13
1 Introduction	1
1.1 Problem Statement	2
1.2 General and Specific Objectives	3
2 Theoretical Background	4
2.1 Many-body Schrödinger Equation	4
2.2 The Born-Oppenheimer (BO) approximation	6
2.2.1 Atomic Units	7
2.3 Foundations of Density Functional Theory (DFT)	8
2.3.1 Thomas-Fermi Theory	9
2.3.2 Hohenberg-Kohn (HK) Theorem	10
2.3.2.1 First Hohenberg-Kohn Theorem	10
2.3.2.2 Second Hohenberg-Kohn Theorem	11
2.3.3 Kohn-Sham Equations	11
2.3.4 Exchange-Correlation Functionals	13
2.3.4.1 The Local Density Approximation (LDA)	14
2.3.4.2 The Generalized Gradient Approximation (GGA)	15
2.3.4.3 Meta-Generalized Gradient Approximation (meta-GGA)	15
2.3.4.4 Hybrid Functionals	17
2.4 Hubbard-corrected DFT (DFT + U)	17
2.5 Density functional Tight Binding (DFTB)	18
2.6 Vienna <i>ab initio</i> Simulation Package (VASP)	19
2.6.1 Plane-waves basis set	19

2.6.2	Pseudopotentials	20
2.6.3	The Projector Augmented-Wave (PAW) Method	21
2.6.3.1	PAW vs. Ultrasoft pseudopotentials (US-PP)	21
2.7	DFTB+ Code	22
3	Methodology	23
3.1	Input Structures	23
3.2	VASP computational implementation	24
3.2.1	Optimal Parameters for Bulk A- TiO_2	24
3.2.1.1	Cut-off Energy (E_{cut})	24
3.2.1.2	K-points Sampling	25
3.2.1.3	Birch-Murnaghan Equation of State	25
3.2.2	Hubbard U correction	27
3.2.3	A- $TiO_2(101)$ - $c(4 \times 2)$ supercell	29
3.3	DFTB+ computational implementation	30
3.4	Oxygen defective A- $TiO_2(101)$ surface	31
3.5	Cluster@A- $TiO_2(101)$ construction	32
3.6	Density of States (DOS) and Partial Density of States (PDOS)	33
3.7	Adsorption energies ΔE_{Ads}	33
3.8	Work function	34
4	Results & Discussion	35
4.1	Bulk Anatase- TiO_2	35
4.2	DFTB+ simulations	39
4.2.1	Pristine A- $TiO_2(101)$ - $c(4 \times 2)$	39
4.2.2	Oxygen defective A- $TiO_2(101)$ - $c(4 \times 2)$	40
4.2.3	Single-Metal nanoclusters@A- $TiO_2(101)$	42
4.2.4	Single-Metal nanoclusters@A- $TiO_2(101)$ + V_{O-sur}	46
4.2.5	Multicomponent nanoclusters@Anatase $TiO_2(101)$	51
4.3	DFT simulations	58
4.3.1	SCAN functional-based calculations	58
4.3.2	r^2 SCAN functional-based calculations	61
5	Conclusions & Outlook	65
A	Short Appendix 1 Heading for the Table of Contents	66
	Bibliography	73

List of Figures

2.1	Self-consistent iterative method for solving KS equations. Adapted from Ref. ¹	13
3.1	Input crystal structures: a) primitive cell, and b) unit cell of a body-centered tetragonal (BCT) $A\text{-TiO}_2$ (space group $I4_1/amd$). Visualization was performed using VESTA software ²	23
3.2	Cut off energy convergence test computed with SCAN+rVV10 functional for $400 \leq E_{cut}(eV) \leq 900$. Convergence within 1meV/atom is reached at $E_{cut} = 700$	24
3.3	k-point convergence test computed with SCAN+rVV10 functional for $0.033 \leq \Delta k (\text{\AA}^{-1}) \leq 0.044$. Chosen k-point density was $\Delta k = 0.040 \text{\AA}^{-1}$	25
3.4	Birch-Murnaghan EOS for the mass of $A\text{-TiO}_2$: the solid line is equation (3.1) fitted from data calculated with the SCAN+rVV10 functional.	26
3.5	Birch-Murnaghan EOS for the mass of $A\text{-TiO}_2$: the solid line is equation (3.1) fitted from data calculated with the r^2 SCAN+rVV10 functional.	26
3.6	Hubbard correction vs Band Gap for $U=1-7$ using SCAN+rVV10 functional. The dashed red line indicates the experimental band gap for $A\text{-TiO}_2$ ³	27
3.7	Hubbard correction vs Band Gap for $U=1-7$ using r^2 SCAN+rVV10 functional. The dashed red line indicates the experimental band gap for $A\text{-TiO}_2$ ³	28
3.8	Modeling procedure for $A\text{-TiO}_2(101)$. It starts with a) a fully relaxed primitive cell, followed by b) imposition of the (101) plane. Next, a-c) slab model of the $A\text{-TiO}_2(101)$ surface with a vacuum of 20\AA is constructed.	29
3.9	a) Original $A\text{-TiO}_2(101)-(1 \times 1)$ unit cell, b) replicate unit cell twice in x direction and four-times in y-axis to obtain a $c(4 \times 2)$ supercell, c) solid blue line refers to the $c(4 \times 2)$ supercell used in this work.	30
3.10	Supercell $A\text{-TiO}_2(101)-c(4 \times 2)$ relaxed by the GFN1-xTB method from a) Top view of its outermost layer, and b) Side view. The atoms selected in yellow (bottom O-Ti-O layer) indicate that they are fixed, similar to the case of the structure calculated by DFT.	31
3.11	Introduction of the surface oxygen vacancy in the $A\text{-TiO}_2(101)-c(4 \times 2)$. The label V_{O-sur} indicates the position of the vacancy.	32
3.12	Structural convergence achieved for the Au8 cluster, viewed from different coordinate planes.	32
4.1	Bulk unit cell of Anatase TiO_2 after relaxation using SCAN+rVV10+U functional.	35

4.2	Partial Density of States (PDOS) of Bulk Anatase TiO_2 after relaxation using SCAN+rVV10+U functional.	38
4.3	Partial Density of States (PDOS) of Bulk Anatase TiO_2 after relaxation using r^2 SCAN+rVV10+U functional.	38
4.4	Partial Density of States (PDOS) of Bulk Anatase TiO_2 after relaxation using GFN1-xBT functional.	39
4.5	(a) Top view of the outermost layer and side view of the fully relaxed supercell. (b) Partial Density of States (PDOS) of pristine A- $TiO_2(101)-c(4 \times 2)$ using xBT method.	40
4.6	(a) Top view of the outermost layer and side view of the fully relaxed supercell. (b) Partial Density of States (PDOS) of oxygen defective A- $TiO_2(101)-c(4 \times 2)$ using xBT method. The dashed blue line indicates the introduction of new localized states close to the Fermi level.	41
4.7	(a) Top view of the outermost layer and side view of the optimized geometry. (b) Partial Density of States (PDOS) of Au_8 cluster supported on stoichiometric A- $TiO_2(101)-c(4 \times 2)$	42
4.8	(a) Top view of the outermost layer and side view of the optimized geometry. (b) Partial Density of States (PDOS) of Ag_8 cluster supported on stoichiometric A- $TiO_2(101)-c(4 \times 2)$	44
4.9	(a) Top view of the outermost layer and side view of the optimized geometry. (b) Partial Density of States (PDOS) of Pd_8 cluster supported on stoichiometric A- $TiO_2(101)-c(4 \times 2)$	45
4.10	(a) Top view of the outermost layer and side view of the optimized geometry. (b) Partial Density of States (PDOS) of Pt_8 cluster supported on stoichiometric A- $TiO_2(101)-c(4 \times 2)$	46
4.11	(a) Top view of the outermost layer and side view of the optimized geometry. (b) Partial Density of States (PDOS) of Au_8 cluster supported on oxygen defective A- $TiO_2(101)-c(4 \times 2)$	47
4.12	(a) Top view of the outermost layer and side view of the optimized geometry. (b) Partial Density of States (PDOS) of Ag_8 cluster supported on oxygen defective A- $TiO_2(101)-c(4 \times 2)$	48
4.13	(a) Top view of the outermost layer and side view of the optimized geometry. (b) Partial Density of States (PDOS) of Pd_8 cluster supported on oxygen defective A- $TiO_2(101)-c(4 \times 2)$	49
4.14	(a) Top view of the outermost layer and side view of the optimized geometry. (b) Partial Density of States (PDOS) of Pt_8 cluster supported on oxygen defective A- $TiO_2(101)-c(4 \times 2)$	50
4.15	(a) Top view of the outermost layer and side view of the optimized geometry. (b) Partial Density of States (PDOS) of bimetallic Pd_4Ag_4 cluster supported on oxygen defective A- $TiO_2(101)-c(4 \times 2)$	52
4.16	(a) Top view of the outermost layer and side view of the optimized geometry. (b) Partial Density of States (PDOS) of bimetallic Pt_4Pd_4 cluster supported on oxygen defective A- $TiO_2(101)-c(4 \times 2)$	53
4.17	(a) Top view of the outermost layer and side view of the optimized geometry. (b) Partial Density of States (PDOS) of trimetallic $Au_2Ag_2Pd_2$ cluster supported on oxygen defective A- $TiO_2(101)-c(4 \times 2)$	54
4.18	(a) Top view of the outermost layer and side view of the optimized geometry. (b) Partial Density of States (PDOS) of trimetallic $Pd_2Pt_2Ag_2$ cluster supported on oxygen defective A- $TiO_2(101)-c(4 \times 2)$	55
4.19	(a) Top view of the outermost layer and side view of the optimized geometry. (b) Partial Density of States (PDOS) of tetra metallic $Au_2Pt_2Ag_2Pd_2$ cluster supported on oxygen defective A- $TiO_2(101)-c(4 \times 2)$	56
4.20	Partial Density of States (PDOS) of A- $TiO_2(101)-c(4 \times 2)$ computed with SCAN+rVV10+U.	59

4.21	(a) Top view of the outermost layer and side view of the optimized geometry. (b) Partial Density of States (PDOS) of Au_8 cluster supported on oxygen defective $A-TiO_2(101)-c(4 \times 2)$ computed with SCAN+rVV10+U.	59
4.22	Planar average potential plot derived from the local potential of the $Au_8@A-TiO_2(101)-c(4 \times 2)+V_{O-sur}$ system calculated using SCAN+rVV10+U functional.	60
4.23	(a) Top view of the outermost layer and side view of the optimized geometry. (b) Partial Density of States (PDOS) of tetrametallic $Au_2Pt_2Ag_2Pd_2$ cluster supported on oxygen defective $A-TiO_2(101)-c(4 \times 2)$ computed with SCAN+rVV10+U.	60
4.24	Planar average potential plot derived from the local potential of the $Au_2Pt_2Ag_2Pd_2@A-TiO_2(101)-c(4 \times 2)+V_{O-sur}$ system calculated using SCAN+rVV10+U functional.	61
4.25	Partial Density of States (PDOS) of $A-TiO_2(101)-c(4 \times 2)$ computed with r^2 SCAN+rVV10+U.	62
4.26	(a) Top view of the outermost layer and side view of the optimized geometry. (b) Partial Density of States (PDOS) of Pd_{11} cluster supported on oxygen defective $A-TiO_2(101)-c(4 \times 2)$ computed with r^2 SCAN+rVV10+U.	62
4.27	Planar average potential plot derived from the local potential of the $Pd_{11}@A-TiO_2(101)-c(4 \times 2)+V_{O-sur}$ system calculated using r^2 SCAN+rVV10+U functional.	63
4.28	(a) Top view of the outermost layer and side view of the optimized geometry. (b) Partial Density of States (PDOS) of Au_8Pd_3 cluster supported on oxygen defective $A-TiO_2(101)-c(4 \times 2)$ computed with r^2 SCAN+rVV10+U.	63
4.29	Planar average potential plot derived from the local potential of the $Au_8Pd_3@A-TiO_2(101)-c(4 \times 2)+V_{O-sur}$ system calculated using r^2 SCAN+rVV10+U functional.	64
A.1	Detailed orbital resolved PDOS for Bulk Anatase TiO_2 computed with r^2 SCAN+rVV10+U functional.	69
A.2	Detailed orbital resolved PDOS for Bulk Anatase TiO_2 computed with SCAN+rVV10+U functional.	72

List of Tables

2.1	“Jacob’s ladder” for exchange-correlation functionals adapted from ^{4,5}	14
2.2	List of the 17 SCAN exact constraints arranged by novelty. Adapted from ⁶	16
3.1	Optimal Volume (V_0), Bulk Modulus (B_0), and Band Gap for A- <i>TiO</i> ₂ with Hubbard correction U=1-7 using SCAN+rVV10 functional.	28
3.2	Optimal Volume (V_0), Bulk Modulus (B_0), and Band Gap for A- <i>TiO</i> ₂ with Hubbard correction U=1-7 using r^2 SCAN+rVV10 functional.	29
4.1	Crystallographic and electronic structure data for Bulk Anatase <i>TiO</i> ₂ . In this table, a, b, and c are the lattice parameters, and E_{bg} indicates the computed band gap. The angles of the unit cell are $\alpha = \beta = \gamma = 90^\circ$	36
4.2	Energetic properties for cluster@A- <i>TiO</i> ₂ (101)-c(4×2) systems computed with DFTB xBT Hamiltonian.	57
4.3	Energetic properties for cluster@A- <i>TiO</i> ₂ (101)-c(4×2) systems computed with DFT SCAN/ r^2 SCAN+rVV10+U functionals.	64

Chapter 1

Introduction

Over recent decades, TiO_2 -based materials have been the subject of great attention in materials engineering. This growing interest is driven by their ability to efficiently catalyze a variety of reactions under light irradiation, their chemical stability and recoverability⁷, which make them the suitable candidates for applications in advanced environmental technology and energy-related areas, including water splitting for hydrogen production⁸, photocatalytic CO_2 conversion into added-value fuels⁹, Advanced Oxidation Processes (AOPs) for wastewater treatment¹⁰, gas sensing¹¹, solar cells¹² and more.

Extensive research, from both experimental and computational approaches, has been conducted on Bare TiO_2 particularly focusing on Anatase and other relevant polymorphs such as Brookite and Rutile^{13,14}. These studies have provided valuable information on their physical and chemical properties, revealing key features such as crystal structure, electronic configuration, optical responses, and surface reactivity^{15,16}. Based on the evidence from theoretical and chemisorption investigations, it is generally accepted that TiO_2 anatase shows higher photocatalytic activity. From the description of the electronic properties of anatase, this can be explained mainly by its classification as an indirect energy gap semiconductor and by the presence of a lighter effective mass compared to the other polymorphs already mentioned. This suggests a longer charge carrier lifetime and a faster migration of photogenerated electrons and holes to the catalyst's surface^{17,18}. However, few studies have reported that brookite outperforms the photocatalytic efficiency of anatase and rutile in heterogeneous photocatalytic systems. Still, it has received less interest given the complex synthesis procedure, and the difficulty of obtaining single-phase brookite¹⁹.

The surface plays a key role in the charge carrier transfer and adsorption processes for photocatalytic reactions. Therefore, the choice of the crystalline facet of the exposed surface and its reactivity/affinity with the specific molecule involved will affect the overall performance of the catalyst. Anatase TiO_2 crystals are typically dominated by (101) facets, which have been reported as the most thermodynamically stable, exhibiting lower surface energy compared to other low-index facets^{20,21}. In particular, it has been observed that the photocatalytic activity for the degradation of Rhodamine B (RhB) in the liquid phase is higher for Anatase TiO_2 (101) with respect to the (010) surface. Similarly, in the gaseous phase, the photoreduction of CO_2 to CH_4 is enhanced when exposed to (101) surface compared to (001)²².

The main drawbacks of unmodified TiO_2 as a photocatalyst are the fast recombination of electron-hole pairs and its wide band gap (3.2 eV for Anatase according to experimental data³), which limits the available active charge carriers for chemical transformations and restricts the activation region to the ultraviolet (UV) light spectrum, preventing full exploitation of the solar radiation spectrum. To overcome these shortcomings, several modification strategies have been implemented²³, including (i) metal and non-metal doping^{24,25}, (ii) co-catalyst loading²⁶, (iii) heterojunction formation²⁷, (iv) dye-sensitization²⁸, and (v) introduction of point defects (e.g. titanium or oxygen vacancies)²⁹.

Thereby, surface-modified TiO_2 -based nano-photocatalysts, belonging to the category of second-generation nanoparticles^{30,31}, have proven to be promising materials with unique physicochemical features and efficient reactivity under visible light ($\lambda > 400\text{nm}$) in both gas and liquid phases.

In advanced nanomaterials, the introduction of multicomponent nanomaterials (MCNMs) represents a ground-breaking frontier to be explored. These materials are hybrid structures composed of two or more functional nanoscale components of different compositions that can exhibit improved properties compared to their single-component counterparts. TiO_2 -based multicomponent nanomaterials are showing promising results, especially in improving photocatalytic performance, surpassing the capabilities of traditional unmodified TiO_2 . This is achieved by tuning the electronic properties through synergistic effects from including other catalytically active species^{32,33}. However, the range of possible compositional combinations is nearly unlimited, making evaluating their efficacy by experimental testing impractical. To address this challenge, the use of computational tools emerges as a valuable strategy for optimizing the preliminary design of these materials; techniques such as ab initio modelling³⁴ and machine learning algorithms³⁵ have the ability to provide crucial insights for informed decision-making in the development of advanced materials.

Density Functional Theory (DFT) is a first-principles method based on quantum mechanics that has demonstrated high accuracy in predicting atomistic-level properties such as electronic structure, energetics, and structural information, with significant advantages in terms of computational speed³⁶. Its widespread use in the scientific literature³⁷ highlights the role of DFT as a key tool to address open questions in the research of novel complex materials, particularly those in the unexplored field of MCNMs.

1.1 Problem Statement

Developing advanced materials is essential for improving sustainable environmental and energy technologies. One of the most promising transition metal oxides for designing next-generation photocatalysts is TiO_2 ³⁸. Although TiO_2 modified with single-metal nanomaterials (NMs) has achieved great photocatalytic performance, they may have some drawbacks in terms of chemical and thermal stability³⁹. Therefore, the transition to TiO_2 modified with hybrids of equal or more than 2 types of metals has attracted great attention as an attempt to explore novel approaches to obtain high-performance materials.

Given their synergistic nature, TiO_2 -based multicomponent nanomaterials face several interesting challenges, with many possibilities to be explored. Among them, the investigation of TiO_2 surface-modified with noble metal multicomponent nanoclusters (Au, Ag, Pt, Pd) could serve as a starting point to delve into systems with a higher

degree of complexity than those already studied. Understanding the electronic structure and adsorption properties through computational approaches is desirable for the preliminary design of these materials, allowing the screening of a wide variety of potential combinations that would be unfeasible using experimental methods alone. However, detailed studies on the combined effect of noble metals on the energetic properties and their interaction with Anatase TiO_2 (101) surface are currently lacking, hindering a deeper understanding of the fundamental mechanisms governing its catalytic behavior. In addition, it is not well understood how oxygen vacancies may influence the multicomponent cluster morphology and the overall electronic structure.

Consequently, the existing gap in the literature suggests the need to employ state-of-the-art computational methods to provide insights into synergistic effects in TiO_2 -based multicomponent nanomaterials.

1.2 General and Specific Objectives

The present study aims to conduct ab initio calculations using density-functional theory (DFT) to investigate the structural and electronic properties of selected mono-, bi-, tri-, and tetra- metallic nanoclusters supported on both stoichiometric and oxygen-defective Anatase TiO_2 (101) surface. To fulfill this goal, the following specific objectives will be addressed:

- Describe the theoretical basis of DFT, covering the fundamentals of the meta-GGA functionals r²SCAN and SCAN.
- Perform geometry relaxations on bulk Anatase TiO_2 and model the (101) $c(4 \times 2)$ supercell considering Hubbard U corrections.
- Optimize cluster@Anatase $TiO_2(101)$ systems using density functional tight-binding (DFTB).
- Compute the proposed systems' electronic structure considering stoichiometric and oxygen-defective Anatase $TiO_2(101)$ surfaces.
- Analyze the adsorption properties of each configuration and assess the influence of noble metals on the overall energetic properties.
- Calculate the vacuum potential and work function of selected systems employing DFT.

Chapter 2

Theoretical Background

The following chapter introduces the fundamental concepts of quantum mechanics that will serve as the basis for a deeper understanding of the formalisms underlying the first-principles methods used in this research.

2.1 Many-body Schrödinger Equation

Solid materials, at the atomic scale, can be thought of as a collection of electrons and nuclei interacting with each other to form the crystal structure, and it is widely recognized that many of their intrinsic macroscopic properties are governed by their electronic structure⁴⁰.

When restricted to stationary electronic states in a non-relativistic frame, it is necessary to consider the time-independent Schrödinger equation to provide a quantum description of the system⁴¹:

$$\hat{H}\psi = E\psi \quad (2.1)$$

In this equation, \hat{H} represents the Hamiltonian operator that includes the information of both Kinetic (\hat{T}) and Potential (\hat{V}) contributions, and E is the energy eigenvalue associated to the wavefunction ψ that depends on the particle position.

Assuming a system with N electrons and M nuclei, the coordinates will be r_1, r_2, \dots, r_N and R_1, R_2, \dots, R_M , respectively. Since the many-body wave function Ψ is defined in terms of the positions of the electrons and the nuclei, it can be written as

$$\Psi = \Psi(r_1, r_2, \dots, r_N; R_1, R_2, \dots, R_M) \quad (2.2)$$

Therefore, the equation (2.1) can now be expressed as

$$\hat{H}\Psi = (\hat{T} + \hat{V})\Psi = E_{tot}\Psi \quad (2.3)$$

where E_{tot} is the system's total energy. The kinetic energy \hat{T} is described by the contribution of the kinetic energy of the electrons \hat{T}_e and the nuclei \hat{T}_n :

$$\hat{T} = \hat{T}_e + \hat{T}_n = - \sum_{i=1}^N \frac{\hbar^2}{2m_e} \nabla_i^2 - \sum_{I=1}^M \frac{\hbar^2}{2M_I} \nabla_I^2 \quad (2.4)$$

In this expression, m_e is the electron mass, M_I is the mass of the I -th nuclei, and ∇^2 stands for the Laplacian operator acting with respect to each particle. For instance, if the Laplace operator is acting on the coordinates of the i -th particle, we have:

$$\nabla_i^2 = \frac{\partial^2}{\partial x_i^2} + \frac{\partial^2}{\partial y_i^2} + \frac{\partial^2}{\partial z_i^2} \quad (2.5)$$

Given that we are dealing with electrically charged particles, electrostatic or Coulombic interactions must be taken into account when defining the total potential energy \hat{V} :

1. *Electron-electron repulsive interaction, $\hat{V}_{(e-e)}$*

$$\hat{V}_{(e-e)} = \frac{1}{2} \sum_{i \neq j} \frac{e^2}{4\pi\epsilon_0} \frac{1}{|r_i - r_j|} \quad (2.6)$$

2. *Electron-nuclei attractive interaction, $\hat{V}_{(e-n)}$*

$$\hat{V}_{(e-n)} = - \sum_{i,I} \frac{e^2}{4\pi\epsilon_0} \frac{Z_I}{|r_i - R_I|} \quad (2.7)$$

3. *Nuclei-nuclei repulsive interaction, $\hat{V}_{(n-n)}$*

$$\hat{V}_{(n-n)} = \frac{1}{2} \sum_{I \neq J} \frac{e^2}{4\pi\epsilon_0} \frac{Z_I Z_J}{|R_I - R_J|} \quad (2.8)$$

where e is the electron charge, ϵ_0 is the vacuum permittivity, and $Z_{I(J)}$ accounts for the atomic number of the I -th (J -th) nuclei.

Then, using equations (2.6), (2.7) and (2.8), we can obtain the overall expression for the potential energy \hat{V} as follows

$$\hat{V} = \hat{V}_{(e-e)} + \hat{V}_{(e-n)} + \hat{V}_{(n-n)} = \frac{1}{2} \sum_{i \neq j} \frac{e^2}{4\pi\epsilon_0} \frac{1}{|r_i - r_j|} - \sum_{i,I} \frac{e^2}{4\pi\epsilon_0} \frac{Z_I}{|r_i - R_I|} + \frac{1}{2} \sum_{I \neq J} \frac{e^2}{4\pi\epsilon_0} \frac{Z_I Z_J}{|R_I - R_J|} \quad (2.9)$$

Finally, by replacing equations (2.4) and (2.9) in (2.3), the complete description of the many-body Schrödinger equation is obtained:

$$\left[- \sum_i^N \frac{\hbar^2}{2m_e} \nabla_i^2 - \sum_I^M \frac{\hbar^2}{2M_I} \nabla_I^2 + \frac{1}{2} \sum_{i \neq j} \frac{e^2}{4\pi\epsilon_0} \frac{1}{|r_i - r_j|} - \sum_{i,I} \frac{e^2}{4\pi\epsilon_0} \frac{Z_I}{|r_i - R_I|} + \frac{1}{2} \sum_{I \neq J} \frac{e^2}{4\pi\epsilon_0} \frac{Z_I Z_J}{|R_I - R_J|} \right] \Psi = E_{tot} \Psi \quad (2.10)$$

The equation (2.10) contains fundamental physical constants and nearly all the information needed to analyze systems in equilibrium from a first principle approach, but a rigorous description would incorporate more complex considerations such as time dependence, external electromagnetic field interactions, and relativistic corrections⁴². In addition, it is important to note that analytically solving the many-body Schrödinger equation becomes computationally demanding as the size of the system increases; this is commonly referred to as the "exponential wall" since the number of possible configurations, and hence matrix operations, grows exponentially with the increase in the number of electrons involved⁴³.

Attempts to overcome this challenge have resulted in several approaches to solve the equation (2.10), such as the mean-field approximation, the Hartree-Fock (HF) method, and the Born-Oppenheimer (BO) approximation, the latter being one of the most important approximations within the condensed matter field.

2.2 The Born-Oppenheimer (BO) approximation

The basic assumption of the Born-Oppenheimer approximation, also known as the adiabatic approximation, is that nuclear and electronic motion can be treated as independent mathematical problems on the time scale⁴⁴. This is based on the fact that, given the considerable ratio of atomic to electron mass M_I/m_e (10^4 to 10^5 times larger mass in most atoms), electrons move significantly faster than nuclei and, as a result, any shift in nuclear position causes electrons to adjust instantaneously⁴⁵. In this context, atoms can be pictured as a collection of nuclei moving on a potential energy surface, which is dictated by the influence of the electrons in a certain eigenstate⁴⁶.

It is assumed that the electrons remain in their lowest energy configuration and that the positions of the nuclei are 'fixed' (nearly stationary due to the uncertainty principle). Thus, the adiabatic potential energy surface of the atom will be given by the ground state energy, which is a function of the positions of the nuclei, $E(R_1, R_2, \dots, R_M)$.

The total wavefunction can be decoupled as the product of the electron-only wavefunction Ψ_R and the nuclear-only wavefunction χ , such that:

$$\Psi(r_1, \dots, r_N; R_1, \dots, R_M) = \Psi_R(r_1, \dots, r_N)\chi(R_1, \dots, R_M) \quad (2.11)$$

For further discussion regarding the main features of the standard BO approximation, please refer to⁴⁷.

At this point, it is possible to obtain the many-body Schrödinger equation for the nuclei only, but to facilitate manipulation of the expressions, it is convenient to rewrite the equation (2.10) in terms of atomic units.

2.2.1 Atomic Units

In the Hamiltonian definition of the many-body Schrödinger equation, fundamental physical constants that are independent of the material under consideration are included. Specifically⁴⁸,

$$\begin{aligned}
 \hbar &= 1.054571817 \cdot 10^{-34} \text{ J} \cdot \text{s}, \\
 m_e &= 9.109383701 \cdot 10^{-31} \text{ kg}, \\
 m_p &= 1.672621923 \cdot 10^{-27} \text{ kg}, \\
 e &= 1.602176634 \cdot 10^{-19} \text{ C}, \\
 \epsilon_0 &= 8.854187812 \cdot 10^{-12} \text{ F/m}.
 \end{aligned} \tag{2.12}$$

To estimate the natural unit of energy, let us consider the hydrogen atom in its ground state, as described in ref.⁴²; the distance between the electron and the nucleus given by the Bohr radius $a_0 \simeq 0.529 \text{ \AA}$, the angular momentum $\hbar = m_e v a_0$, and the electron-proton pair's Coulomb energy using Hartree is $E_{Ha} = \frac{e^2}{4\pi\epsilon_0 a_0}$. In addition, the kinetic energy in terms of E_{Ha} is defined as:

$$\frac{1}{2} m_e v^2 = \frac{1}{2} E_{Ha} \tag{2.13}$$

And,

$$E_{Ha} = \frac{e^2}{4\pi\epsilon_0 a_0} = m_e v^2 = \frac{\hbar^2}{m_e a_0^2} \tag{2.14}$$

Hence, using results from (2.14) and dividing equation (2.10) by E_{Ha} , the following simplification can be obtained:

$$\left[-\sum_i^N \frac{1}{2} a_0^2 \nabla_i^2 - \sum_I^M \frac{1}{2} \frac{a_0^2}{M_I/m_e} \nabla_I^2 + \frac{1}{2} \sum_{i \neq j} \frac{a_0}{|r_i - r_j|} - \sum_{i,I} Z_I \frac{a_0}{|r_i - R_I|} + \frac{1}{2} \sum_{I \neq J} a_0 \frac{Z_I Z_J}{|R_I - R_J|} \right] \Psi = \frac{E_{tot}}{E_{Ha}} \Psi \tag{2.15}$$

To further simplify the equation, it is advantageous to express the physical constants in terms of Hartree atomic units⁴⁹. In this convention, the set of base units defined by the reduced Planck constant \hbar , the unit length a_0 , the unit charge e , and the unit mass m_e , takes the value of 1. Consequently, the Hartree energy E_{Ha} from the equation (2.14) is also set to one. In this way, equation (2.15) results as:

$$\left[-\sum_i^N \frac{\nabla_i^2}{2} - \sum_I^M \frac{\nabla_I^2}{2M_I} + \frac{1}{2} \sum_{i \neq j} \frac{1}{|r_i - r_j|} - \sum_{i,I} \frac{Z_I}{|r_i - R_I|} + \frac{1}{2} \sum_{I \neq J} \frac{Z_I Z_J}{|R_I - R_J|} \right] \Psi = E_{tot} \Psi \tag{2.16}$$

Referring back to the BO approximation postulate mentioned earlier in this section, it is appropriate to assume that when it comes to the study of solids, the heaviness keeps the nuclei in fixed positions⁵⁰. Consequently, treating the M_I as ∞ implies disregarding the kinetic energy of the nuclei. For further simplification, we can introduce the E term, where the repulsion between nuclei is considered a constant:

$$E = E_{tot} - \frac{1}{2} \sum_{I \neq J} \frac{Z_I Z_J}{|R_I - R_J|} \quad (2.17)$$

Similarly, the attractive electron-nucleus interaction is parameterized as a function only of the electron coordinates,

$$V_n(r) = - \sum_I \frac{Z_I}{|r_i - R_I|} \quad (2.18)$$

Then, equation (2.16) is written as follows:

$$\left[- \sum_i^N \frac{\nabla_i^2}{2} + \frac{1}{2} \sum_{i \neq j} \frac{1}{|r_i - r_j|} + \sum_i V_n(r_{i;R}) \right] \Psi_R = E_R \Psi_R \quad (2.19)$$

Note that the subscript \mathbf{R} denotes the dependence on the nuclear coordinate set. Equations (2.11) and (2.19) are replaced into (2.16), yielding,

$$E_R \Psi_{R\chi} + \left[- \sum_i^N \frac{\nabla_i^2}{2M_I} + \frac{1}{2} \sum_{i \neq j} \frac{Z_I}{|R_I - R_J|} \right] \Psi_{R\chi} = E_{tot} \Psi_{R\chi} \quad (2.20)$$

Furthermore, by multiplying by Ψ_R^* , integrating over the electronic coordinates, and normalizing to unity, the whole equation then results in:

$$\left[- \sum_i^N \frac{\nabla_i^2}{2M_I} + \frac{1}{2} \sum_{i \neq j} \frac{Z_I}{|R_I - R_J|} + E_R \right] \chi = E_{tot} \chi \quad (2.21)$$

In this way, the unfolding of the electronic and nuclear dynamics from the general quantum mechanical description of equation (2.16) is represented by expressions (2.19) and (2.21).

2.3 Foundations of Density Functional Theory (DFT)

Solving the many-body Schrödinger equation is a challenging task; therefore, using specific approximation schemes is advisable. Even if a simplification is achieved using these assumptions, the problem is still mathematically too complex as we are working with $3N$ Cartesian coordinates⁵¹.

Density Functional Theory (DFT) offers an alternate formalism for handling the many-electron problem. This approach emerged between 1964 and 1965 from the pioneering contributions of Hohenberg, Kohn, and Sham^{52,53}. It is based on calculating the ground state energy of a quantum system as a function of the electron density distribution in space $n(r)$ rather than explicitly dealing with the observable many-electron wave function Ψ . The core of DFT is based on two fundamental theorems: the Hohenberg-Kohn theorem and the Kohn-Sham equations, which we will discuss in more detail in this section.

2.3.1 Thomas-Fermi Theory

This semi-classical model (1927) is considered the predecessor of DFT, as it proposed the first idea of electron gas⁵⁴. In this framework, it was established that the kinetic energy is conveniently denoted as a functional of the local density for N electrons.

For the scenario of a homogeneous electron gas with non-interacting electrons under a constant electrostatic potential, the average kinetic energy is defined⁵⁵:

$$E_k(n) = \frac{3}{10}(3\pi^2)^{2/3}n^{2/3} \quad (2.22)$$

When electrons are subjected to slightly fluctuating external potential v_{ext} , i.e., varying slowly in space, the approximate value of their kinetic energy density at a point r is:

$$E_k[n(r)] \approx \int n(r)E_k(r)d^3r = \frac{3}{10}(3\pi^2)^{2/3} \int n^{5/3}(r)d^3r \quad (2.23)$$

For the Coulomb energy, the approximation leads to,

$$E_c[n(r)] = \int n(r)v_{ext}(r)d^3r + \frac{1}{2} \iint \frac{n(r)n(r')}{|r-r'|} d^3r d^3r' \quad (2.24)$$

where the first term represents the electron-nuclei attractive energy and the second is the electron-electron repulsive energy. Hence, the total energy can be written using the Thomas-Fermi functional in the following way:

$$E_{T-F}[n(r)] = E_k[n(r)] + E_c[n(r)] \quad (2.25)$$

The equilibrium ground state can be obtained by minimizing the equation (2.25) with the normalization constraint that conserves the number of electrons in the system⁵⁶,

$$\int n(r)d^3r = N \quad (2.26)$$

As a result, the Thomas-Fermi equation is derived:

$$\frac{1}{2}(3\pi^2)^{2/3}n^{2/3}(r) + v_{ext}(r) + \int \frac{n(r')}{|r-r'|} d^3r' = \mu \quad (2.27)$$

In which μ is the Lagrange multiplier introduced to satisfy condition (2.26). Then, the implicit equation for density is,

$$\rho = \frac{1}{3\pi^2} 2^{3/2} \left(\mu - v_{ext}(r) - \int \frac{n(r')}{|r-r'|} d^3r' \right)^{3/2} \quad (2.28)$$

It is worth mentioning that due to the non-rigorous treatment of the kinetic energy and the absence of explicit terms for exchange-correlation effects, it fails to capture all quantum effects fully and to provide reliable electronic descriptions. Despite its limitations, it is considered an excellent first approximation that laid the groundwork for the transition to more sophisticated and accurate theories⁵⁷.

2.3.2 Hohenberg-Kohn (HK) Theorem

In 1964, Hohenberg and Kohn established two remarkable principles related to existence theorems, which laid the foundations of modern DFT⁵⁸. Briefly, the key insight of the HK theorem is that the ground-state energy is a function of the electron density, where the ground-state wave function and the ground-state electron density are injectively related,

$$E = F[n(r)] \quad (2.29)$$

The following three premises serve as the basis for the justification of this theorem⁴²:

1. The external potential is solely determined by the electron density in the ground state, $n(r) \rightarrow V_{ext}$.
2. For a given external potential, there is a unique associated many-electron wavefunction, $V_{ext} \rightarrow \Psi$.
3. The system's overall energy is a function of the wavefunction, $\Psi \rightarrow E$.

Consequently, the arguments above suggest that the electron density dictates the total energy, $n \rightarrow V_{ext} \rightarrow \Psi \rightarrow E$.

2.3.2.1 First Hohenberg-Kohn Theorem

The first theorem holds that *the ground state density of a system of N electrons uniquely determines all the properties of an electronic system, such as the number of electrons, the external potential, the Hamiltonian, and thus the properties of the ground state*⁵⁹.

The theorem is proved as suggested in reference⁶⁰. Let us start by assuming that the Hamiltonian \hat{H} has a non-degenerate ground state wavefunction Ψ with its corresponding external potential $v_{ext}(r)$, ground state density $n(r)$, and kinetic \hat{T} and electron interaction \hat{U} energy operators. The corresponding energy of the ground state equals,

$$E = \langle \Psi | \hat{H} | \Psi \rangle = \int v_{ext}(r)n(r)d^3r + \langle \Psi | (\hat{T} + \hat{U}) | \Psi \rangle \quad (2.30)$$

Let us now consider a different potential v'_{ext} that leads to the same electron density $n(r)$ as v_{ext} but differs from it by a factor greater than a constant, such that $v'_{ext} \neq v_{ext} + const$. The energy of the ground state is,

$$E' = \langle \Psi' | \hat{H}' | \Psi' \rangle = \int v'_{ext}(r)n(r)d^3r + \langle \Psi' | (\hat{T} + \hat{U}) | \Psi' \rangle \quad (2.31)$$

Based on the Rayleigh-Ritz variational principle for energy⁶¹, we get the inequality:

$$\begin{aligned} E < \langle \Psi' | \hat{H}' | \Psi' \rangle &= \int v_{ext}(r)n(r)d^3r + \langle \Psi' | (\hat{T} + \hat{U}) | \Psi' \rangle \\ &= E' + \int (v_{ext}(r) - v'_{ext}(r))n(r)d^3r \end{aligned} \quad (2.32)$$

Likewise, given that we have not explicitly guaranteed the non-degeneracy for Ψ' , we have :

$$E' \leq \langle \Psi | \hat{H}' | \Psi \rangle = E + \int (v'_{ext}(r) - v_{ext}(r))n(r)d^3r \quad (2.33)$$

Adding equations (2.32) and (2.33) results in a contradiction,

$$E + E' < E + E' \quad (2.34)$$

The first HK theorem is then proved by applying *reductio ad absurdum*, invalidating our initial assumption that the same electron density can be obtained from two different external potentials.

2.3.2.2 Second Hohenberg-Kohn Theorem

According to the second HK Theorem, *the ground-state energy functional $F[n(r)]$, which can be obtained variationally, determines the ground-state density $n(r)$. By minimizing the total energy, this density corresponds to the exact electron distribution of the system¹*. It is possible to write the energy functional as⁶⁰,

$$E[n] = F_{HK}[n] + \int n(r)v_{ext}(r)d^3r \quad (2.35)$$

Where,

$$F_{HK}[n] = \langle \Psi[n] | (\hat{T} + \hat{U}) | \Psi[n] \rangle \quad (2.36)$$

$F_{HK}[n]$ is a universal functional of n -representable densities (same form for all Coulombic systems), and the factors that determine it are the kinetic and electron-electron interaction operators rather than the external potential.

To illustrate how a functional changes with a slight variation, the functional derivative is presented:

$$\delta F = \int \left(\frac{\delta F}{\delta n(r)} \right) \delta n(r) d^3r \quad (2.37)$$

By considering the Lagrangian multiplier for particle conservation from the constraint (2.26), energy minimization can be obtained using the variational principle:

$$\delta \left\{ E[n] - \mu \left[\int n(r) d^3r - N \right] \right\} = 0 \quad (2.38)$$

Yielding the Euler-Lagrange equation for the density,

$$\frac{\delta E[n]}{\delta n(r)} = v_{ext}(r) + \frac{\delta F_{HK}[n]}{\delta n[r]} = \mu \quad (2.39)$$

Even though $F_{HK}[n(r)]$ has a formal definition found in equation (2.36), the explicit density-dependent functional form is unknown and needs to be estimated. Equation (2.39) can be satisfied by an approximate $F_{HK}[n(r)]$, so the corresponding solutions are estimates of the actual density of the system. Thus, the accuracy will depend on the functional used⁵⁵.

2.3.3 Kohn-Sham Equations

Practical implementations of the Hohenberg-Kohn principles were made possible by the Kohn-Sham (KS) approach. This implementation assumes that the kinetic energy can be mapped as a function of single-particle orbitals. Suppose

the interacting electron system described previously is considered an auxiliary system of independent electrons with the same ground-state charge density as the real interacting electron system. In that case, the system can be simplified considerably⁶². Since KS-DFT is generally more accurate than orbital-free DFT, it is regarded as one of the most widespread electronic structure approximations⁶³.

The density is computed from a single Slater determinant of the non-interacting system, and an approximation to the kinetic energy of the actual interacting system is evaluated from the spin orbitals of this determinant similarly as the kinetic energy is computed in wave function theory⁶⁴.

Functional $F_{HK}[n(r)]$ can be split into^{65,66},

$$F_{HK}[n(r)] = T_s[n(r)] + E_H[n(r)] + E_{XC}[n(r)] \quad (2.40)$$

involving $T_s[n]$ as the kinetic energy of non-interacting electrons, the classic electrostatic Hartree energy $E_H[n]$, and the exchange-correlation energy $E_{XC}[n]$. The Hartree term is given by,

$$E_H = \frac{1}{2} \int \int \frac{n(r)n(r')}{|r-r'|} d^3r d^3r' \quad (2.41)$$

The existence of an effective external Kohn-Sham potential $v_{KS}(r)$ is then introduced,

$$v_{KS}(r) = v_{ext}(r) + v_H(r) + v_{XC}(r) \quad (2.42)$$

The Coulomb repulsion between the defined electron and the overall electron density is expressed by the Hartree potential $v_H(r)$,

$$v_H(r) = \frac{\delta E_H[n]}{\delta n(r)} = \int \frac{n(r')}{|r-r'|} d^3r' \quad (2.43)$$

and the exchange-correlation potential, which accounts for quantum effects in the interacting electron system:

$$v_{XC}(r) = \frac{\delta E_{XC}[n]}{\delta n(r)} \quad (2.44)$$

The interaction problem is thus reduced to a system of coupled equations known as the Kohn-Sham equations, which are similar to the Schrödinger equation but only for one electron.

$$\left[-\frac{\nabla^2}{2} + v_{ext}(r) + v_H(r) + v_{XC}(r) \right] \phi_i(r) = \varepsilon_i \phi_i(r) \quad (2.45)$$

where ε_i are the Lagrange multipliers or "eigenvalues", and $\phi_i(r)$ are the single-electron wavefunctions or "orbitals". The equation (2.45) must produce the exact density of the ground state, which is built as follows:

$$n(r) = \sum_i^N |\phi_i(r)|^2 \quad (2.46)$$

Furthermore, one can rewrite the total energy functional of the equation 2.35 in its ground state as⁴²,

$$E[n] = \int n(r)v_{ext}(r)d^3r - \sum_i \int \phi_i^*(r) \frac{\nabla^2}{2} \phi_i(r) d^3r + \frac{1}{2} \int \int \frac{n(r)n(r')}{|r-r'|} d^3r d^3r' + E_{XC}[n] \quad (2.47)$$

At this point, a self-consistency loop is encountered when trying to find a solution to the equation (2.45): the Hartree potential, which depends on the electron density, must be defined to solve the KS equations. The electron density is known to depend on the Kohn-Sham orbitals, so the KS equations must be solved to determine these wave functions. This problem is usually approached iteratively. A schematic representation of this algorithm is displayed in Fig. (2.1).

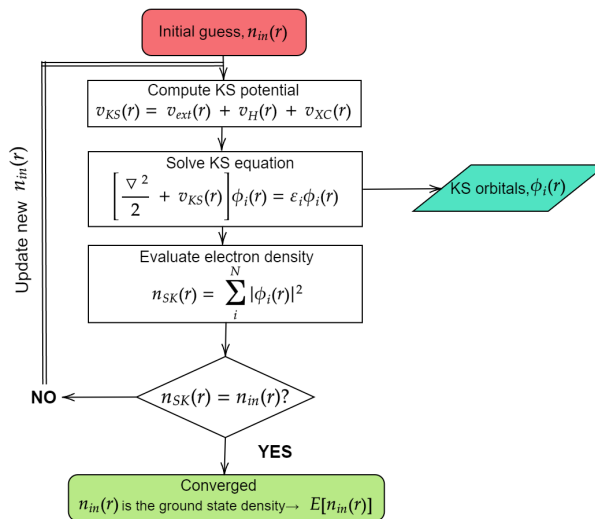


Figure 2.1: Self-consistent iterative method for solving KS equations. Adapted from Ref. ¹

2.3.4 Exchange-Correlation Functionals

As discussed above, to solve the Kohn-Sham equations, it is necessary to identify the exchange-correlation functional $E_{XC}[n]$, whose exact form is unknown but can be approximated. It represents the system's energy that decreases due to the electrons avoiding each other as they pass through the density due to the Pauli principle and Coulomb repulsion⁶⁷.

Since this term is approximated in the Kohn-Sham equation, the reliability of electrical and structural properties predictions will depend on its accuracy⁶⁸. Many exchange-correlation functionals have been developed and are available in the literature. According to Takao Tsuneda, exchange-correlation functionals can be systematically formulated based on the following criteria⁶⁹:

- (i) Meet the fundamental physical requirements of each energy component, e.g., coordinate scaling conditions.
- (ii) Provide reliable reproductions of reactions and quantum properties of a broad spectrum of molecular systems.
- (iii) Employ as a minimum number of parameters as possible.
- (iv) Avoid unnecessary artificial terms added to fulfill particular physical properties.
- (v) Being able to incorporate physical corrections without modifying parameters or involving additional operations.

The density functional approximations for $E_{XC}[n]$ can also be ordered hierarchically, as presented in the Jacob's Ladder proposed by Perdew⁷⁰. $E_{XC}[n]$ in its most basic form may be expressed as:

$$E_{XC}[n \uparrow, n \downarrow] = \int n(r) \varepsilon_{XC}([n \uparrow, n \downarrow]; r) d^3 r \quad (2.48)$$

where ε_{XC} is the exchange-correlation energy per electron. The complexity depends on the "ingredient" on which the ε_{XC} . As shown in Table (2.1), the functionals are ordered in ascending order from the Hartree approximation ($E_{XC}[n] = 0$) to high chemical precision.

Increasingly complex ingredients	Chemical Accuracy	Functional
Unoccupied $\phi_i(r)$	Runge 5: Generalized RPA [‡]	B2PLYP,...
E_X^{HF}	Runge 4: Hybrid-GGA, Hybrid meta-GGA	B3LYP, HSE06,...
$\tau(r)/\nabla^2 n(r)$	Runge 3: meta-GGA	SCAN, mPWB95, ...
$\nabla n(r)$	Runge 2: GGA	PBE, BLYP, ...
$n(r)$	Runge 1: LDA	SPWL, VWN, ...
Hartree-Fock Theory		

Table 2.1: "Jacob's ladder" for exchange-correlation functionals adapted from^{4,5}

2.3.4.1 The Local Density Approximation (LDA)

This non-empirical approximation is considered the simplest and earliest functional (excluding the Hartree $V_{XC} = 0$), in which the local exchange-correlation energy density of an inhomogeneous system is approximated as that of a homogeneous electron gas with the same density at that point in space⁷². The exchange-correlation functional depends only on the value of the density $n(r)$ and takes the form:

$$\begin{aligned} E_{XC}^{LDA}[n(r)] &= \int n(r) \varepsilon_{XC}^{unif}(n(r)) d^3 r \\ &= \int n(r) [\varepsilon_X(n(r)) + \varepsilon_C(n(r))] d^3 r \end{aligned} \quad (2.49)$$

with the exchange-correlation energy per electron in a homogeneous electron gas being $\varepsilon_{XC}^{unif}(n)$. The exchange energy is determined by the LDA exchange hole, resulting in:

$$E_X^{LDA}[n(r)] = -\frac{3}{4} \left(\frac{3}{\pi}\right)^{1/3} \int n^{4/3}(r) d^3 r \quad (2.50)$$

[‡]In most of the literature, the representations of the first four rungs are consistent; however, there is no clear consensus on the fifth rung. Some works include either RPA (random phase approximation) or DHA (double hybrid approximation), while few include both⁷¹. This choice can be attributed to the research approach and system-specific factors.

The main drawback of LDA is that, in most solids, the density is not uniform and does not vary slowly. Therefore, it does not provide an accurate description of the electron interaction since it tends to overestimate $E_X^{LDA}[n(r)]$ and binding forces, as well as giving an error of the order of $\sim 1eV$ for the molecular atomization energies⁶². However, its formal applicability seems particularly suitable for systems similar to the homogeneous electron gas, such as simple metals and covalent systems.

2.3.4.2 The Generalized Gradient Approximation (GGA)

This semi-local approximation, where in addition to the local electron density, the local gradient of the electron density $|\nabla n(r)|$ is considered, has a higher accuracy compared to LDA due to a better description of the exchange energy and the corrected cohesive energies⁷³. The general form of the exchange-correlation functional is⁷⁴:

$$E_{XC}^{GGA}[n(r)] = \int n(r) \epsilon_{XC}^{GGA}(n(r), |\nabla n(r)|) d^3 r \quad (2.51)$$

Equation (2.51) can likewise be expressed based on LDA :

$$E_{XC}^{GGA}[n(r), s] = \int n(r) \epsilon_{XC}^{LDA}(n(r)) F(s) d^3 r \quad (2.52)$$

An enhancement factor $F(s)$ is included, which also depends on both electron density and gradient, with s defined as⁶⁶,

$$s = C \frac{|\nabla n(r)|}{n^{4/3}(r)} \quad (2.53)$$

where C represents a constant containing the Fermi wavevector $k_F(r)$.

Among GGA's limitations is the loss of some XC hole features in strongly correlated systems, such as transition metal oxides. In addition, the calculation of the band gap is inaccurate.

Many GGA functionals have been developed for specific isolated systems, but a well-known one is the Perdew-Burke-Ernzerhof (PBE)⁷⁵. PBE is a non-empirical functional that is an improved and simplified version of the PW91 GGA functional; however, it tends to overestimate the computed volumes.

2.3.4.3 Meta-Generalized Gradient Approximation (meta-GGA)

The meta-GGA method is a semi-local approximation of the orbitals and a non-local functional of density, which involves the incorporation of the Laplacian of electron density $\nabla^2 n(r)$ and the orbital kinetic energy density $\tau(r)$ ⁷⁶. The meta-GGA is described as follows,

$$\begin{aligned} E_{XC}^{meta-GGA}[n(r)] &= \int n(r) \epsilon_{XC}^{meta-GGA}(n(r), |\nabla n(r)|, \nabla^2 n(r)) d^3 r \\ &= \int n(r) \epsilon_{XC}^{meta-GGA}(n(r), |\nabla n(r)|, \tau(r)) d^3 r \end{aligned} \quad (2.54)$$

and the occupied orbital-dependent kinetic energy density $\tau(r)$,

$$\tau_\sigma = \frac{1}{2} \sum_i^{occup} |\nabla \psi_{i\sigma}(r)|^2 \quad (2.55)$$

The Strongly Constrained and Appropriately Normed (SCAN) functional

The non-empirical semilocal SCAN functional has demonstrated superiority over most gradient-corrected functionals in calculating lattice parameters, formation enthalpy, weak interaction binding energies, transition pressures, and atomization energies⁷⁷. It is suitable for systems with non-covalent bonds with an incorporated dispersion term but fails when computing magnetic moments on alloys and surfaces, as they are overestimated⁷⁸.

This functional was the first published meta-GGA to obey all 17 known exact constraints, which are listed in Table (2.2):

SCAN Constraints	
Exchange	(i) Negativity (ii) Spin-scaling (iii) Uniform density scaling (iv) 4th-order gradient expansion (v) Non-uniform density scaling (vi) Tight bound for $2n(r)$
Correlation	(vii) Nonpositivity (viii) 2nd-order gradient expansion (ix) Uniform density scaling to high density (x) Uniform density scaling to low density (xi) Zero-correlation energy for 1-e spin-polarized energy (xii) Non-uniform density scaling
Exchange-Correlation	(xiii) Size extensivity (xiv) Lieb-Oxford bound (xv) Weak spin polarization in the low density (xvi) Static linear response of the uniform electron gas (xvii) Lieb-Oxford bound for $2n(r)$

Table 2.2: List of the 17 SCAN exact constraints arranged by novelty. Adapted from⁶

For van der Waals interactions, SCAN can capture the intermediate part but not include the long-range part. This limitation could be overcome by combining it with the revised nonlocal correlation functional Vydrov-van Voorhis (rVV10)⁷⁹, potentially improving the physisorption and chemisorption binding energies.

The Regularized-Restored SCAN (r^2 SCAN) functional

To overcome numerical instabilities, improve convergence, and promote the generation of reliable ultrasmooth pseudopotentials, the regularized SCAN functional (rSCAN) was proposed. Although its performance was still similar to SCAN, rSCAN introduced two regularizations in the iso-orbital indicator (which is a crucial function to

satisfy the exact constraints), violating several of them⁸⁰.

The introduction of the new r^2 SCAN functional made it possible to satisfy almost all SCAN constraints[†]. This functional maintains the accuracy of SCAN and the grid density stability of rSCAN, with noticeably faster convergence at a lower computational cost⁸¹.

2.3.4.4 Hybrid Functionals

Hybrid functionals partially incorporate nonlocal Hartree-Fock (HF) exchange with local/semi-local DFT exchange, such as the GGA or meta-GGA type, as the main component. This idea is supported by the fact that HF does not consider the effects of electron dynamic correlation. On the contrary, DFT has difficulties concerning self-interaction and strongly correlated systems, so it seems a convenient alternative to couple both approaches⁶⁶.

Becke first successfully applied this method under the name "half-and-half" theory⁸². Given any DFT functional, the hybrid energy related to a mixing coefficient (α) can be expressed as⁸³:

$$E_{XC} = E_{XC}^{DFT} + \alpha(E_X^{HF} - E_X^{DFT}) \quad (2.56)$$

Constant α represents the amount of Hartree Fock replacement in the system. Commonly, a good choice of mixing coefficient is $\sim \alpha = 0.25$ for most molecules^{84,85}. It should be noted that considering the exact HF exchange information makes it a computationally more expensive problem, limiting its applicability on a large scale.

An example of this approximation type is the application of B3LYP, which has become one of the most explored and used functionals in computational chemistry. This scheme includes the exact Hartree-Fock exchange with gradient-corrected correlation terms. The exchange-correlation energy functional is given by⁸⁶:

$$E_{XC}^{B3LYP} = E_{XC}^{LSDA} + a_0(E_X^{HF} - E_X^{LSDA}) + a_x \Delta E_X^{B88} + a_c \Delta E_C^{PW91} \quad (2.57)$$

Where the semi empirical coefficients are $a_0 = 0.2$, $a_x = 0.72$, and $a_c = 0.81$. Here, E_{XC}^{LSDA} is the local spin density approximation exchange-correlation functional, E_X^{HF} is the Hartree-Fock exact exchange functional, ΔE_X^{B88} is the Becke's gradient correction to the LSDA exchange, and ΔE_C^{PW91} is the Perdew-Wang gradient correction for correlation. On solids and surfaces, it has been shown to yield band gaps, binding energies, and magnetic moments in good agreement with experimentally reported values⁸⁷. However, there is a notable shortcoming in describing atomization energies for extended systems, especially in d -metals⁸⁸.

2.4 Hubbard-corrected DFT (DFT + U)

One strategy to correct on-site Coulomb repulsions between electrons is the implementation of the semi-empirical DFT+U (here we consider Dudarev's approach⁸⁹), which adds a Hubbard-type Coulomb repulsion. The Hubbard parameter U , i.e., the energy cost caused by placing two electrons in the same location, is defined as⁹⁰:

$$U = E(d^{n+1}) + E(d^{n-1}) + 2E(d^n) \quad (2.58)$$

[†]However, it does not recover the slowly varying fourth order density-gradient expansion constraint, listed as (iv) in Table (2.2).

Electrons located in the d and f orbitals are susceptible to strong quasi-atomic interactions, and the strength of these interactions can be described by $U_{eff} = U - J$, where J is the in situ exchange parameter. The goal of DFT+U is to provide a corrected description of the ground state of these correlated systems.

In particular, the LDA+U method is extensively employed in transition metal oxides and sulfides⁹¹. It describes the valence electrons similarly to LDA but applies the corrective functional on the strongly correlated d and f electrons. The total system energy accounts for the addition of the standard LDA functional, the Hubbard functional, and a "double-counting" term E_{dc} treated as a mean-field approximation,

$$E_{LDA+U}[n(r)] = E_{LDA}[n(r)] + E_{HUB}[\{n_{mm'}^{I\sigma}\}] - E_{dc}[\{n^{I\sigma}\}], \quad (2.59)$$

where $n_{mm'}^{I\sigma}$ is the localized orbital occupancy number, I is the atomic site index, m is the state index, and σ is the spin.

DFT+U has been shown to reliably predict intermolecular interactions, band gaps, formation energies, and other physical properties, including magnetic and structural features⁹².

2.5 Density functional Tight Binding (DFTB)

Despite the promising results obtained with DFT, faster and less computationally demanding tools are needed to study larger and more complex systems, such as biomolecules. Density Functional Tight Binding (DFTB) is a DFT-based approximation scheme involving derivations from second-order Taylor series expansions of the total Kohn-Sham energy.

Before describing the core of DFTB, it is useful to understand the framework of the Tight-Binding (TB) theories. The main TB model, also known as Linear Combination of Atomic Orbitals (LCAO), states that delocalized Bloch-type functions can be represented by a linear combination of isolated atomic orbitals⁹³. The following expression defines the TB Hamiltonian in its general matrix form⁹⁴,

$$H_{a\mu,b\beta} = \langle \phi_{a\mu} | \hat{H} | \phi_{b\beta} \rangle \quad (2.60)$$

where (a, b) represents the atomic labels, (μ, β) the valence orbitals and $\phi_{a\mu}$ the single atomic function. The single electron effective energy levels of the valence orbitals are represented by the diagonal elements $H_{a\mu,a\mu}$; the nondiagonal elements $H_{a\mu,b\beta}$, or hopping integrals, are the descriptors of electron delocalization, whereas the intersite nondiagonal elements are usually zero:

$$\begin{aligned} H_{a\mu,a\mu} &= \langle \phi_{a\mu} | -\frac{\nabla^2}{2} + \hat{V} | \phi_{a\mu} \rangle = \varepsilon_{a\mu} \\ H_{a\mu,b\beta} &= \langle \phi_{a\mu} | -\frac{\nabla^2}{2} + \hat{V} | \phi_{b\beta} \rangle \end{aligned} \quad (2.61)$$

The total TB energy includes a short-range repulsion term of the ionic core $V_{rep}(R)$ and an exchange-correlation contribution $G[n(r)]$. It is summarized in an expression consistent with the DFT approach:

$$E[n(r)] = V_{rep}(R) + \sum_k n_k \varepsilon_k + G[n(r)] \quad (2.62)$$

In current DFTB models, the electron density $n(r)$ is expanded around a superposed initial density $n_0(r)$ perturbed by a fluctuation,

$$n(r) = n_0(r) + \delta n(r) \quad (2.63)$$

The total energy functional expanded to second order under this approach results in⁹⁴:

$$E[n(r)] = E[n_0(r)] + \int \frac{\delta E[n(r)]}{\delta n(r)} \Big|_{n_0} \delta n(r) + \frac{1}{2} \int \int \frac{\delta^2 E[n(r)]}{\delta n(r) \delta n(r')} \Big|_{n_0} \delta n(r) \delta n(r') + \dots \quad (2.64)$$

Based on the approach outlined above, the DFTB has implemented three main versions^{95,96}:

1. **DFTB1**: It is a non-self-consistent model that takes into account the first 2 terms of the equation (2.64). It has a convenient applicability for systems with small charge transfer.
2. **DFTB2**: It is a self-consistent model that approximates the first 3 terms of the equation (2.64), and assumes the density fluctuation as the superposition of the neutral density contributions of the atoms. It is suitable for molecules with partial charge transfer.
3. **DFTB3**: Similar to DFTB2 but includes third-order expansion, which can substantially improve the description of charged molecules.

2.6 Vienna *ab initio* Simulation Package (VASP)

Among the best-known *ab initio* DFT computational simulation tools are the Vienna *ab initio* Simulation Package (VASP), which was parallelized mainly by Georg Kresse and co-developed with other collaborators from code written by Mike Payne.

This package uses plane wave basis sets and the projector augmented wave (PAW) or ultrasoft pseudopotentials to calculate electron-ion interactions, either by KS equations in the DFT framework or from a hybrid approach. Some of the remarkable features of VASP are that it (i) offers an efficient alternative to reduce orthonormalization operations via iterative diagonalization, (ii) it calculates the electronic ground state after each full cycle of self-consistent field (SCF) iterations accurately, (iii) describes the electron-ion interaction using pseudopotentials, and (iv) it improves energy conservation along the molecular trajectory^{97,98}.

2.6.1 Plane-waves basis set

The basis set VASP uses for expanding KS orbitals and electronic charge densities is conformed by plane waves. Bloch's theorem⁹⁹ states that the Coulomb potential in a crystalline solid is periodic and that the wave function is the product of the plane wave and a function $u_{nk}(r)$ sharing the same lattice periodicity,

$$\psi_{nk}(r) = e^{ikr} u_{nk}(r) \quad (2.65)$$

where k is the wave vector in the first Brillouin zone and is determined by the unit cell. The KS orbitals are expressed as^{100,101}:

$$\psi_{nk}(r) = \frac{1}{\sqrt{\Omega}} \sum_G C_{Gnk} e^{i(G+k)r} \quad (2.66)$$

In this equation, the expansion coefficients are C_{Gnk} , \mathbf{G} are the reciprocal lattice vectors, and Ω is the volume of the primitive cell given by:

$$\Omega = a_1 \cdot (a_2 \times a_3) \quad (2.67)$$

The density can also be defined in terms of plane waves:

$$n(r) = \sum_G n_G e^{iG \cdot r} \quad (2.68)$$

The expansion is restricted to a condition that establishes that only reciprocal vectors whose energy is less than a given cutoff energy are included in the basis set,

$$\frac{1}{2} |G + k|^2 < E_{cut} \quad (2.69)$$

Some advantages conferred by using plane waves are the straightforward momentum space representation, convergence control based on cutoff energy, and, unlike localized bases, basis set overlap errors can be prevented¹⁰².

2.6.2 Pseudopotentials

Plane-wave expansion could achieve convergence if the nodal feature of the valence orbitals is removed, which can be done by including a pseudopotential. The pseudopotential introduces a softer, effective potential that replaces the strong potential exerted by bound and core electrons on the valence electrons¹⁰³. The plausibility of this proposition is based on the fact that in most atoms, the chemical bonds are dictated by the valence electrons since the contribution of the electrons in the core is usually negligible¹⁰⁴.

Let now consider the wavefunction of an electron in the valence shell⁴⁵:

$$|\psi_v\rangle = |\psi_{ps}\rangle - \sum_i |\psi_{c_i}\rangle \langle \psi_{c_i} | \psi_{ps}\rangle \quad (2.70)$$

where $|\psi_{c_i}\rangle$, $|\psi_v\rangle$ and $|\psi_{ps}\rangle$ are the core, true valence, and pseudo wave functions, respectively. Considering the form of the KS equation (2.45) we have,

$$\begin{aligned} \left[-\frac{\nabla^2}{2} + v_{eff} \right] |\psi_v\rangle &= \varepsilon_v |\psi_v\rangle, \\ \left[-\frac{\nabla^2}{2} + v_{ps} \right] |\psi_{ps}\rangle &= \varepsilon_v |\psi_{ps}\rangle \end{aligned} \quad (2.71)$$

The pseudopotential obtained is then a nonlocal energy-dependent potential and is defined as:

$$v_{ps} = v_{eff}(r) + \sum_i (\varepsilon_v - \varepsilon_{c_i}) |\psi_{c_i}\rangle \langle \psi_{c_i}| \quad (2.72)$$

Pseudopotentials can be classified into: (i) norm-conserving¹⁰⁵, and (ii) Vanderbilt ultrasoft¹⁰⁶. The second group encompasses pseudopotentials that do not consider the norm-conserving condition, which implies that the charge in the core is not equal to that of the wave function of all electrons. Therefore, fewer plane waves are needed for the approximation.

2.6.3 The Projector Augmented-Wave (PAW) Method

This method generalizes the concepts of pseudopotentials and augmented linear plane waves and is used to avoid the development of nonlinear kernel corrections. This approach was first introduced by Bloch^{107,108} and further refined by Kresse¹⁰⁹. It involves a linear transformation of the pseudopotential to the all-electron wave function:¹⁰²:

$$|\psi_{AE}\rangle = |\psi_{ps}\rangle + \sum_i (\phi_i^{AE} - \phi_i^{ps}) \langle p_i^{ps} | \psi_{ps} \rangle \quad (2.73)$$

The partial waves of all electrons ϕ_i^{AE} are obtained from a non-spin-polarized reference atom. In contrast, the pseudopotential partial waves ϕ_i^{ps} are equivalent to the partial waves of all electrons outside the radius of the core. On the other hand, the projector functions p_i represent linear combinations of intermediate functions and are dual to the partial waves,

$$\langle p_i^{ps} | \phi_j^{ps} \rangle = \delta_{ij} \quad (2.74)$$

This process can be considered an all-electron treatment in which the core states of the atoms are frozen. Although, in theory, a reliable transformation requires an infinite number of projectors and partial waves, for practical applications, up to two projector functions for each angular momentum channel are adequate¹¹⁰.

2.6.3.1 PAW vs. Ultrasoft pseudopotentials (US-PP)

DFT implementations to treat core electrons have been performed, commonly adopting either the PAW approach or ultrasoft pseudopotentials (US-PP). The latter, which was first proposed by Vanderbilt¹⁰⁶, relaxes the norm-conserving condition and treats the electron density as a soft contribution given by the squared moduli of the wave functions to describe the valence electrons, and a hard part involving the angular momentum projector and the magnification functions that account for electrons located close to the nucleus¹¹¹. The construction of smooth pseudo-wavefunctions allows the reduction of the cutoff energy and the number of plane waves needed to describe the wave function, which helps to gain computational efficiency.

The PAW method has proved to be more accurate than SS-PP in some scenarios, such as strong magnetic moment transition metals and alkali and alkali-earth metals, where particular effects within the core region must be considered. This can be attributed to the need for using a smaller radial cutoff. However, SS-PP yields accurate results for p-elements and most non-magnetic transition metals.

2.7 DFTB+ Code

DFTB+ is an open-source quantum mechanics simulation code that uses a localized basis set of atomic orbitals to calculate electronic structure and molecular geometry¹¹². In general, electronic parameterization in DFTB+ involves determining atomic densities and basis functions and calculating Hamiltonian and overlap matrix elements.

DFTB+ relies on DFTB- and xTB- approaches and extensions, such as long-range corrected functionals for excited states and steady-state electron transport simulations. In general terms, the xTB methods are an extended version of the tight binding methods. The xTB Hamiltonian is constructed on a partially polarized basis set that includes the coordination number dependence. This extension achieves a good ratio between performance and computational cost. For a broader view of the improvements of this theory, please refer to Ref¹¹³.

Chapter 3

Methodology

This section provides information on the computational tools used in this research work and how the proposed systems' main energy descriptors are calculated. It is divided into the following 2 main methodologies: DFT and DFTB, with their implementation computational software, which are VASP and DFTB+, respectively. The outlined procedures range from the modeling of multicomponent nanoclusters supported on Anatase $TiO_2(101)$ (A- $TiO_2(101)$), including the relaxation of these structures, to the establishment of their characteristic electronic structure.

3.1 Input Structures

As a well-studied material, the A- TiO_2 unit cell is available in several online databases. The construction of the final surface of this work is performed starting from the unit cell extracted from the Materials Project¹¹⁴, shown in Fig. (3.1).

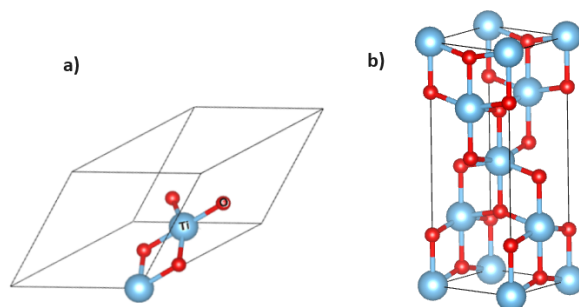


Figure 3.1: Input crystal structures: a) primitive cell, and b) unit cell of a body-centered tetragonal (BCT) A- TiO_2 (space group $I4_1/amd$). Visualization was performed using VESTA software².

3.2 VASP computational implementation

3.2.1 Optimal Parameters for Bulk A-TiO₂

Convergence tests are performed on the original structure to determine the optimal parameters. The files needed for these simulations are INCAR, POSCAR, KPOINTS, and POTCAR. This section will implement DFT calculations using 2 different meta-GGA functionals: SCAN and r^2 SCAN, combined with the nonlocal rVV10 van der Waals functional.

3.2.1.1 Cut-off Energy (E_{cut})

As discussed in Section (2.6.1) and since VASP is a package based on the plane-wave basis set, it is necessary to determine the cutoff energy to ensure the completeness of this set, an accurate electronic description of the system and also to optimize the simulation in terms of computational cost. The cut-off energy convergence test was conducted using SCAN+rVV10 functional. From Fig. 3.2, we have that the appropriate E_{cut} is 700 eV since the desired convergence in total energy of 1meV/atom is achieved at this value. This convergence threshold was set following previous DFT studies of A-TiO₂ (101)^{115,116}, which is usually associated with the value of energy changes in structural phase transformations of titanium dioxide¹¹⁷. The electronic properties of the system may not be fully captured by the plane-wave basis set at 400 eV, leading to a lower energy state with an energy difference of more than 3 meV compared to the cutoff energy at 450 eV. The energy begins to converge to a stable value as it approaches 700 eV, as the more complete basis set allows a more accurate representation of the electron density, especially near the atomic core.

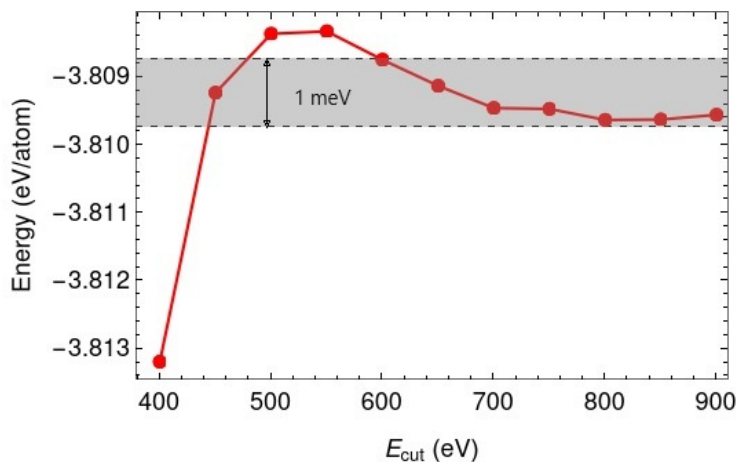


Figure 3.2: Cut off energy convergence test computed with SCAN+rVV10 functional for $400 \leq E_{cut}(eV) \leq 900$. Convergence within 1meV/atom is reached at $E_{cut} = 700$.

3.2.1.2 K-points Sampling

The k-points selection within the Brillouin zone is given by the Γ centered Monkhorst-Pack grid approach¹¹⁸. The k-point density Δk indicates the number of k points per unit length in the reciprocal space. The convergence test was calculated with the SCAN+rVV10 functional so that the total energy of the k-point density changes is <1 meV. As noticed in Fig. 3.3, in the range of k-point densities $0.033 \leq \Delta k (\text{\AA}^{-1}) \leq 0.044$ the total energy remains stable within 1 meV/atom. Choosing a k-point density of $\Delta k = 0.040 \text{\AA}^{-1}$ for the bulk A-TiO₂ (equivalent to $7 \times 7 \times 9$ k-point mesh) provides a finer mesh that could potentially lead to more accurate results that are convergent within the criterion while maintaining computational efficiency. The k-point meshes for the subsequent construction of A-TiO₂(101)-(1 \times 1) and A-TiO₂(101)-c(4 \times 2) supercell are chosen to ensure the same accuracy.

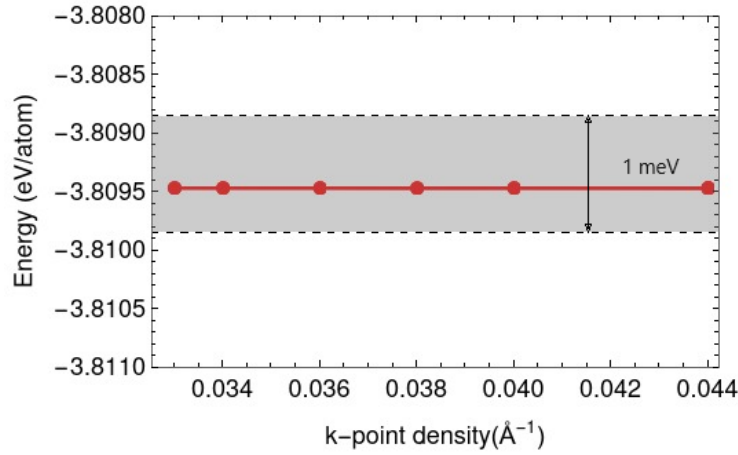


Figure 3.3: k-point convergence test computed with SCAN+rVV10 functional for $0.033 \leq \Delta k (\text{\AA}^{-1}) \leq 0.044$. Chosen k-point density was $\Delta k = 0.040 \text{\AA}^{-1}$.

3.2.1.3 Birch-Murnaghan Equation of State

The third-order Birch-Murnaghan (EOS) equation of state¹¹⁹ is useful for determining the optimal structural parameters of the system under consideration. By varying the volumes, the total energy for each scenario is calculated and the resulting points are adjusted to the following equation:

$$E(V) = E_0 + \frac{9V_0 B_0}{16} \left\{ \left[\left(\frac{V_0}{V} \right)^{2/3} - 1 \right]^3 B'_0 + \left[\left(\frac{V_0}{V} \right)^{2/3} - 1 \right]^2 \left[6 - 4 \left(\frac{V_0}{V} \right)^{2/3} \right] \right\}, \quad (3.1)$$

where information can be extracted, such as the optimum volume V_0 (which is the minimum of the fitted equation), the bulk modulus B_0 , and the B'_0 is the first derivative of the bulk modulus with respect to pressure at T=0K. This provides insight into how the material behaves under compression and expansion.

Fig. 3.4 shows the energy values obtained by calculations using the SCAN+rVV10 functional for volumes from 64 to 73 \AA^3 and their respective fit. This functional yielded the following parameters: $V_0 = 68.21 \text{\AA}^3$, $B_0 = 189.96$

GPa, and $B'_0 = 2.31$. Similarly, for the fit depicted in Fig. 3.5, which used the r^2 SCAN+rVV10 data, we obtained $V_0 = 68.56 \text{ \AA}^3$, $B_0 = 187.76 \text{ GPa}$, and $B'_0 = 2.36$.

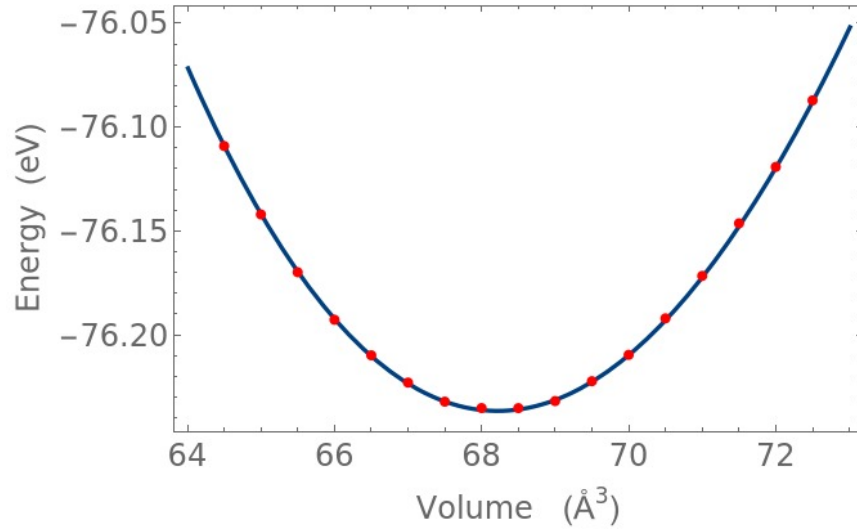


Figure 3.4: Birch-Murnaghan EOS for the mass of A- TiO_2 : the solid line is equation (3.1) fitted from data calculated with the SCAN+rVV10 functional.

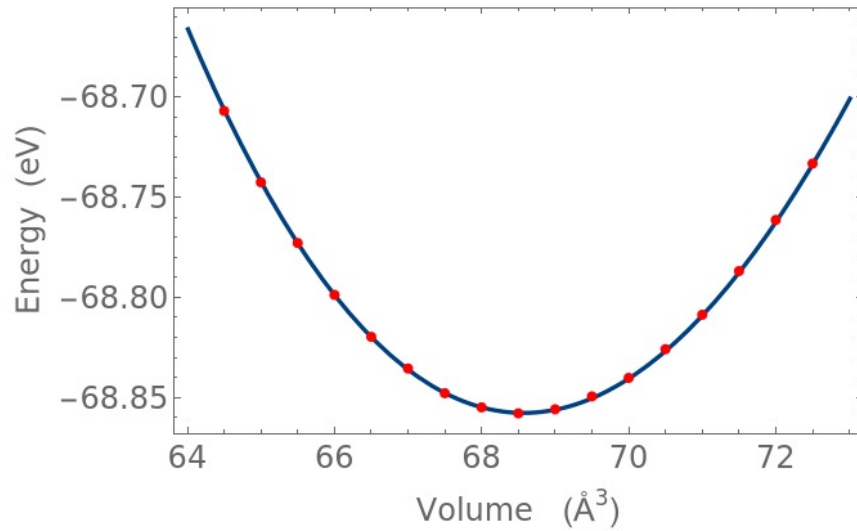


Figure 3.5: Birch-Murnaghan EOS for the mass of A- TiO_2 : the solid line is equation (3.1) fitted from data calculated with the r^2 SCAN+rVV10 functional.

3.2.2 Hubbard U correction

This work uses the simplified rotationally invariant DFT+U, also known as the Dudarev approach. The DFT+U variant type can be selected by modifying the LDAUTYPE variable in the INCAR file (LDAUTYPE=2, in this case).

The Hubbard correction parameter "U" is calculated using various Coulomb corrections. Here, we tested U=0 to 7 in steps of 0.5 and performed VASP calculations for systems under those conditions. The band gap information is then extracted, and a relationship is established between the U vs. band gap data. These values are validated against the available experimental value, which, as mentioned before, is ~ 3.2 eV, and the extrapolated value closest to it will be the correction. Fig. 3.6 shows the values obtained from the calculation using SCAN+rVV10, while Fig. 3.7 represents the r^2 SCAN data. The suitable corrections found are $U_{SCAN} = 5.3$ eV and $U_{r^2SCAN} = 5.15$ eV, respectively.

To the best of our knowledge, no available works have employed SCAN or r^2 SCAN functionals with U-correction to reproduce the electronic properties of TiO_2 in its Anatase phase. However, using a SCAN+U framework has been explored for Rutile- TiO_2 . In this study¹²⁰, an optimal value of U = 2.5 eV yielded a bandgap of 2.06 eV, closer to the experimental data of 3 eV than the uncorrected DFT-SCAN. Although this approximation still underestimates the bandgap, it is shown that U correction can improve the accuracy in calculating the ground state energies of 3d oxides when using meta-GGA functionals.

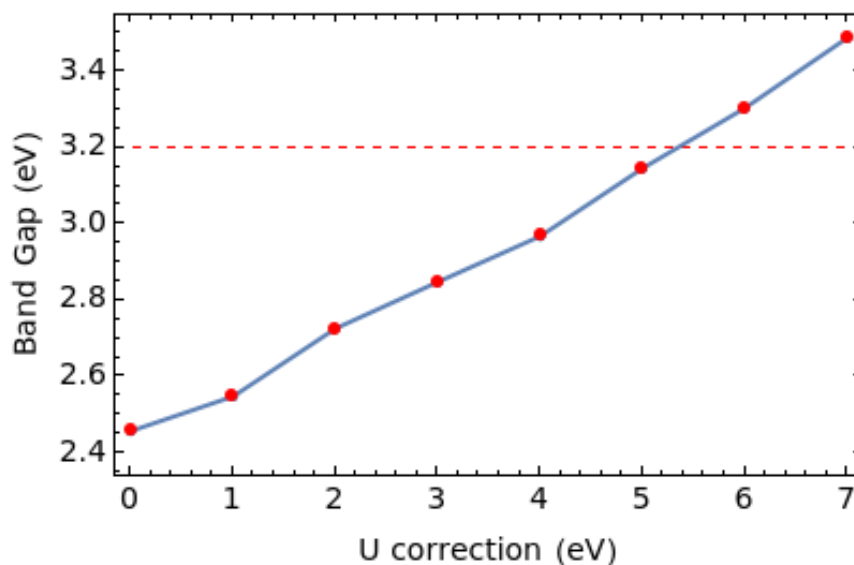


Figure 3.6: Hubbard correction vs Band Gap for U=1-7 using SCAN+rVV10 functional. The dashed red line indicates the experimental band gap for A- TiO_2 ³.

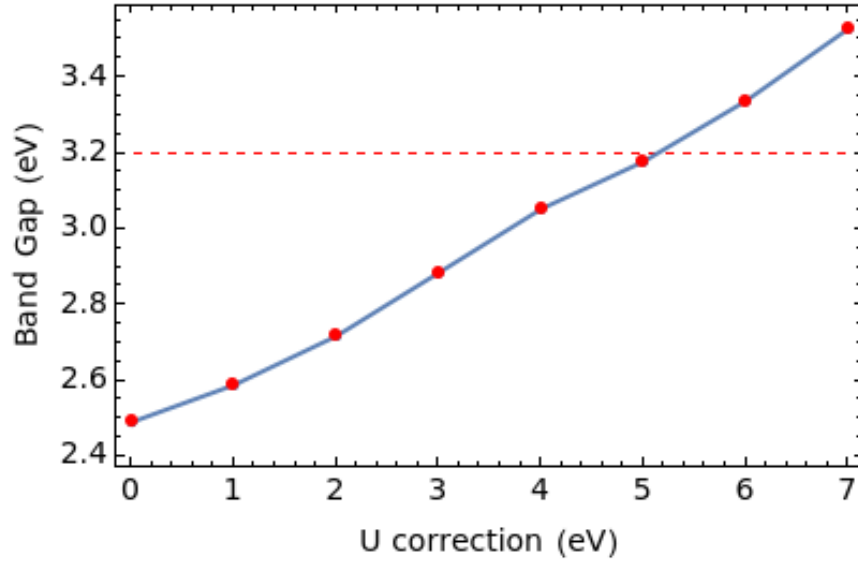


Figure 3.7: Hubbard correction vs Band Gap for $U=1-7$ using r^2 SCAN+rVV10 functional. The dashed red line indicates the experimental band gap for $A-TiO_2^3$.

The structural parameters extracted from the Birch-Murnaghan EOS are also reported for each case in Tables (3.1) and (3.2),

U (eV)	$V_0(\text{\AA}^3)$	$B_0(\text{GPa})$	B'_0	Band Gap (eV)
0	68.21	189.96	2.31	2.46
1	68.85	188.12	2.50	2.55
2	69.50	186.54	2.38	2.73
3	70.16	185.14	2.28	2.85
4	70.82	184.34	2.27	2.97
5	71.49	183.50	2.11	3.15
5.3	69.71	191.41	2.48	3.18
6	72.15	181.28	2.34	3.30
7	72.83	180.08	2.28	3.49

Table 3.1: Optimal Volume (V_0), Bulk Modulus (B_0), and Band Gap for $A-TiO_2$ with Hubbard correction $U=1-7$ using SCAN+rVV10 functional.

U (eV)	$V_0(\text{\AA}^3)$	$B_0(\text{GPa})$	B'_0	Band Gap (eV)
0	68.56	187.76	2.36	2.49
1	69.20	185.33	2.37	2.59
2	69.84	183.58	2.47	2.72
3	70.49	182.46	2.44	2.89
4	71.16	180.92	2.43	3.05
5	71.83	179.75	2.40	3.18
5.15	71.92	179.04	2.49	3.21
6	72.50	177.82	2.43	3.34
7	73.17	176.65	2.48	3.53

Table 3.2: Optimal Volume (V_0), Bulk Modulus (B_0), and Band Gap for A- TiO_2 with Hubbard correction $U=1-7$ using $r^2\text{SCAN}+r\text{VV10}$ functional.

3.2.3 A- $TiO_2(101)$ - $c(4 \times 2)$ supercell

Once the cell primitive is optimized and relaxed by the corresponding Hubbard correction value, this result can be used to cleave a plane with orientation (101). The surface was modeled using three O-Ti-O layers and introducing a vacuum of 20\AA perpendicular to the plane for subsequent cluster placement and to avoid interactions between periodic images. The procedure is illustrated in Fig. 3.8.

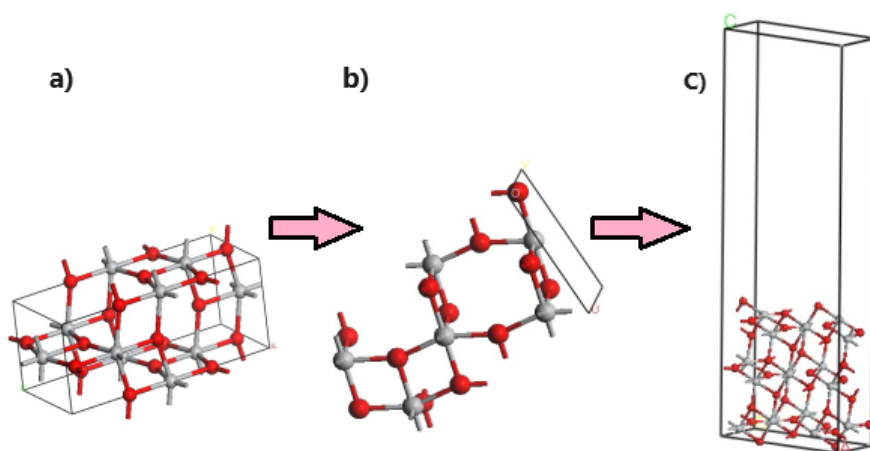


Figure 3.8: Modeling procedure for A- $TiO_2(101)$. It starts with a) a fully relaxed primitive cell, followed by b) imposition of the (101) plane. Next, a-c) slab model of the A- $TiO_2(101)$ surface with a vacuum of 20\AA is constructed.

The optimal computed lattice parameters for bulk A- TiO_2 are $a=b=3.82\text{\AA}$, $c=9.55\text{\AA}$ for $\text{SCAN}+U$, and $a=b=3.86$

\AA , $c=9.64 \text{ \AA}$ for $r^2\text{SCAN}+U$. Geometry relaxation of the slab $A\text{-TiO}_2(101)\text{-}(1 \times 1)$ and the supercell $A\text{-TiO}_2(101)\text{-}c(4 \times 2)$ is conducted with a k-point mesh of $2 \times 7 \times 1$ and $2 \times 2 \times 1$, respectively. The bottom layer (32 O and 16 Ti) is kept fixed to emulate the stability of the bulk structure.

The supercell is generated from the relaxed structure $A\text{-TiO}_2(101)\text{-}c(1 \times 1)$ with optimal lattice parameters of $a=10.39 \text{ \AA}$, $b=3.86 \text{ \AA}$ and $c=29.56 \text{ \AA}$. $A\text{-TiO}_2(101)$ supercell is proposed to be $c(4 \times 2)$ since the surface size is appropriate to ensure minimal image interaction between the clusters. The notation $c(4 \times 2)$ implies that a supercell is being generated that is four times as large along one lattice vector and twice as large along the other. For a better understanding, the construction of this supercell is schematized in Fig. 3.9,

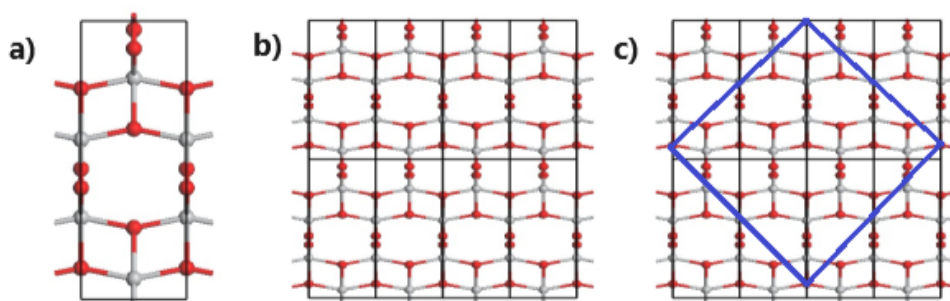


Figure 3.9: a) Original $A\text{-TiO}_2(101)\text{-}(1 \times 1)$ unit cell, b) replicate unit cell twice in x direction and four-times in y-axis to obtain a $c(4 \times 2)$ supercell, c) solid blue line refers to the $c(4 \times 2)$ supercell used in this work.

The total system is made up of 144 atoms (96 O and 48 Ti). The optimal parameters estimated with $r^2\text{SCAN}$ for this supercell were $a=b=12.94 \text{ \AA}$ and $c=29.56 \text{ \AA}$.

It should be noted that the k-point grid for each k-point density was calculated based on the lattice parameters and the reciprocal lattice vectors of each model. The k-point grids were selected based on the convergence test performed in section (3.2.1.2), where it was determined that a k-point density of 0.040 \AA^{-1} was sufficient for accurate calculations for all structures. The k-point grids were adjusted to reflect periodicity and symmetry for the bulk, slab, and supercell models of $A\text{-TiO}_2$. The $2 \times 7 \times 1$ grid is appropriate for the slab as it reflects the change in periodicity in the in-plane directions compared to the slab while minimizing sampling to a single k-point along the z-axis due to vacuum. The $c(4 \times 2)$ supercell exhibits extended periodicity in the x-y plane, and the $2 \times 2 \times 1$ grid is suitable for capturing its extended periodicity and reduced symmetry.

3.3 DFTB+ computational implementation

The construction of the supercell follows a procedure similar to that described in Section 3.2.3 but using the DFTB approach instead of DFT. In this sense, a semiempirical method and a localized atomic orbital basis set are taken into consideration. The software employed is DFTB+ Version 24.1, and the required INPUT file is "*dftb_in.hsd*" which

provides blocks of information about geometry, atom constraints during dynamics, and the Hamiltonian model to be used.

First, a geometry and lattice relaxation is performed with a $2 \times 2 \times 1$ k-point mesh and making use of a GFN1-xBT functional¹²¹ with a self-consistent tolerance of 10^{-6} Eh. Like the structures computed with VASP, the last surface layer is immobilized. The total system is made up of 144 atoms (96 O and 48 Ti). Following this relaxation, a $6 \times 6 \times 1$ k-point grid is used to calculate the electronic structure.

The resulting optimal parameters for $A\text{-TiO}_2(101)\text{-}c(4 \times 2)$ were $a=b=13.29$ Å and $c=30$ Å. The converged structure is shown in Fig. 3.10

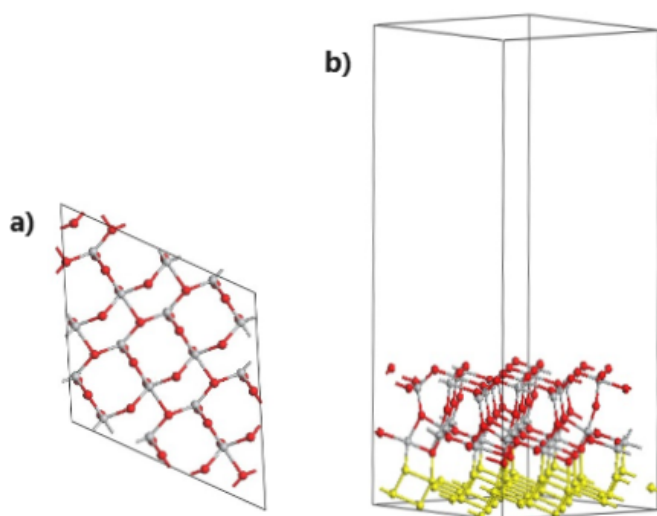


Figure 3.10: Supercell $A\text{-TiO}_2(101)\text{-}c(4 \times 2)$ relaxed by the GFN1-xTB method from a) Top view of its outermost layer, and b) Side view. The atoms selected in yellow (bottom O-Ti-O layer) indicate that they are fixed, similar to the case of the structure calculated by DFT.

3.4 Oxygen defective $A\text{-TiO}_2(101)$ surface

Oxygen vacancies are known to contribute more to the band gap tuning compared to interstitial Ti. Furthermore, it is shown that the surface oxygen vacancy is energetically more favorable than the incorporation of a subsurface vacancy¹¹⁵. Thus, an oxygen surface vacancy ($V_{O\text{-}sur}$) is introduced to analyze the defect-induced properties on the $A\text{-TiO}_2(101)$ surface in the presence of a metallic cluster. The relaxation is performed after removing one binding oxygen and simultaneously adding the metallic cluster to the surface. This strategy allows the system to adapt to the combined conditions imposed by both the cluster and the presence of the vacancy. The position selected for the vacancy is depicted in Fig. 3.11, and it will remain the same for all calculated systems.

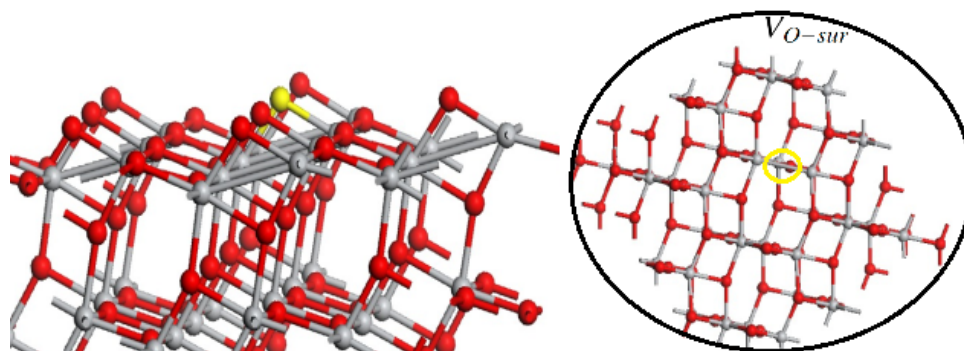


Figure 3.11: Introduction of the surface oxygen vacancy in the A-TiO₂(101)-c(4 × 2). The label V_{O-sur} indicates the position of the vacancy.

3.5 Cluster@A-TiO₂(101) construction

An initial truncated pyramid-type cluster composed of 8 gold atoms (Au8) was constructed following the procedure of Mikołajczyk et al.¹¹⁵, and subsequently geometrically optimized already supported on A-TiO₂(101)-c(4 × 2). This geometry was chosen because it is the most stable compared to other configurations, such as wall-like or flat. The design of this cluster was also inspired by the results of previous studies¹²², which highlighted that systems derived from this configuration are realistic and thermodynamically stable. Briefly, to build an Au cluster with this geometry, a face-centered cubic lattice (FCC), characteristic of gold atoms, is considered. Then, starting from a square base and following the arrangement of the atoms based on available STM information¹²³, the structure is built layer by layer, reducing the number of atoms in the second layer (3 atoms) compared to the base layer (5 atoms) to achieve the pyramidal arrangement. The height is defined with two layers, adjusting the position of the atoms to ensure the desired shape and truncation at the top. The resulting structure (see Fig. 3.12) was chosen as the initial configuration of all clusters. Thus, the Au8 cluster serves as a "template" for systematically exploring clusters of different noble metals and the number of component atoms.

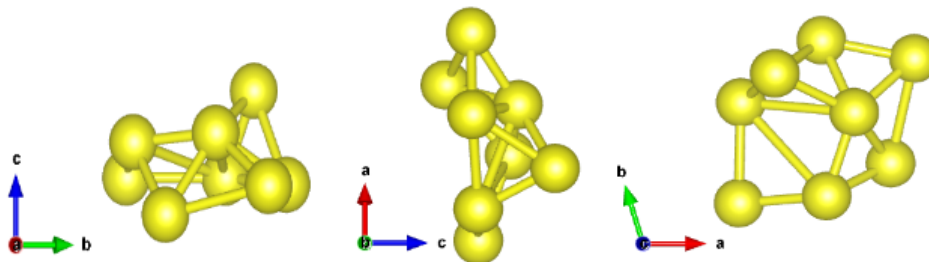


Figure 3.12: Structural convergence achieved for the Au8 cluster, viewed from different coordinate planes.

One single cluster is placed on the Anatase surface. It is worth mentioning that, for all systems, the clusters occupy the same position during the generation of the initial geometry before relaxation, i.e., the clusters have a common placement position. When considering V_{O-sur} , a cluster atom must be intentionally placed near the vacancy site as a strategy to try to achieve faster geometric convergence.

3.6 Density of States (DOS) and Partial Density of States (PDOS)

Density of states (DOS) is one of the essential tools of DFT to understand the electronic structure of a material. It shows the distribution of electrons along the energy spectrum by quantifying the energy states available in the system that can be occupied by electrons. In the DFT framework, the DOS can be obtained by integrating the electron density in k -space; this is by sampling the Brillouin zone along a given k -grid, which involves solving the Kohn-Sham equations to determine the energy eigenvalues at each k -point, for subsequent integration of the electronic states at each energy level¹. The DOS is a descriptor that quantifies the number of electronic states in the energy domain; it takes into account the total contribution of the atoms and orbitals of the system and provides useful insights into the nature of electronic transitions, the existence of a band gap, the identification of valence and conduction bands, among others. The peaks indicate regions with high density of accessible energy levels and the fermi level, where the electrons are probable to be found at 0K, is often located at zero energy.

Similarly, the Partial Density of States (PDOS) accounts for the contribution of individual atoms to the DOS. It helps to determine the role of specific elements in the overall electronic properties of the system. To calculate the PDOS in VASP, the tetrahedral method with Blöchl corrections is used (ISM_EAR=-5), and the energy is divided into 5001 intervals (NEDOS=5001). In addition, the parameter LORBIT=11 is set to decompose the projected DOS. In the case of DFTB+, the *ProjectStates* option of the *Analysis* block is modified by specifying each atom species within the *Region* segment.

3.7 Adsorption energies ΔE_{Ads}

In this study, we will estimate the adsorption energy by directly calculating the difference between the energy of the cluster/surface system (E_{tot}), the energy of the bare TiO_2 slab (E_{TiO_2}), and the energy of the gas-phase metal cluster (E_{C_n}). The adsorption energy of a cluster on a surface defined by Vittadini¹²⁴ is given by an expression dependent on the energy of the isolated gas-phase adsorbate:

$$\Delta E_{Ads} = -E_{tot} + E_{C_n} + E_{TiO_2} \quad (3.2)$$

and similarly, the cohesion energy,

$$\Delta E_{Coh} = E_{tot} - [E_{TiO_2} + n_1 E_{M_1} + n_2 E_{M_2} + \dots + n_i E_{M_i}] \quad (3.3)$$

where E_{M_i} represents the energy of a single isolated metal atom and n_i is the number of atoms of each metal (M_i) in the cluster.

3.8 Work function

The energy needed to remove an electron from a solid is known as the work function (ϕ), a fundamental surface feature. It is defined as the difference between the vacuum potential and the fermi level:

$$\phi = E_{vac} - E_{fermi} \quad (3.4)$$

Here, we will estimate the work function of four selected systems of cluster@A-TiO₂(101)-c(4×2) + V_{O-sur} computed with VASP, where the cluster can be of one of the following configurations: Au₈, Au₂Pt₂Ag₂Pd₂, Pd₁₁, or Au₈Pd₃. This is done by setting the LVTOT= TRUE tag in the INCAR file and post-processing with the python MacroDensity package¹²⁵. VASP provides an output file, "LOCPOT", which contains the local electronic potential (eV), which will be transformed into a planar-averaged potential along the vector z.

Chapter 4

Results & Discussion

The results are mainly based on the PDOS description of the proposed systems. Most systems are calculated with DFTB, but some configurations are implemented within the DFT approach to exemplify the usefulness of meta-GGA functionals. For convenience, the projected density of states is presented as a function of the energy shifted from the Fermi level; in this way, the valence and conduction levels are located relative to the Fermi level.

The obtained energetic parameters are compared to account for the contribution of each species to the overall electronic structure. In addition, the impact of oxygen vacancies on cluster adsorption and band gap formation is discussed. Finally, the work function is determined for the systems calculated with VASP.

4.1 Bulk Anatase- TiO_2

Bulk Anatase- TiO_2 ($A-TiO_2$) was computed with DFT functionals (SCAN and r^2SCAN), and via DFTB (GFN1-xBT).

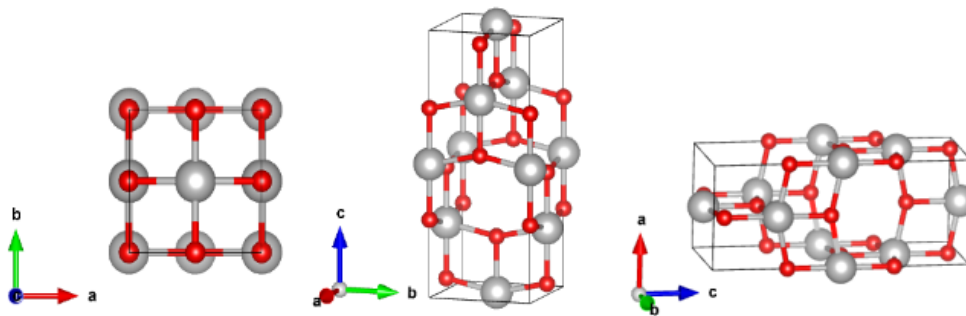


Figure 4.1: Bulk unit cell of Anatase TiO_2 after relaxation using SCAN+rVV10+U functional.

The optimal lattice parameters and band gap obtained with each functional are detailed in Table 4.1. It is observed that the value of the Hubbard parameter can vary significantly depending on the exchange-correlation functional employed in DFT. Comparative studies can be found in the literature to evaluate the effect of different functionals in predicting the electronic properties of A-TiO₂ when the U-correction is applied. For instance, to achieve a comparable band gap prediction using the PBE+U and Perdew-Wang 91 (PW91)+U methods, a difference of 1.8 eV in the applied corrections was required, i.e. U=5.8eV for PBE and U=4 for PW91.

In addition, González Ramirez¹²⁶ evaluated several exchange-correlation functionals, including LDA, PBE, PW91 and PBE revised for solids (PBEsol) with the same Hubbard correction of 4.2 eV for titanium, and found that PBEsol+U provided more accurate predictions in terms of lattice constants and bond lengths. The band gap prediction accuracy was also observed following the trend PBE+U=PBEsol+U > PW91+U > LDA+U.

Table 4.1: Crystallographic and electronic structure data for Bulk Anatase TiO₂. In this table, a, b, and c are the lattice parameters, and E_{bg} indicates the computed band gap. The angles of the unit cell are $\alpha = \beta = \gamma = 90^\circ$.

Bulk Anatase TiO ₂						
<i>Functional</i>	<i>U correction (eV)</i>	<i>a=b (Å)</i>	<i>c (Å)</i>	<i>Volume(Å³)</i>	<i>E_{bg}(eV)</i>	<i>Source</i>
SCAN+rVV10+U	U=0	3.79	9.52	136.75	2.53	This work
	U=5.3	3.82	9.55	139.36	3.12	This work
<i>r</i> ² SCAN+rVV10+U	U=0	3.78	9.57	136.74	2.45	This work
	U=5.15	3.86	9.64	143.63	3.14	This work
PBE+U	U=5.8	3.88	9.77		2.79	¹²⁷
	U=4.2	3.83	9.63		2.00	¹²⁸
	U=4.2	3.83	9.76		2.51	¹²⁶
	U=9	3.80	9.81	141.70	3.35	¹²⁹
	U=2.5	3.83	9.70		2.29	¹³⁰
PBEsol+U	U=5.97	3.83	9.66	141.95	2.91	¹³¹
	U=8.5	3.87	9.76		3.17	¹³²
	U=4.2	3.80	9.64		2.51	¹²⁶
PW91+U	U=4	3.88	9.64		2.70	¹³³
	U=4.2	3.82	9.71		2.49	¹²⁶
LDA+U	U=4.2	3.77	9.52		2.44	¹²⁶
GFN1-xBT	-	3.47	10.79	129.95	2.49	This work
Experimental	-	3.79	9.51	136.28	3.20	^{3,134}

The values of the U corrections implemented in this work are consistent with those intervals evaluated in the literature. In particular, the *r*²SCAN+rVV10+U (U=5.15 eV) functional showed one of the closest approximations to the experimental band gap underestimating it by 1.88%. Still, the results of SCAN+rVV10+U (U=5.3 eV) are also comparable with a deviation of 2.5%. As for the lattice constants, both functionals show a slight overestimation,

but SCAN+rVV10 gives a closer approximation both with and without correction. When the correction is not applied, i.e., $U=0$ eV, the values are more accurate than when applied, i.e., $U=5.3$ eV. This suggests that for A-TiO₂, the Hubbard correction is more crucial in predicting the electronic properties, whereas its impact on the structural properties is relatively less pronounced.

The Ti-O bond lengths (d_{Ti-O}) for A-TiO₂ were also determined. Consider that the number in parentheses refers to the equivalent bonds within the unit cell. Within the DFT framework, using SCAN+rVV10+U ($U=5.3$ eV), the bond lengths were $d_{Ti-O} = 1.95$ Å (4), 1.99 Å (2). For r^2 SCAN+rVV10+U ($U=5.15$ eV), the obtained lengths were $d_{Ti-O} = 1.97$ Å (4), 2.01 Å (2). On the other hand, employing the DFTB approach, GFN1-xBT yielded bond lengths of $d_{Ti-O} = 1.79$ Å (4), 2.24 Å (2). According to calculations performed using local density approximation (LDA) and Perdew-Wang (PW91) functionals¹³⁵, the resulting bond lengths are $d_{Ti-O(LDA)} = 1.90$ Å (4), 1.96 Å (2), and $d_{Ti-O(PW91)} = 1.93$ Å (4), 1.99 Å (2), respectively. Comparatively, the meta-GGA SCAN functional reproduced the bond lengths reported by both LDA and PW91 with better agreement.

Fig. 4.2 illustrates the PDOS for Bulk A-TiO₂ computed with SCAN+rVV10+U, revealing this material's semiconductor nature. The upper part of the valence band is predominantly influenced by the oxygen from the $O - p_{y,z,x}$ orbitals with minor Ti 3d states contribution near the Fermi level. In contrast, the lower part of the conduction band presents a strong presence of Ti- d_{xy,xz,yz,x^2-y^2,z^2} at ~ 3.15 eV, which facilitates the electron mobility. From Crystal Field Theory, it is known that the d orbitals of a transition metal oxide, such as TiO₂ under an octahedral arrangement, can be split into two sets with different energies. In this sense, the conduction band is divided in the t_{2g} (dx_y, dx_z, dy_z) and the e_g level ($dx^2 - y^2, dz^2$)¹³⁶. The orbital contributions of e_g together with O p form the σ bonding in the low energy region of the valence band, while t_{2g} form π bonds with O p states in the middle region of the valence band. The orbital resolved density of states for SCAN and r^2 SCAN is fully described in Appendix A.

The meta-GGA functionals employed in this study yielded band gap values consistent with each other and provided a very similar description of the electronic structure in both the valence and conduction bands. However, the intensity of the main peak in terms of states per eV of the conduction part presented in the case of SCAN is less than the one shown with r^2 SCAN functional (Fig.4.3).

On the other hand, the PDOS of the bulk calculated with GFN1-xTB (Fig. 4.4) showed its main peak in the valence part at ~ -1.20 eV, while in the conduction part, it located at ~ 1.3 eV. The band gap was underestimated by around 0.7 eV compared to the experimental value in Table 4.1. The DFTB+ framework provides a less detailed electronic description than the DFT functionals. However, it yields reasonable results that can offer important information for a preliminary description of the relative changes in the electronic structure across various configurations. In addition, it requires reduced computational resources and shorter computational time, which makes it suitable for studying our targeted systems.

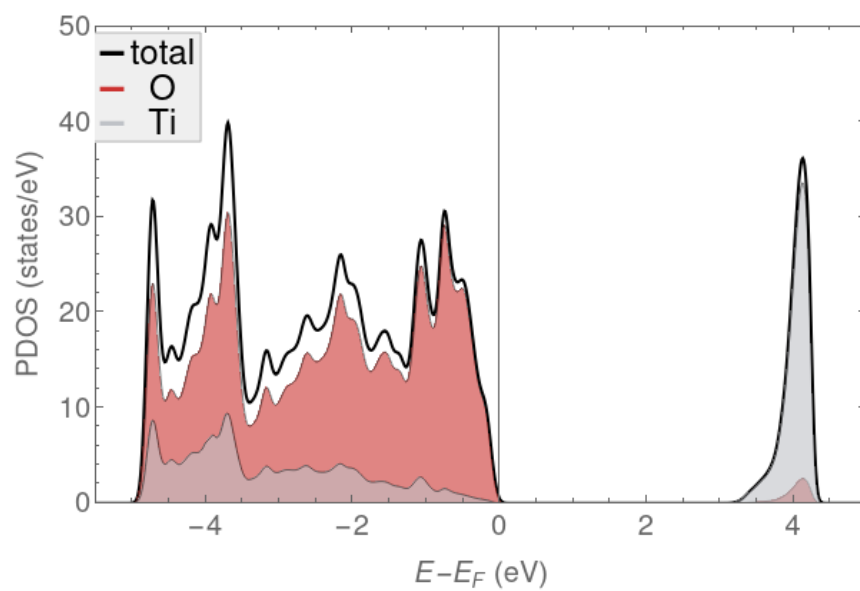


Figure 4.2: Partial Density of States (PDOS) of Bulk Anatase TiO_2 after relaxation using SCAN+rVV10+U functional.

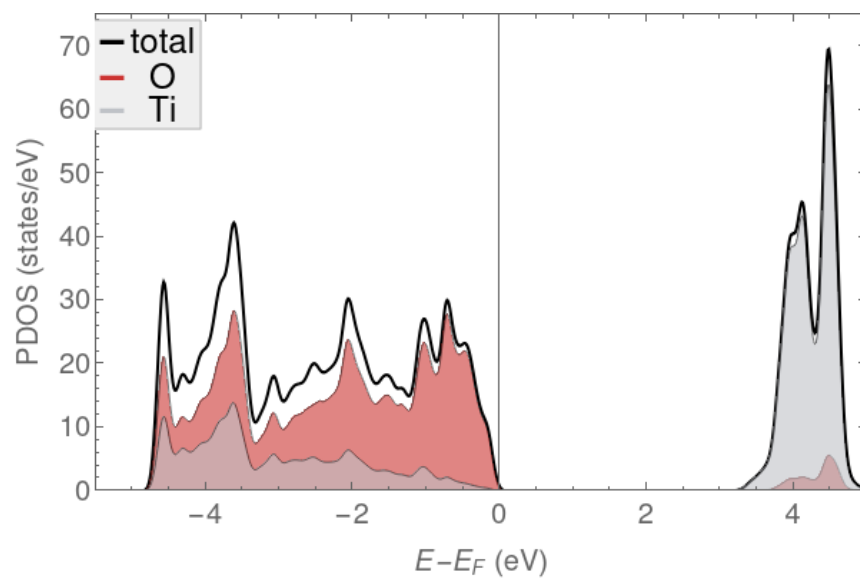


Figure 4.3: Partial Density of States (PDOS) of Bulk Anatase TiO_2 after relaxation using r^2 SCAN+rVV10+U functional.

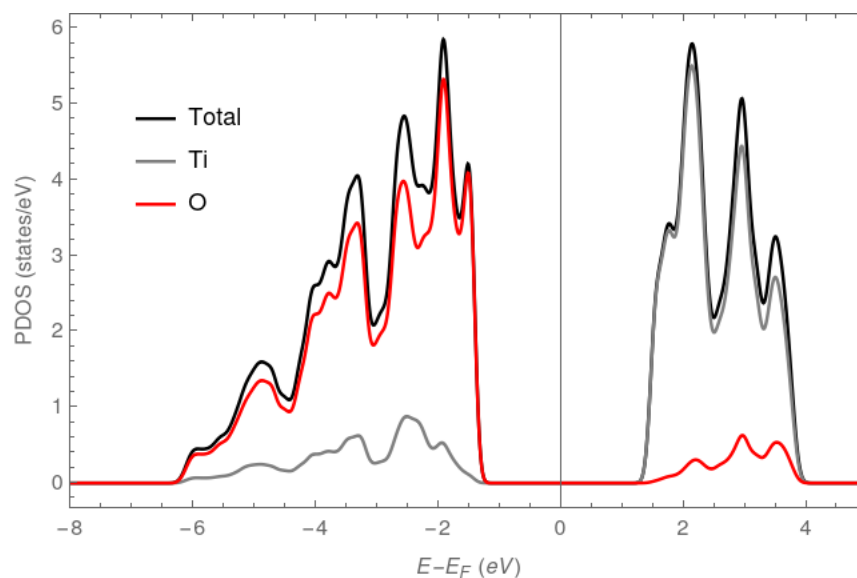


Figure 4.4: Partial Density of States (PDOS) of Bulk Anatase TiO_2 after relaxation using GFN1-xBT functional.

4.2 DFTB+ simulations

4.2.1 Pristine A- $TiO_2(101)$ - $c(4 \times 2)$

Resulting optimized structure for A- $TiO_2(101)$ - $c(4 \times 2)$ is shown in Fig. (4.5). The equilibrium lattice parameters were $a=b=13.29 \text{ \AA}$ and $c=30 \text{ \AA}$. Fermi level is found at $E_F = -10.61 \text{ eV}$, and the computed total energy of the system is $E_{tot} = -14130.77 \text{ eV}$. It is inferred that the major contribution in the valence band is given by the 2p states of the oxygen atoms, while in the conduction band, the key role is played by the 3d states of the Ti atoms. The band gap for the A- $TiO_2(101)$ surface resulted in $E_{bg} = 1.75 \text{ eV}$, which is . As discussed earlier, A- TiO_2 is a partially covalent semiconductor that generally contains dangling bonds associated with under-coordinated Ti atoms when presented on surfaces. These dangling bonds are the unpaired bonds that result from the unsatisfied valence of an atom and produce charge carrier trapping, thus making the band gap of the A- $TiO_2(101)$ slab smaller in comparison to the bulk A- TiO_2 ($E_{bg} = 2.49 \text{ eV}$). In this scenario, the presence of surface states introduces shoulders at the edge of the conduction band minimum and shifts it to $\sim 0.5 \text{ eV}$. In contrast, the position of the valence band edge does not undergo a significant shift.

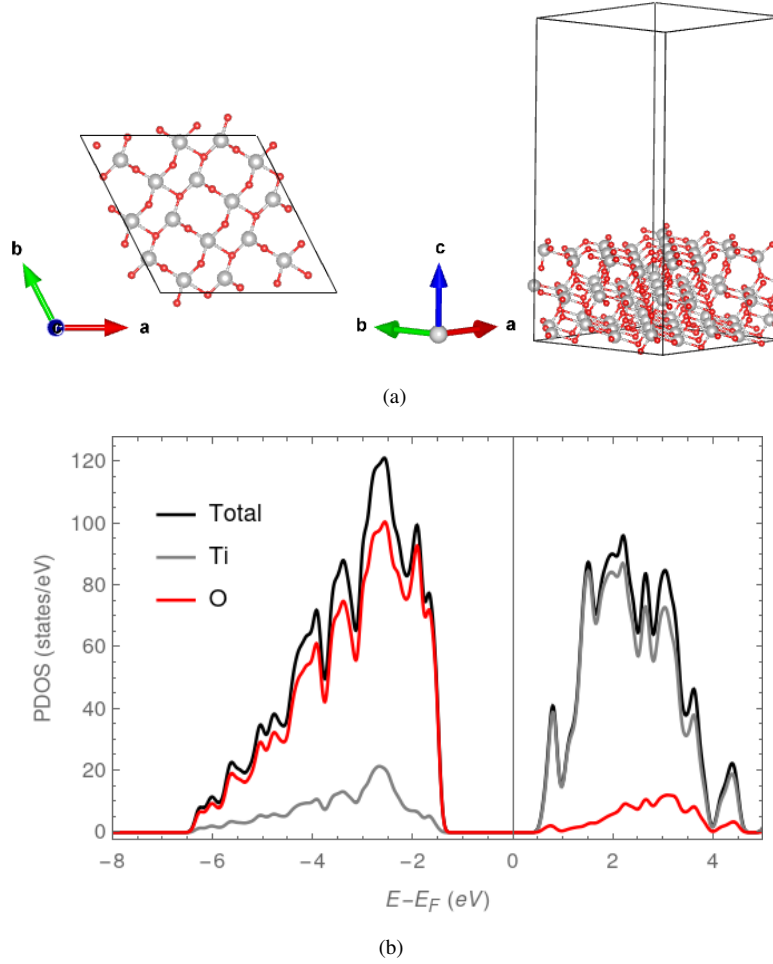


Figure 4.5: (a) Top view of the outermost layer and side view of the fully relaxed supercell. (b) Partial Density of States (PDOS) of pristine $A\text{-TiO}_2(101)\text{-}c(4 \times 2)$ using xBT method.

4.2.2 Oxygen defective $A\text{-TiO}_2(101)\text{-}c(4 \times 2)$

Similar to the pristine system, the titanium atoms make the main contributions to the conduction band. Fermi level is found at $E_F = -10.37$ eV, and the computed total energy of the system is $E_{tot} = -14002.11$ eV. As expected, the energy value is higher than the non-defective surface, potentially signifying a less stable configuration. This indicates that the formation of an oxygen vacancy is energetically costly. Moreover, introducing the oxygen vacancy probably causes slight local lattice distortions, which propagate to the surrounding structure and can be observed through changes in the Ti-O bond lengths near the defect. In the pristine $A\text{-TiO}_2(101)$ the shortest distance is $d_{\text{Ti-O}} = 1.69$ Å, whereas in the oxygen defective $A\text{-TiO}_2(101)$ it is reduced to $d_{\text{Ti-O}} = 1.67$ Å.

Removing an oxygen atom induces a slight shift of the energy peaks and the appearance of new states near the Fermi level, suggesting trap states. The Ti atoms experience an induced charge due to the vacancy, which generates the states near the conduction band, known as localized states. These states are around ~ 0.45 eV below the Fermi level. The oxygen vacancy broke the octahedral arrangement, in which the Ti atom is surrounded by six O atoms and thus gives rise to two fourfolding coordinated Ti atoms. This results in dangling bonds and induces the Ti species to reduce from Ti^{4+} to Ti^{3+} . Consequently, an increase in electron concentration in the system leads to electronic states within the band gap. The band gap for this configuration is ~ 1.70 eV, which is slightly lower than that obtained for stoichiometric anatase.

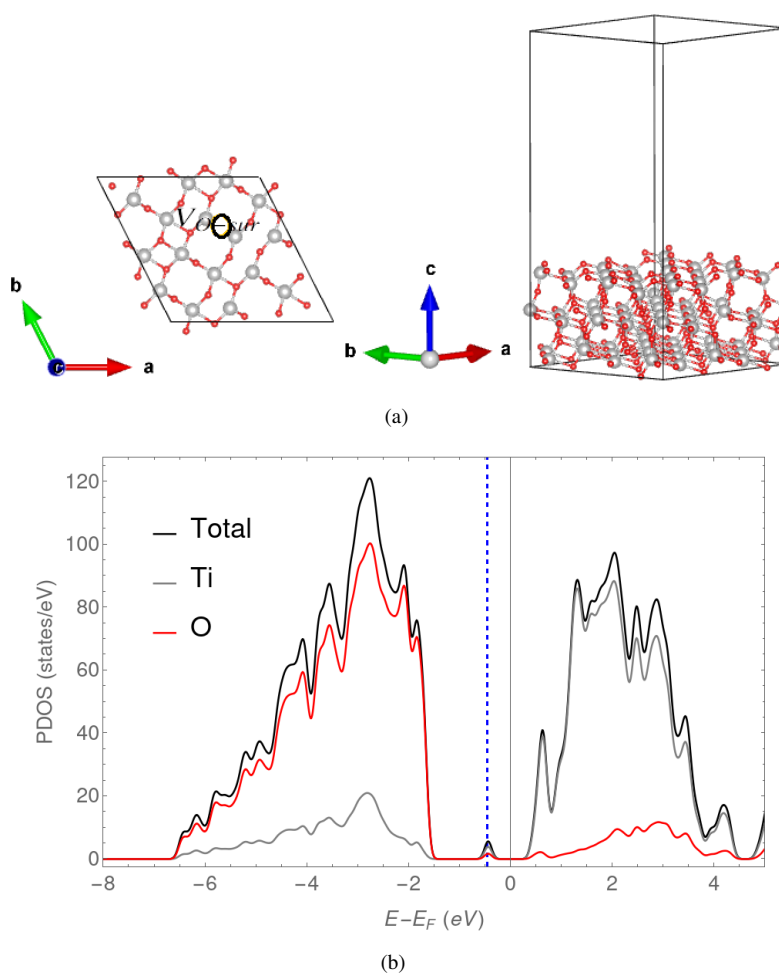


Figure 4.6: (a) Top view of the outermost layer and side view of the fully relaxed supercell. (b) Partial Density of States (PDOS) of oxygen defective $A-TiO_2(101)-c(4 \times 2)$ using xBT method. The dashed blue line indicates the introduction of new localized states close to the Fermi level.

4.2.3 Single-Metal nanoclusters@A-TiO₂(101)

The system in Fig. (4.7) takes into account a cluster of 8 gold atoms supported on A-TiO₂(101), which was allowed to relax until convergence in the global system was reached. The distance of the closest Au to Ti atom is $d_{Au-Ti} = 2.57$ Å, and to an O atom $d_{Au-O} = 2.23$ Å. In addition, we have observed some structural changes on the surface as there is a shortening of the Ti-O bond length to $d_{Ti-O} = 1.67$ Å (reference Ti-O bond in the subsurface) compared to that present on the pristine undoped surface. The cluster atoms adopt an almost flat central pentagonal arrangement with a shortest Au-Au bond of $d_{Au-Au} = 2.56$ Å.

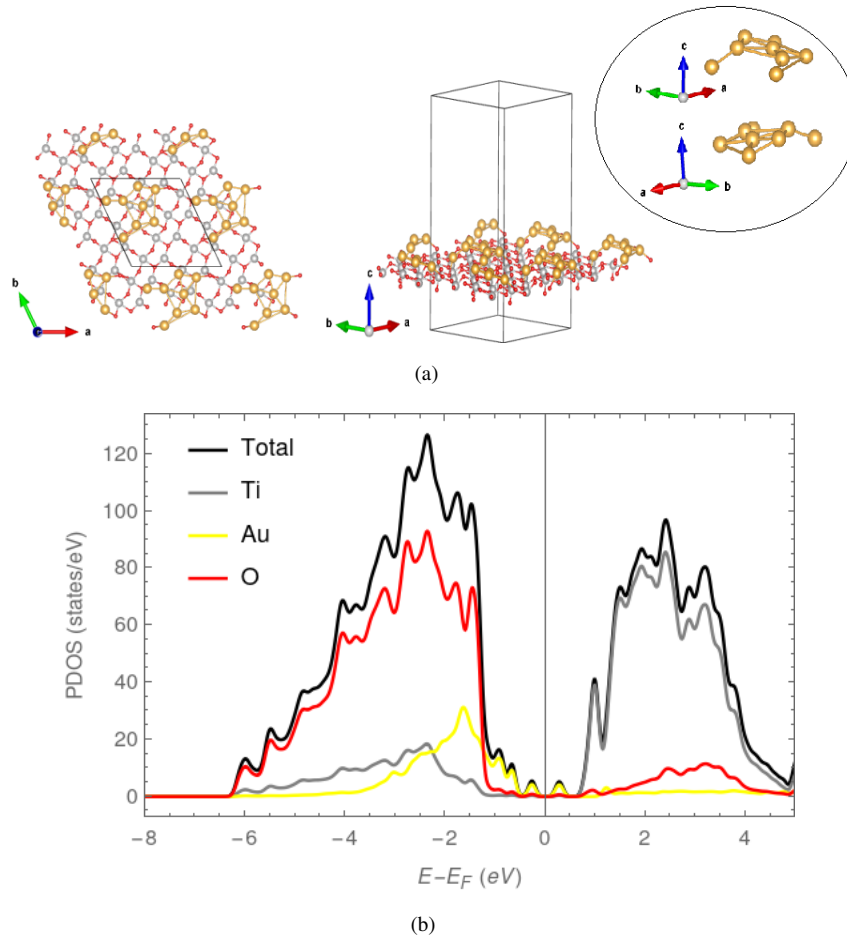


Figure 4.7: (a) Top view of the outermost layer and side view of the optimized geometry. (b) Partial Density of States (PDOS) of Au₈ cluster supported on stoichiometric A-TiO₂(101)-c(4 × 2).

The presence of gold atoms and the contribution of their electron transfer tune the electronic behavior within the

forbidden energy range. It should be noted that the effect of single Au atoms on A-TiO₂(101) is well known in the literature, in which the contribution of the 5d states of Au generates the creation of new energetic states within the band gap¹³⁷. Since we are studying a cluster composed of multiple gold atoms, we can infer that introducing additional atoms into the system could form more pronounced and complex electronic states than those from individual Au atoms. The cluster-surface system presents a higher number of interactions among the gold atoms themselves and with the Ti and O atoms, creating a larger number of defect states with a more delocalized nature. This cluster size could show slight localized surface plasmon resonance effects however, as this is a size-dependent phenomenon, in general, Au₈ is not large enough (around 0.8 nm) to show strong and well-defined plasmonic effects, as it has been shown that a threshold of around 2 nm is required for gold clusters¹³⁸. The greatest contribution of gold is in the valence part, but still, the contribution of the O 2p states is much higher. Fermi level is found at $E_F = -10.26$ eV, and the computed total energy of the system is $E_{tot} = -15009.41$ eV. The highest density of these new states is found near the valence band edge, and the closest states to the fermi level are located at -0.27 eV and 0.27 eV. Regardless of the localized states, the band gap energy is $E_{bg} = 1.06$ eV. The valence band edge is at -0.45 eV, and the conduction band edge is at 0.61 eV. Regarding the adsorption mechanism, two phenomena are physisorption and chemisorption. Physisorption is governed by weak Van der Waals forces, while chemisorption requires higher adsorption energy since it involves the establishment of new chemical bonds. In this work, we assume that chemisorption occurs when $E_{ads} > 0.5$ eV¹³⁹. According to our calculations, Au₈ is adsorbed by chemisorption. More information about energetic parameters can be found in Table 4.2.

Similarly, other noble metals (Ag, Pd, and Pt) were used for cluster construction to compare their influence on generating excited states. As seen in Fig 4.8, the Ag₈ cluster adopted a planar geometry anchored to the surface. The longest distance of the Ag-Ag atoms is $d_{Ag-Ag} = 8.16$ Å. It was observed that Ag atoms prefer to bind to surface oxygen ($d_{Ag-O} = 2.21$ Å) rather than bind to other Ag ($d_{Ag-Ag} = 2.73$ Å) or Ti cations ($d_{Ag-Ti} = 2.64$ Å). New localized states appeared within the band gap after introducing the Ag cluster. The state closest to the fermi level is found at -0.64 eV. The Fermi level is within the conduction band, suggesting metallic behavior of the Ag₈ system. The valence band edge is at -1.53 eV, and the conduction band edge is at -0.32 eV. Most of the Ag contribution lies at the top of the valence band, showing a strong interaction with O atoms. It has been found that Ag₈ is adsorbed by chemisorption.

On the other hand, Pd₈ and Pt₈ clusters (see Fig. 4.9, Fig. 4.10) adopted the shape of a pentagonal-pyramid with 2 adjacent atoms forming a flat, tilted layer, and a saddle shape, respectively. It was also observed that Pd atoms prefer to bind to surface oxygen ($d_{Pd-O} = 2.27$ Å) rather than bind to other Pd ($d_{Pd-Pd} = 2.49$ Å) or Ti cations ($d_{Pd-Ti} = 2.47$ Å). Additionally, the longest distance of the Pd-Pd atoms is $d_{Pd-Pd} = 6.03$ Å, and for Pd-O is $d_{Pd-O} = 3.69$ Å. There is an elongation of the Ti-O bond length to $d_{Ti-O} = 1.71$ Å (reference Ti-O bond in the subsurface with $d_{Ti-O} = 1.69$ Å). From the PDOS presented in Fig.4.9 (b), it is noticeable that a broad state is created within the band gap by an increased contribution of Pd. The highest peak of these defective states is located at -0.62 eV. The contribution of Pd 4d orbitals is extended to the valence band edges, and overlap with possible hybridized states involving Pd 4d and O 2p orbitals can be observed.

A similar scenario is presented in the case of Pt₈. The Pt atoms tend to approach the surface oxygens ($d_{Pt-O} = 2.14$ Å) rather than prefer other Pt ($d_{Pt-Pt} = 2.42$ Å) or Ti cations ($d_{Pt-Ti} = 2.59$ Å). The longest distance between

Pt-Pt atoms is $d_{Pt-Pt} = 5.60 \text{ \AA}$, and for Pt-O is $d_{Pt-O} = 4.49 \text{ \AA}$. The $Pt_8@A-TiO_2(101)$ system (Fig.4.10 (b)) also presents a broad energy level within the band gap due to the Pt contribution, and extends it to the valence band edge. A considerable presence of states located at the conduction band edge is observed, with a higher contribution of noble metals with respect to the Pd_8 system. This can be related to the structural findings discussed above, in which it was found that the metal-oxygen bonding distance was smaller in the case of platinum compared to the other metals studied, suggesting that the Pt orbitals found along the valence and conduction band hybridize effectively with O 2p orbitals promoting covalent bonding. The closest localized state to the fermi level is located at -0.24 eV .

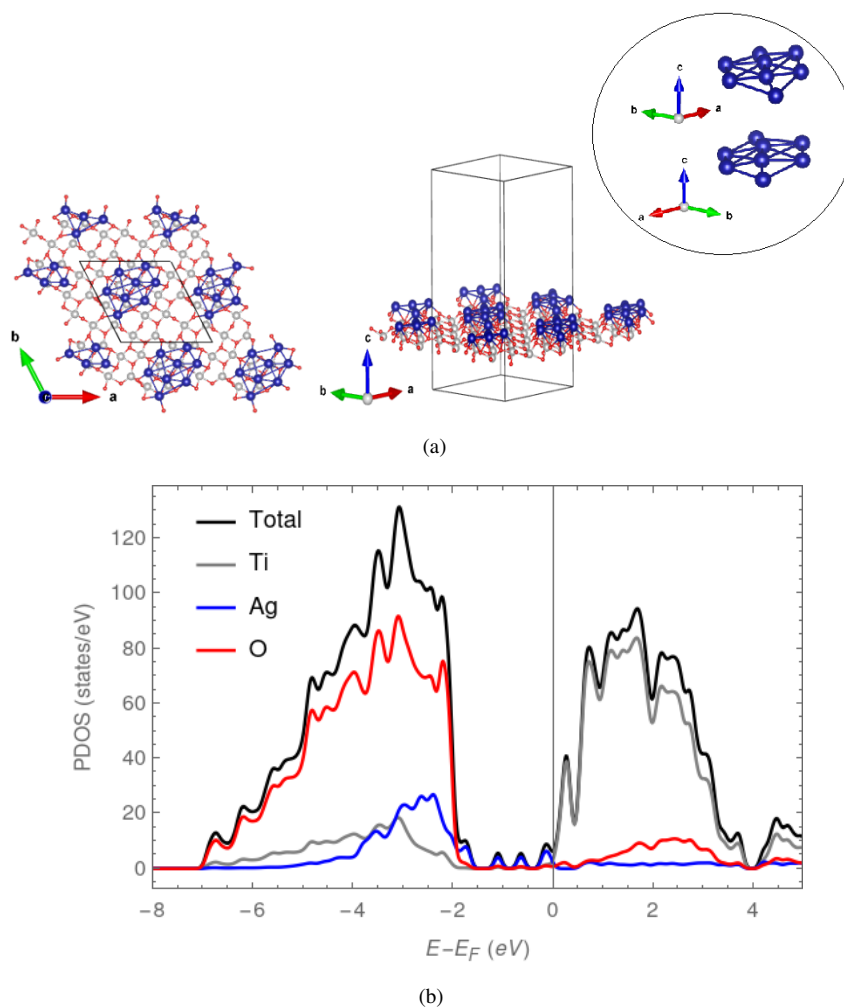


Figure 4.8: (a) Top view of the outermost layer and side view of the optimized geometry. (b) Partial Density of States (PDOS) of Ag_8 cluster supported on stoichiometric $A-TiO_2(101)-c(4 \times 2)$.

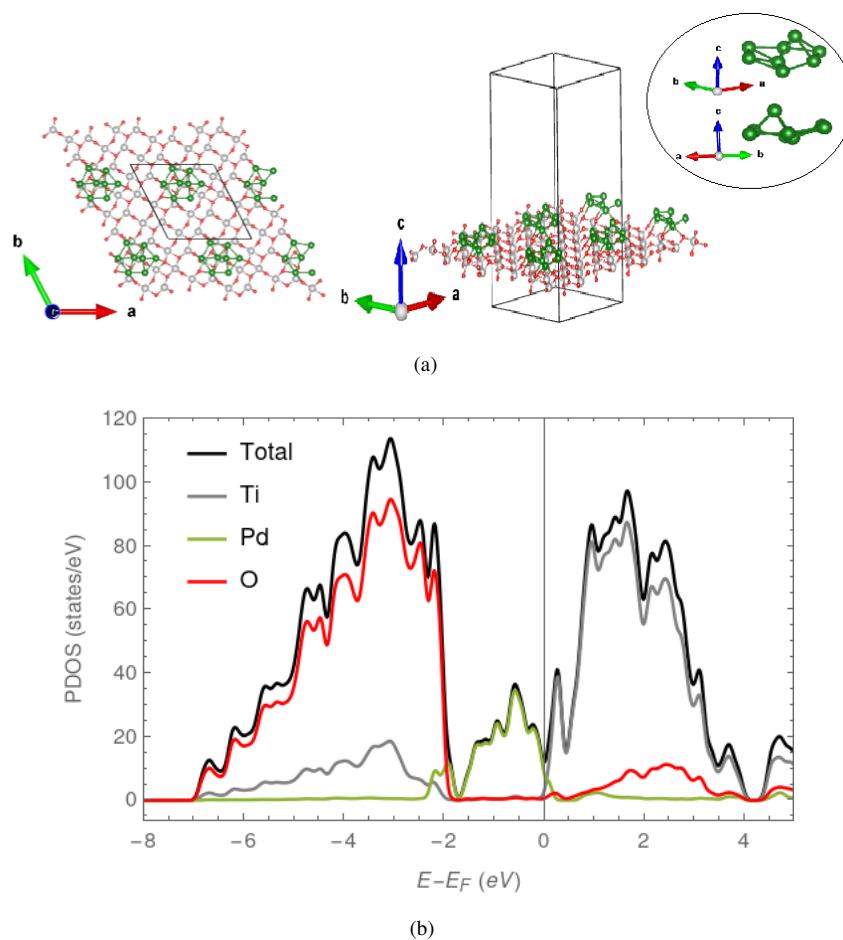


Figure 4.9: (a) Top view of the outermost layer and side view of the optimized geometry. (b) Partial Density of States (PDOS) of Pd_8 cluster supported on stoichiometric $A-TiO_2(101)-c(4 \times 2)$.

The order of adsorption energy for the clusters considering a pristine substrate from highest to lowest is: Ag ($\Delta E_{Ads} = 15.29$ eV) > Pd ($\Delta E_{Ads} = 13.49$ eV) > Au ($\Delta E_{Ads} = 12.53$ eV) > Pt ($\Delta E_{Ads} = 3.93$ eV). This indicates that the Ag cluster is much more tightly bound to the surface, making it less likely to desorb than the Pt cluster. The Pd_8 and Pt_8 clusters are also adsorbed by chemisorption. As for the electronic contributions, the Ag cluster behaves similarly to the Au cluster within the band gap by creating localized energy levels. However, when introducing Ag atoms, the new energy levels become visible at both the valence and conduction band edge, in contrast to the Au cluster system, which mainly affects the valence band edge. The Pd cluster has the largest contribution compared to the others in the excited states. The magnitude of the localized states in the Pd system could indicate that the charge carrier trapping is higher in this system compared to clusters based on the other noble metals. The contribution of the Pt atoms in the lower part of the valence band suggests that electrons are available for conduction.

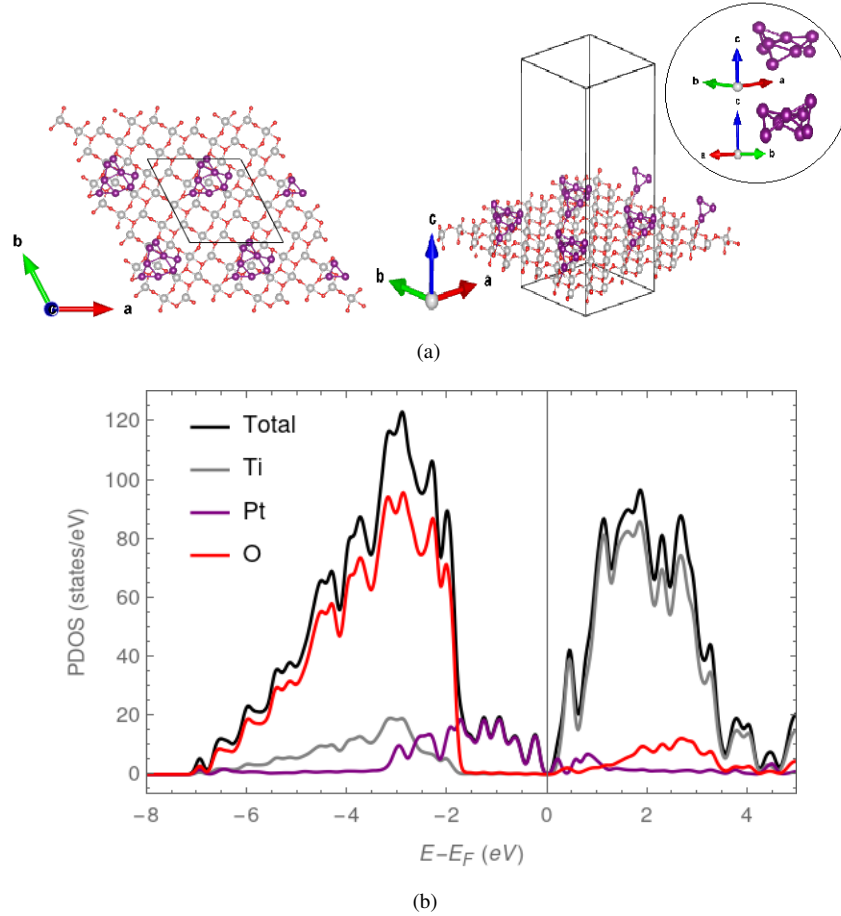


Figure 4.10: (a) Top view of the outermost layer and side view of the optimized geometry. (b) Partial Density of States (PDOS) of Pt_8 cluster supported on stoichiometric $A-TiO_2(101)-c(4 \times 2)$.

4.2.4 Single-Metal nanoclusters@A-TiO₂(101)+V_{O-sur}

For the Au_8 system supported on defective oxygen $A-TiO_2(101)$, the shortest distance of the Au atom to surface oxygen is $d_{Au-O} = 2.23 \text{ \AA}$, resulting in the same value as the Au_8 cluster on the stoichiometric surface. The metal-metal shortest bond is $d_{Au-Au} = 2.60 \text{ \AA}$, while the longest distance between Au-Au atoms is $d_{Au-Au} = 8.84 \text{ \AA}$. The metal-Ti shortest bond is $d_{Au-Ti} = 2.49 \text{ \AA}$. There is an elongation of the Ti-O bond length to $d_{Ti-O} = 1.71 \text{ \AA}$ (reference Ti-O bond in the subsurface near to the oxygen vacancy with $d_{Ti-O} = 1.67 \text{ \AA}$). In general, the Au_8 cluster adopts a planar shape, and one of the gold atoms sits near the vacancy, affecting the distribution of nearby atoms by causing them to disperse more than on the stoichiometric surface.

The band gap is $E_{bg} = 0.98 \text{ eV}$ (without considering the new states), which is narrower than the one calculated for

the case of gold supported on non-defective anatase. The valence band edge is at -0.82 eV, and the conduction band edge is at 0.16 eV. The highest density of these new states is found near the valence band edge, and the states located within the band gap appear below the fermi level and are located at -0.36 eV and -0.70 eV. This system exhibits higher adsorption energy than Au_8 supported on anatase without oxygen vacancy.

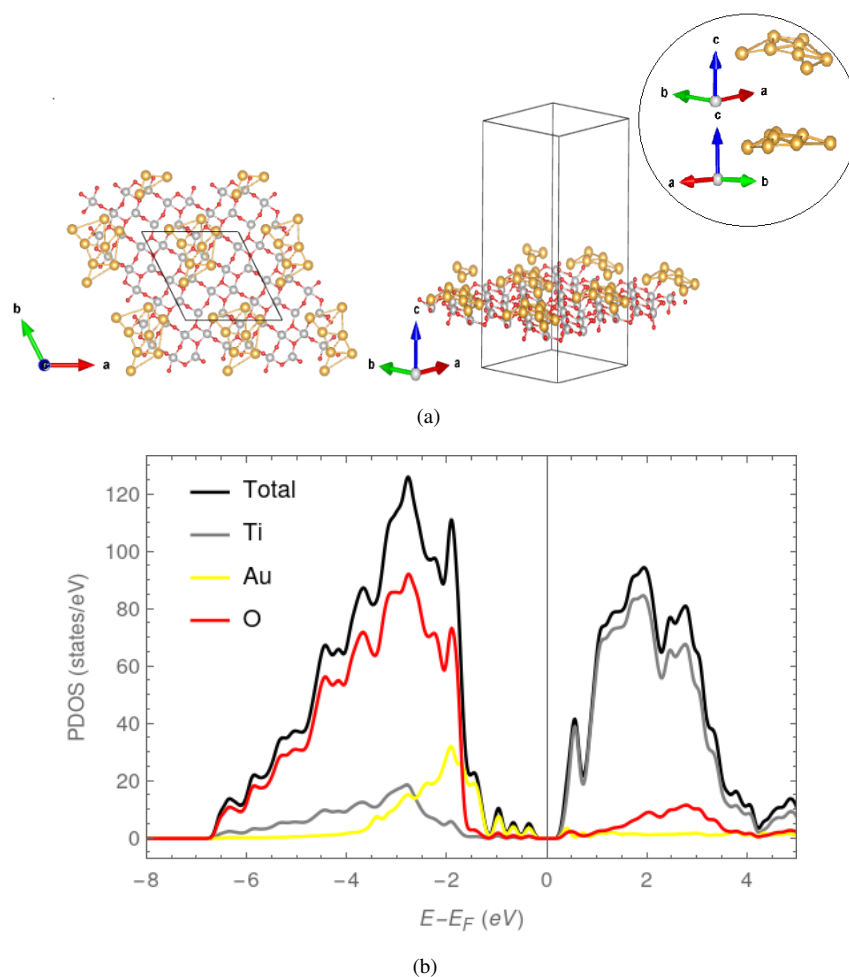


Figure 4.11: (a) Top view of the outermost layer and side view of the optimized geometry. (b) Partial Density of States (PDOS) of Au_8 cluster supported on oxygen defective A- $TiO_2(101)-c(4 \times 2)$.

For the Ag_8 cluster supported on defective anatase, the shortest Ag-O bond length is $d_{Ag-O} = 2.29 \text{ \AA}$, and the metal-Ti distance is $d_{Ag-Ti} = 2.53 \text{ \AA}$, with the Ag-Ti distance being shorter when an oxygen vacancy is introduced. The Ag atoms are strongly bonded to neighboring oxygen atoms. The metal-metal shortest bond is $d_{Ag-Ag} = 2.79 \text{ \AA}$, while the longest distance is $d_{Ag-Ag} = 10.41 \text{ \AA}$. There is a slight elongation of the Ti-O bond length to $d_{Ti-O} = 1.68$

Å (reference Ti-O bond in the subsurface near to the oxygen vacancy with $d_{Ti-O} = 1.67$ Å). One Ag atom is located near the vacancy while neighboring Ag atoms appear to scatter in the same direction. The result is a disordered configuration with more pronounced displacement in the z direction, compared to the nearly flat cluster observed on the non-defective system. In addition, the vacancy exerts a force on the adjacent Ti atoms, causing them to move downward.

The closest state near the fermi level is visibly broader than the one presented in Fig. 4.8. This new energy level appears as an independent and more pronounced state, not a contribution to the conduction band. The valence band edge is at -1.79 eV and presents a considerable sharp peak of Ag contribution. In addition, the bottom of the conduction is located at -0.20 eV; this is shifted to the left by ~ 0.12 eV compared to the Ag cluster supported on the defect-free surface. The closest localized state near the fermi level is at -0.34 eV.

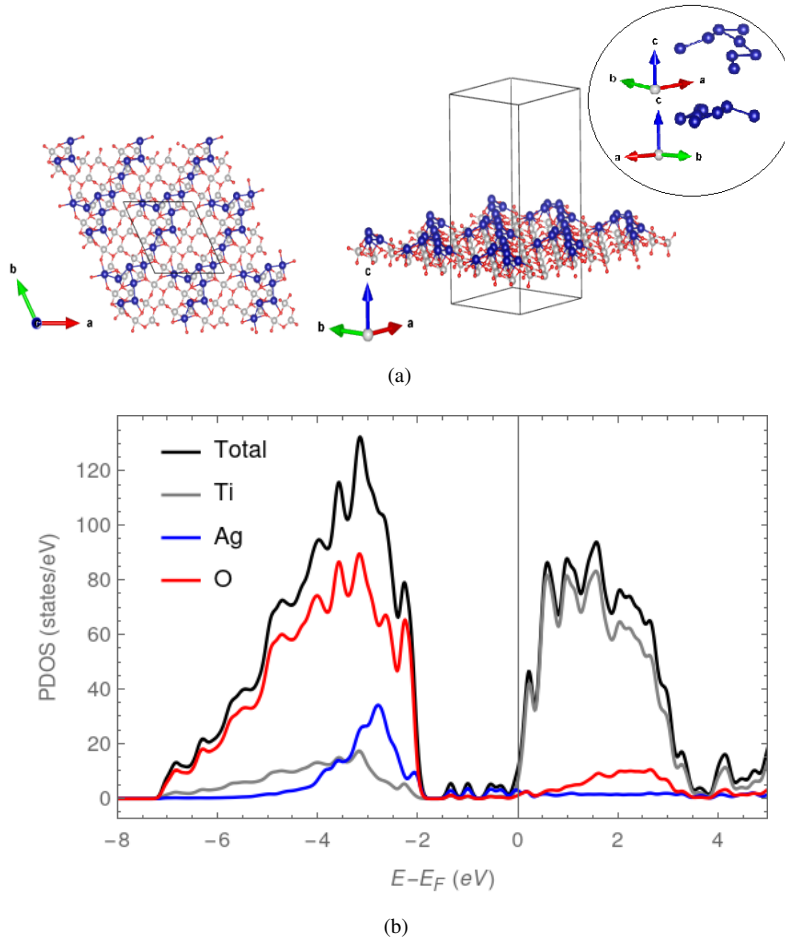


Figure 4.12: (a) Top view of the outermost layer and side view of the optimized geometry. (b) Partial Density of States (PDOS) of Ag_8 cluster supported on oxygen defective $A-TiO_2(101)-c(4 \times 2)$.

In Pd_8 system, the shortest Pd-O bond length is $d_{Pd-O} = 2.27 \text{ \AA}$ while the largest distance is $d_{Pd-O} = 4.37 \text{ \AA}$, the latter being larger than in the case of the stoichiometric surface. The metal-metal distance is $d_{Pd-Pd} = 2.56 \text{ \AA}$, whereas the longest distance between Pd-Pd atoms is $d_{Pd-Pd} = 5.50 \text{ \AA}$. The metal-Ti distance is $d_{Pd-Ti} = 2.46 \text{ \AA}$. There is a slight elongation of the Ti-O bond length to $d_{Ti-O} = 1.68 \text{ \AA}$ (reference Ti-O bond in the subsurface near to the oxygen vacancy with $d_{Ti-O} = 1.67 \text{ \AA}$). The cluster results in a shape similar to that described for the non-defective surface but with greater height and a steeper slope due to the local charge imbalance in the crystal lattice caused by the missing oxygen. Upon introducing Pd atoms, a defect state emerges within the band gap, and additional states appear in the valence band, although not as close to the edge as non-defective anatase. The contribution of Pd within the band gap is broader, but the intensity of the highest peak is less pronounced.

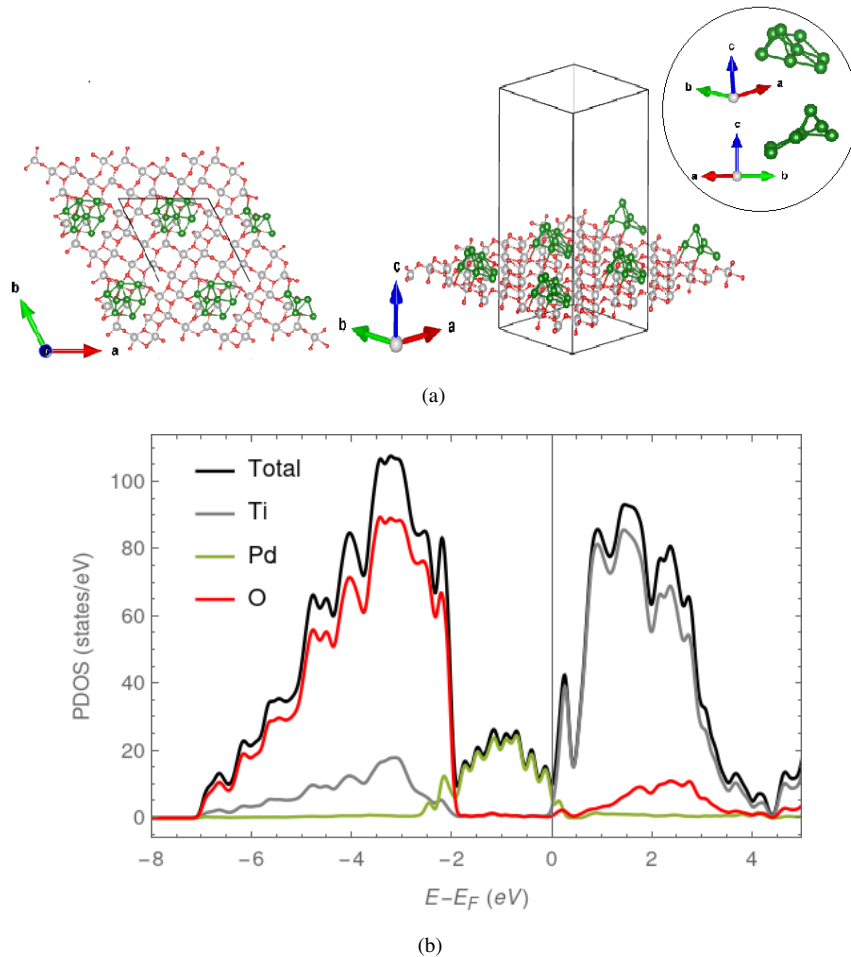


Figure 4.13: (a) Top view of the outermost layer and side view of the optimized geometry. (b) Partial Density of States (PDOS) of Pd_8 cluster supported on oxygen defective A- $TiO_2(101)-c(4 \times 2)$.

In Pt_8 system, the shortest Pt-O bond length is $d_{Pt-O} = 2.52 \text{ \AA}$. The metal-metal distance is $d_{Pt-Pt} = 2.41 \text{ \AA}$, whereas the longest distance between Pt-Pt atoms is $d_{Pt-Pt} = 6.59 \text{ \AA}$. The metal-Ti distance is $d_{Pt-Ti} = 2.61 \text{ \AA}$. There is an elongation of the Ti-O bond length to $d_{Ti-O} = 1.71 \text{ \AA}$ (reference Ti-O bond in the subsurface near to the oxygen vacancy with $d_{Ti-O} = 1.67 \text{ \AA}$). The morphology of the cluster is more ordered and resembles a flat hexagonal configuration. Although flat, the cluster is tilted, with the lower part near the vacancy and showing a greater height farther away from the vacancy. The defective states within the band gap present less defined peaks, while their contribution near the valence band edge shows a similar intensity to that of the non-defective system. In addition, Pt has a minor contribution near the conduction band edge. The closest sharp localized state to the fermi level is at -0.81 eV .

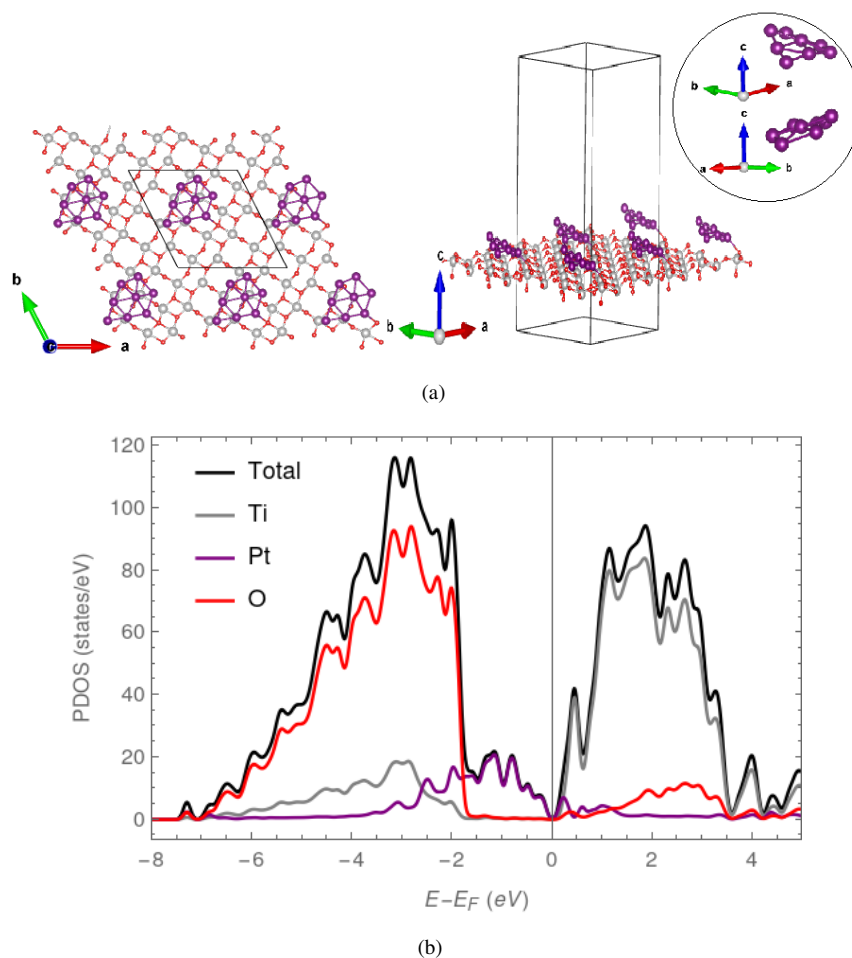


Figure 4.14: (a) Top view of the outermost layer and side view of the optimized geometry. (b) Partial Density of States (PDOS) of Pt_8 cluster supported on oxygen defective $A-TiO_2(101)-c(4 \times 2)$.

The order of adsorption energy for the clusters considering an oxygen defective surface, from highest to lowest, is Ag ($\Delta E_{Ads} = 16.54$ eV) > Pd ($\Delta E_{Ads} = 14.84$ eV) > Au ($\Delta E_{Ads} = 14.40$ eV) > Pt ($\Delta E_{Ads} = 6.06$ eV). The single metal clusters supported on A- $TiO_2(101)$ with an oxygen vacancy showed higher adsorption energy than the ones obtained for stoichiometric anatase. Adsorption is more stable because oxygen vacancies create localized sites with better electrical interactions and charge imbalances that attract the adsorbate. In contrast, the stoichiometric surface offers fewer reactive sites and weaker interactions due to its well-coordinated structure, which reduces adsorption energies. In both scenarios, the order of the adsorption energies of the metal groups remains constant; thus, the presence of an oxygen vacancy increases the binding but does not change the relative interaction strengths between the different metals. This result can be validated by comparing the contributions of each metal near the valence band edge, where the Ag cluster has the largest contribution and the Pt cluster the smallest.

4.2.5 Multicomponent nanoclusters@Anatase $TiO_2(101)$

The bimetallic system in Fig. 4.15 presents an interesting geometry where the Ag tries to enclose the Pd atoms with a "snail" pattern. The shortest metal-O bond distances are $d_{Ag-O} = 2.24$ Å and $d_{Pd-O} = 2.47$ Å. The Pd atom is preferentially located near the oxygen vacancy, a fact that can be corroborated by comparing the bond distances Ag-O and Pd-O calculated for single metal groups, which are $d_{Pd-O} = 2.27$ Å and $d_{Ag-O} = 2.29$ Å, respectively. Since the Pd-O bond length is shorter, oxygen forms stronger bonds with Pd atoms compared to Ag atoms, so Pd is more likely to position itself towards the vacancy, where it can maximize its bonding with the surrounding oxygen atoms and, in turn, stabilize the local environment. The states in the band gap are characterized by a high contribution of Pd; the upper part of the valence band is governed by Ag atoms, while the conduction band is mainly Ti atoms. The second bimetallic system shown in Fig. 4.16 exhibits an upward-pointing configuration. It combines the pyramidal structure characteristic of the single Pd cluster with the tilted planar arrangement typical of the Pt cluster. The shortest metal-O bond distances are $d_{Pt-O} = 2.17$ Å and $d_{Pd-O} = 2.17$ Å. Similarly, the Pd atom is preferentially located near the oxygen vacancy. The presence of Pd predominantly influences states located within the band gap, although Pt states also contribute. In particular, Pt's contribution is higher than Pd states near the valence band edge.

In the $Au_2Ag_2Pd_2$ trimetallic system from Fig. 4.17, two atoms of Ag, one of Pd and one of Au form the base, which takes the shape of a trapezoid, with a gold atom located at the top of the cluster. The shortest metal-O bond distances are $d_{Au-O} = 2.82$ Å, $d_{Ag-O} = 2.11$ Å and $d_{Pd-O} = 2.44$ Å. Interestingly, the Au atom is preferentially located near the oxygen vacancy. The presence of Pd predominantly influences the states within the band gap, although Au and Ag states also contribute. However, near the valence band edge, the contribution of gold is greater, and in the -2eV to -3eV range, there is a strong presence of Ag states. The $Pd_2Pt_2Ag_2$ cluster (Fig.4.18) displays a U-shaped flat morphology oriented downward. The shortest metal-O bond distances are $d_{Pt-O} = 2.82$ Å, $d_{Ag-O} = 2.11$ Å and $d_{Pd-O} = 2.44$ Å. The Pd atom is preferentially located near the oxygen vacancy. The states within the band gap, which are sharper compared to the other trimetallic clusters, are mainly influenced by the presence of Pd, with Pt exhibiting a comparable density of states in this region, while Ag makes a minor contribution. Near the valence band edge, the contribution of Ag is greater and in the -2eV to -3eV range.

In the $Au_2Pt_2Ag_2Pd_2$ tetrametallic cluster (Fig.4.19), one atom of each noble metal forms the base, while the

second layer, composed of the remaining atoms, adopts a larger rhomboidal shape above the base. The shortest metal-O bond distances are $d_{Au-O} = 2.85 \text{ \AA}$, $d_{Pt-O} = 2.07 \text{ \AA}$, $d_{Ag-O} = 2.27 \text{ \AA}$ and $d_{Pd-O} = 2.35 \text{ \AA}$. The Au atom is preferentially located near the oxygen vacancy. The states within the band gap exhibit their highest peak at -0.54 eV , primarily influenced by Pd, followed by notable contributions from Pt and Ag. Near the bottom of the valence band edge, Au has a strong contribution and a presence of Pt states. In the energy range of -2.5 to -3.5 eV , the contribution from Ag is predominant.

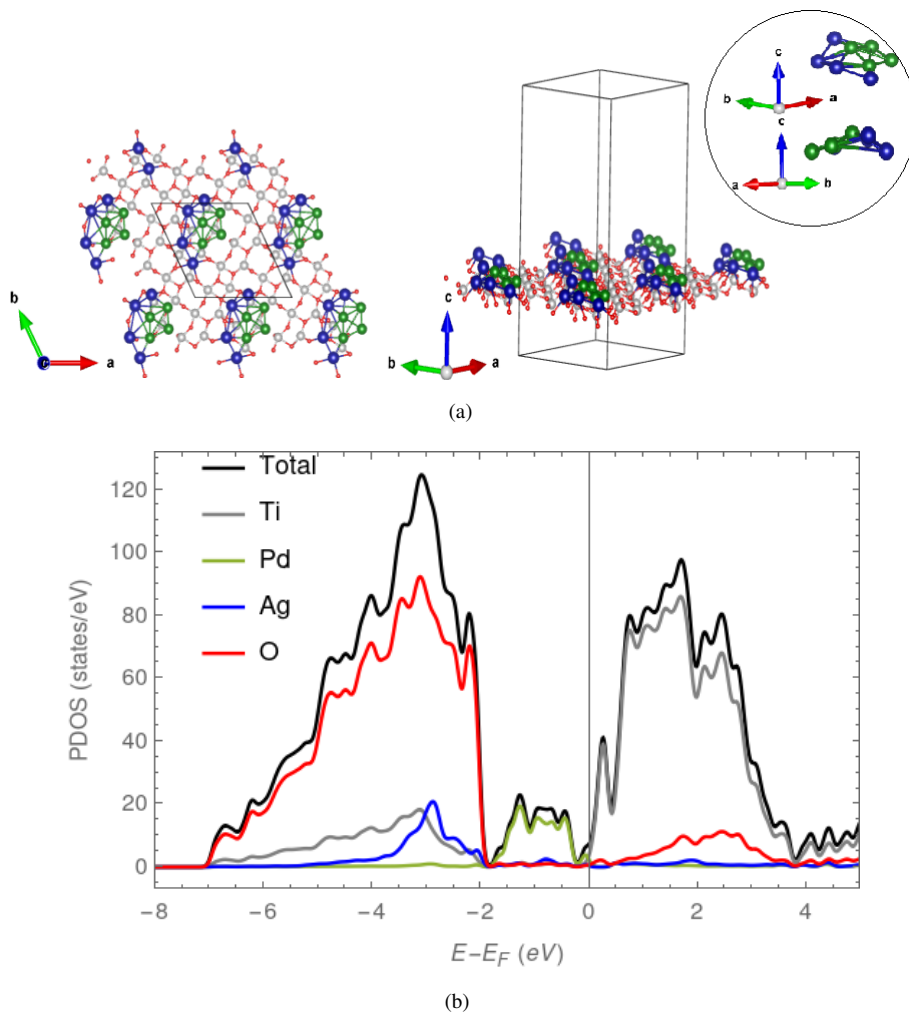


Figure 4.15: (a) Top view of the outermost layer and side view of the optimized geometry. (b) Partial Density of States (PDOS) of bimetallic Pd_4Ag_4 cluster supported on oxygen defective $A-TiO_2(101)-c(4 \times 2)$.

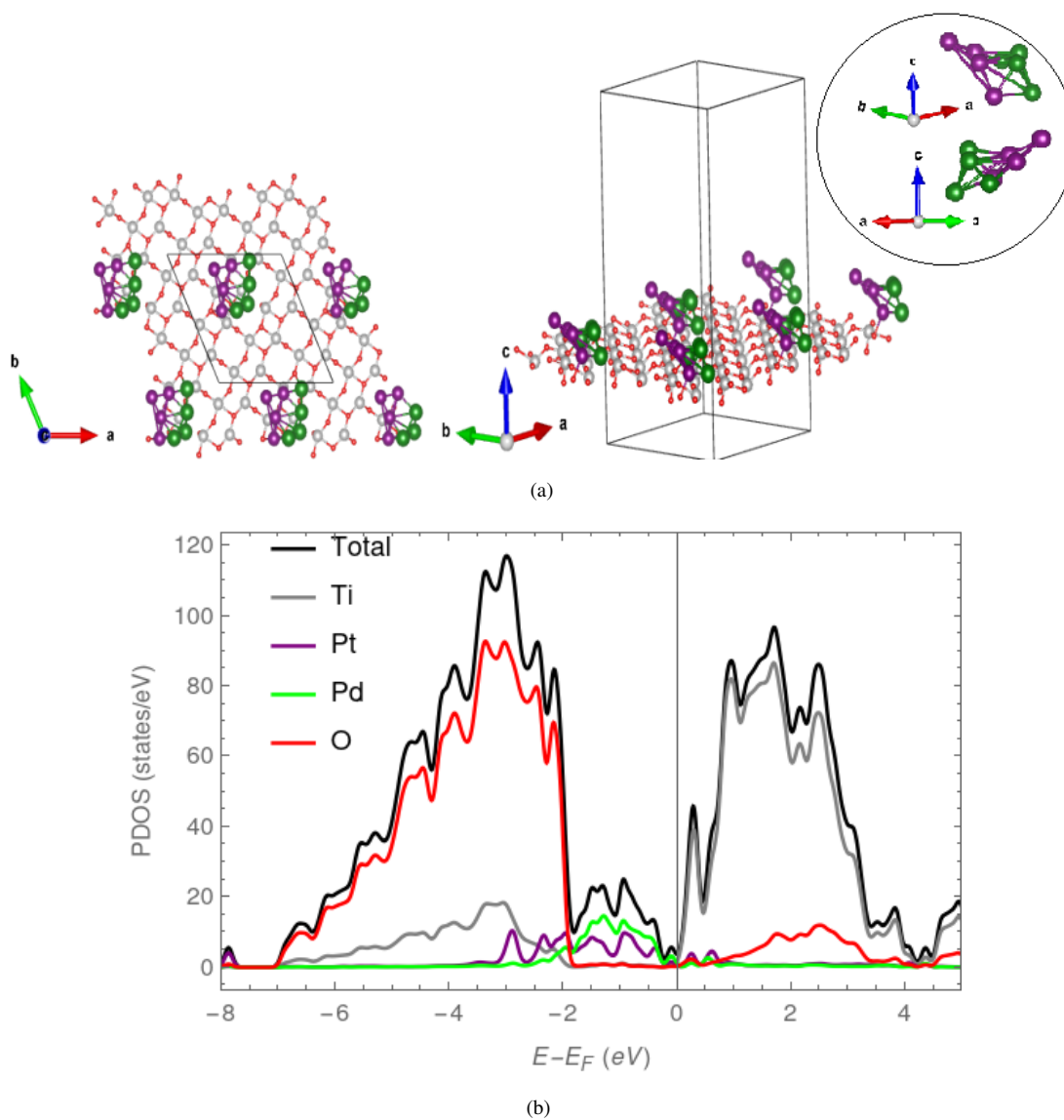


Figure 4.16: (a) Top view of the outermost layer and side view of the optimized geometry. (b) Partial Density of States (PDOS) of bimetallic Pt_4Pd_4 cluster supported on oxygen defective $A-TiO_2(101)-c(4 \times 2)$.

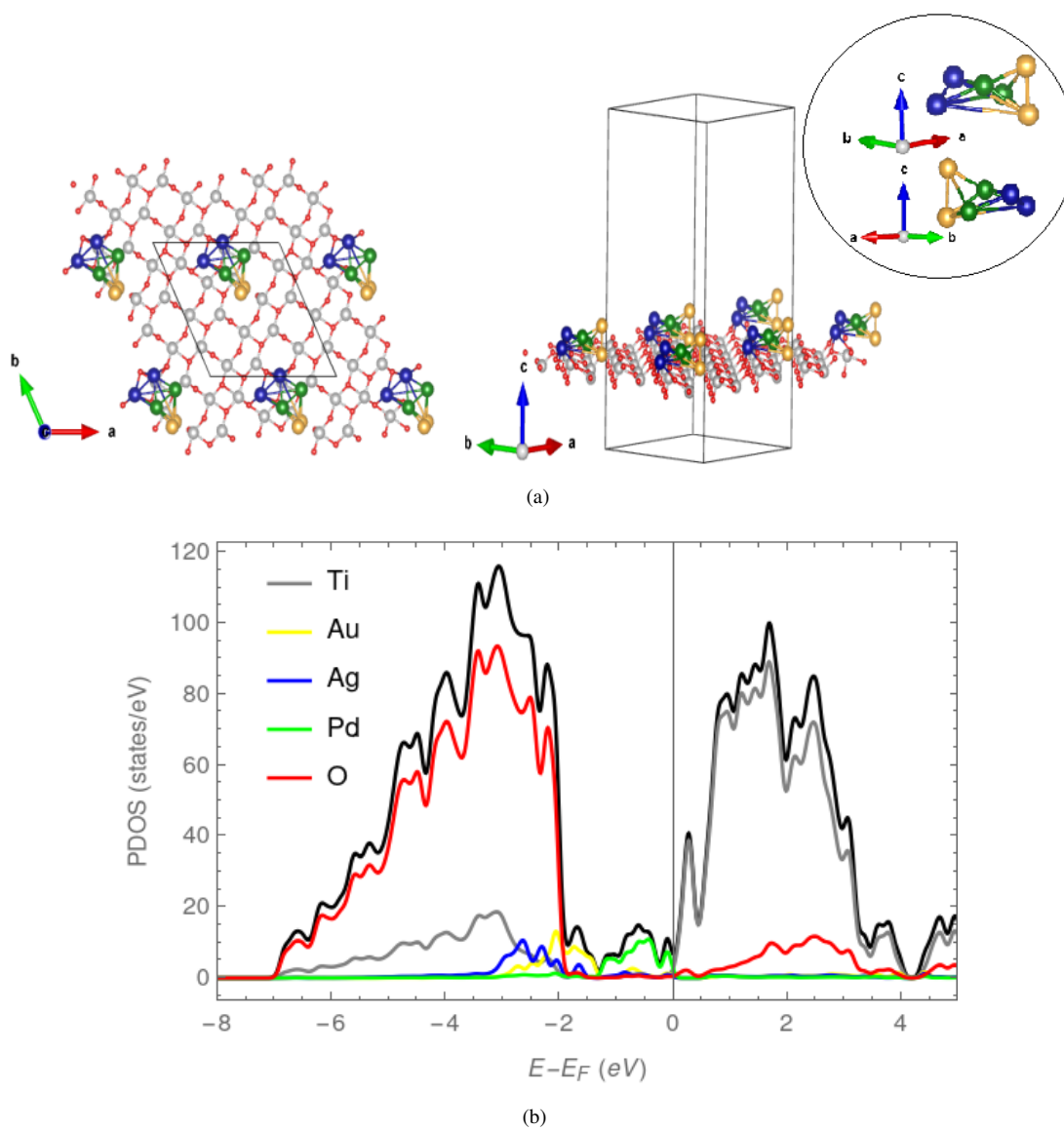


Figure 4.17: (a) Top view of the outermost layer and side view of the optimized geometry. (b) Partial Density of States (PDOS) of trimetallic $Au_2Ag_2Pd_2$ cluster supported on oxygen defective $A-TiO_2(101)-c(4 \times 2)$.

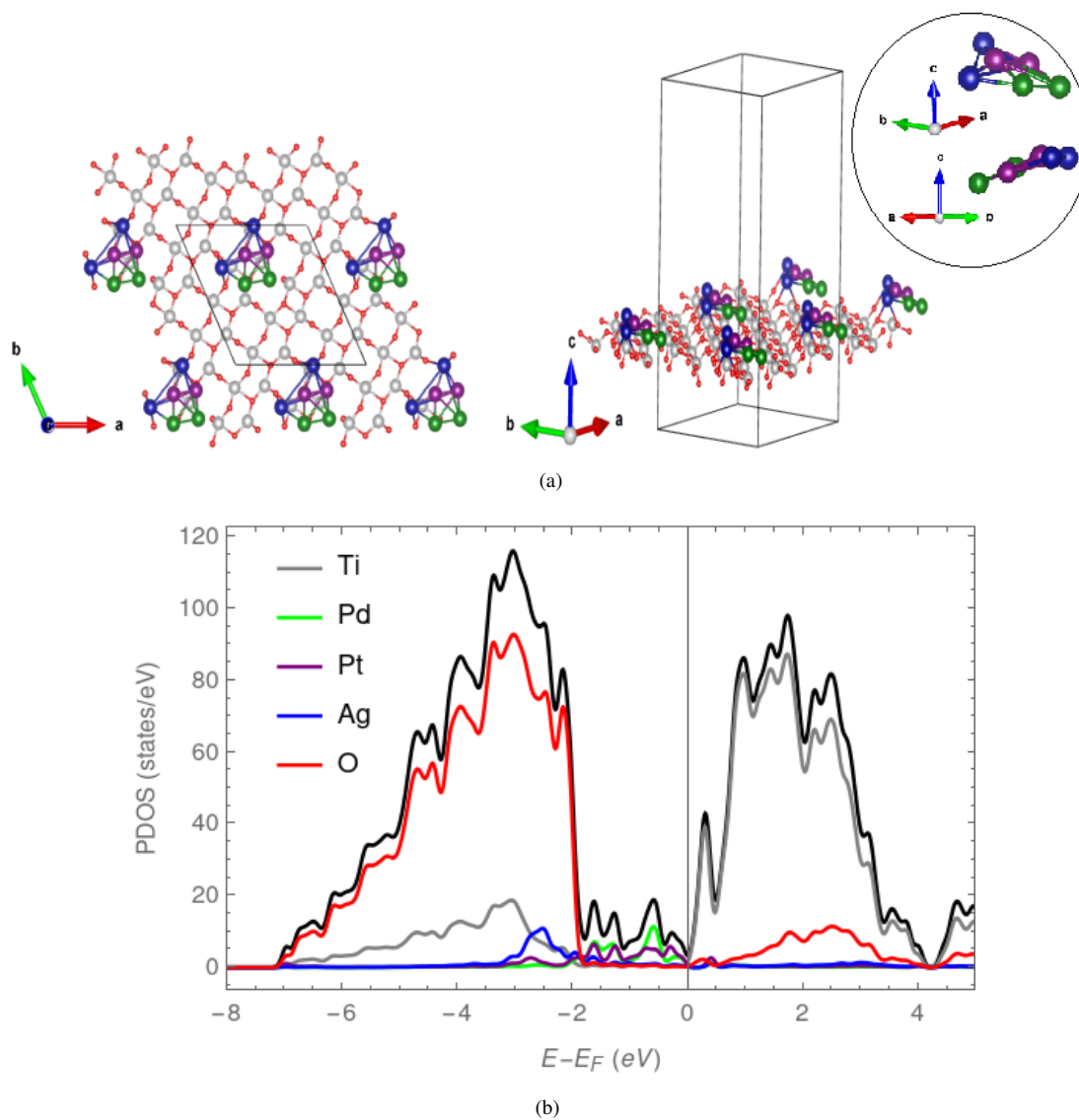


Figure 4.18: (a) Top view of the outermost layer and side view of the optimized geometry. (b) Partial Density of States (PDOS) of trimetallic $Pd_2Pt_2Ag_2$ cluster supported on oxygen defective $A-TiO_2(101)-c(4 \times 2)$.

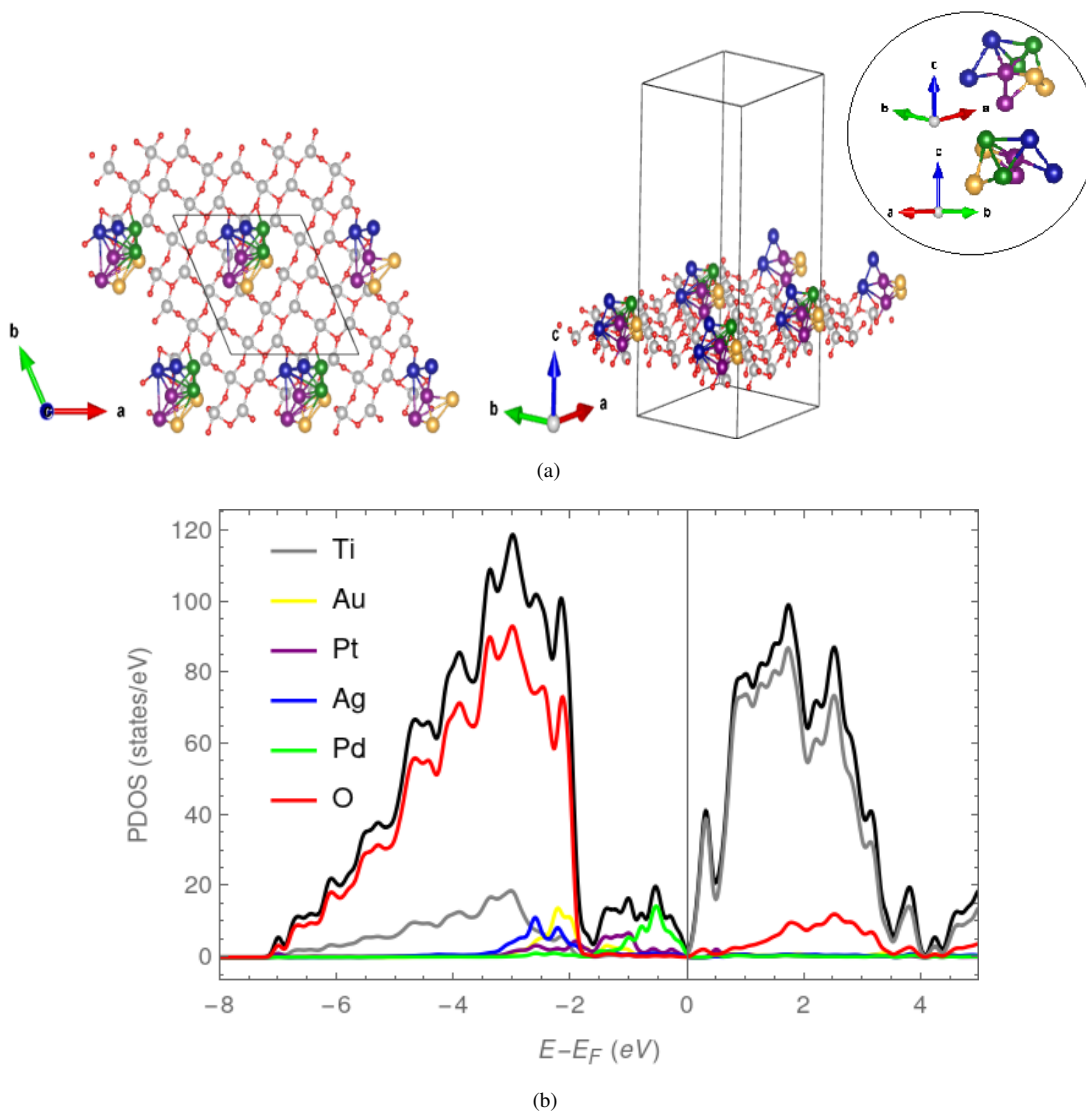


Figure 4.19: (a) Top view of the outermost layer and side view of the optimized geometry. (b) Partial Density of States (PDOS) of tetra metallic $Au_2Pt_2Ag_2Pd_2$ cluster supported on oxygen defective $A-TiO_2(101)-c(4 \times 2)$.

The order of adsorption energy for the multicomponent clusters considering an oxygen defective surface, from highest to lowest is: $Au_2Pt_2Ag_2Pd_2$ ($\Delta E_{Ads} = 15.79$ eV) > Pd_4Ag_4 ($\Delta E_{Ads} = 14.39$ eV) > $Au_2Ag_2Pd_2$ ($\Delta E_{Ads} = 10.89$ eV) > $Pd_2Pt_2Ag_2$ ($\Delta E_{Ads} = 10.28$ eV) > Pt_4Pd_4 ($\Delta E_{Ads} = 7.30$ eV).

The highest adsorption energy for the tested multicomponent clusters is lower than that of the single metal clusters. Specifically, the Ag_8 cluster exhibits stronger interaction with the surface compared to the $Au_2Pt_2Ag_2Pd_2$

tetrametallic cluster, despite the presence of Ag atoms in both clusters. This also suggests that multi-metal clusters can reach high adsorption energies but do not always overcome the strongest single-metal (Ag-Ag) interactions. Moreover, as in the case of the Pd_4Ag_4 bimetallic cluster, it is observed that the combination of metals in some cases can almost equal but not significantly exceed the adsorption energy of the single-metal counterparts (Pd- $\Delta E_{Ads} = 14.84$ eV, and Ag- $\Delta E_{Ads} = 16.54$ eV). Clusters such as $Au_2Ag_2Pd_2$ and $Pd_2Pt_2Ag_2$ resulted in lower values of adsorption energies compared to their single-metal counterparts, except for the inclusion of Pt. Both trimetallic clusters display similar values, with only a 0.61 eV difference when substituting Pt with Au. This may be due to the strong Ag and Au interactions in both scenarios. If the individual metal clusters are compared, the energy difference is much larger, with Au_8 having the highest adsorption energy, 8.34 eV, higher than that of Pt_8 .

Table 4.2: Energetic properties for cluster@A- $TiO_2(101)-c(4 \times 2)$ systems computed with DFTB xBT Hamiltonian.

System Label	Fermi level (eV)	Total Energy of the system (eV)	ΔE_{Ads} Adsorption energy on surface (eV)	ΔE_{Coh} Average Cohesion energy per atom (eV)
TiO_2	-10.61	-14130.77	-	-
TiO_2+V_{O-sur}	-10.37	-14002.11	-	-
TiO_2+Au_8	-10.26	-15009.41	12.53	-29.23
TiO_2+Ag_8	-9.1	-14981.55	15.29	-31.53
TiO_2+Pd_8	-9.39	-15111.35	13.49	-21.24
TiO_2+Pt_8	-10.13	-15114.06	3.93	-58.33
$TiO_2+Au_8+V_{O-sur}$	-9.83	-14882.62	14.40	-31.10
$TiO_2+Ag_8+V_{O-sur}$	-8.92	-14854.14	16.54	-32.78
$TiO_2+Pd_8+V_{O-sur}$	-9.46	-14984.04	14.84	-22.59
$TiO_2+Pt_8+V_{O-sur}$	-10.1	-14987.53	6.06	-60.46
$TiO_2+Pd_4Ag_4+V_{O-sur}$	-9.24	-14919.63	14.39	-28.22
$TiO_2+Pt_4Pd_4+V_{O-sur}$	-9.73	-14984.57	7.30	-40.31
$TiO_2+Au_2Ag_2Pd_2+V_{O-sur}$	-9.67	-14679.54	10.89	-20.43
$TiO_2+Pd_2Pt_2Ag_2+V_{O-sur}$	-9.65	-14706.93	10.28	-28.93
$TiO_2+Au_2Pt_2Ag_2Pd_2+V_{O-sur}$	-9.67	-14925.16	15.79	-34.81

The contrast shows that multicomponent clusters are more complex than the sum of the contributions of each single metal. It demonstrates that combining metals can result in adsorption energies that are not additive but synergistic. In some cases, the presence of Pt apparently decreases the adsorption energy. Table 4.2 summarizes some relevant parameters of the systems calculated with DFTB. It shows that the energetically most stable system was loaded with the Pt_8 cluster. As for the adsorption energy, single metal cluster systems with an oxygen vacancy showed increased adsorption energy. In a general trend, we can order the systems according to their adsorption

energy as follows: single-metallic+oxygen vacancy> tetrametallic> single-metallic> trimetallic> bimetallic.

It also provides information on how the different nature of the clusters causes the Fermi level to shift. Introducing an oxygen vacancy raises the position of the Fermi level (rightward shift). The presence of a single metal cluster shows a similar trend, shifting it also to a higher value, with the Ag_8 cluster being the system showing the most significant increase and the Pt_8 cluster the smallest. In the case of multicomponent clusters, the Pd_4Ag_4 bimetallic system shows a larger shift of the Fermi level, even larger than some single metal clusters (Au, Pd, Pt); here, we can also observe the synergistic effects of metals, since for this particular example, the Fermi level is larger than that of Pd alone but smaller than that of Ag alone. Since the Fermi level plays a key role in determining electron occupancy, these shifts need to be considered; a higher Fermi level could mean improved conductivity and charge carrier mobility. Thus, the Ag_8 cluster could show an increase in the reactivity of the overall system, potentially being a good candidate not only for catalyzing pollutant degradation reactions but also for stabilizing reaction intermediates due to its adsorption properties.

4.3 DFT simulations

4.3.1 SCAN functional-based calculations

The PDOS for bare $A-TiO_2(101)-c(4 \times 2)$ is shown in Fig. 4.20. This surface resulted in a band gap of 3.17 eV, with the conduction band edge at 2.88 eV. For the Au_8 system supported on defective oxygen $A-TiO_2(101)$ (Fig. 4.21), the shortest distance of the Au atom to surface oxygen is $d_{Au-O} = 2.09 \text{ \AA}$, resulting in a value shorter than that obtained with the relaxation performed by DFTB. The metal-metal shortest bond is $d_{Au-Au} = 2.50 \text{ \AA}$, while the longest distance between Au-Au atoms is $d_{Au-Au} = 6.45 \text{ \AA}$. The metal-Ti shortest bond is $d_{Au-Ti} = 2.50 \text{ \AA}$. Considering the new electronic states within the band gap, the Au_8 cluster showed a band gap of 1.08 eV with a semiconductor behavior. The contribution to the valence band edge is mainly given by Au 5d states, the closest localized state to the Fermi level is located at -0.33 eV, and the conduction band edge is at 0.74 eV. The computed vacuum potential is shown in Fig. 4.22, resulting in 4.76 eV. The horizontal line represents the Fermi level of the system. The work function was calculated using the planar average electrostatic potential shown in Fig. 4.22, as explained in the methodology. In this plot, the highest value in where the potential becomes nearly constant (in the region from 15 \AA to 25 \AA), represents the vacuum level. The initial oscillations, from 0 to 15 \AA , are probably due to surface effects and interactions between the metallic atoms and the anatase surface. Regions of positive potential represent areas with low electron density like vacuum or inter-layer regions, whereas negative troughs might correspond to areas with higher electron density. The gray horizontal line indicates the Fermi level. On the other hand, for the $Au_2Pt_2Ag_2Pd_2$ tetrametallic cluster (Fig. 4.23), the shortest metal-O bond distances are $d_{Au-O} = 3.17 \text{ \AA}$, $d_{Pt-O} = 2.05 \text{ \AA}$, $d_{Ag-O} = 2.22 \text{ \AA}$ and $d_{Pd-O} = 2.05 \text{ \AA}$. The Au atom is preferentially located near the oxygen vacancy. This system exhibits a metallic nature with localized states at the Fermi level. The major contribution to the defect state at the Fermi level is given by gold, followed by palladium, silver, and platinum, respectively. The vacuum potential yielded 4.45 eV.

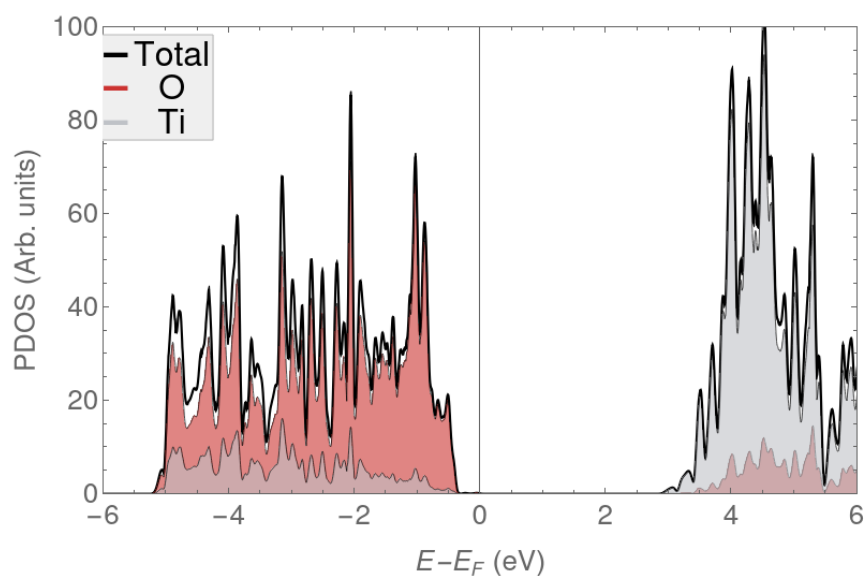


Figure 4.20: Partial Density of States (PDOS) of $A\text{-TiO}_2(101)\text{-}c(4 \times 2)$ computed with SCAN+rVV10+U.

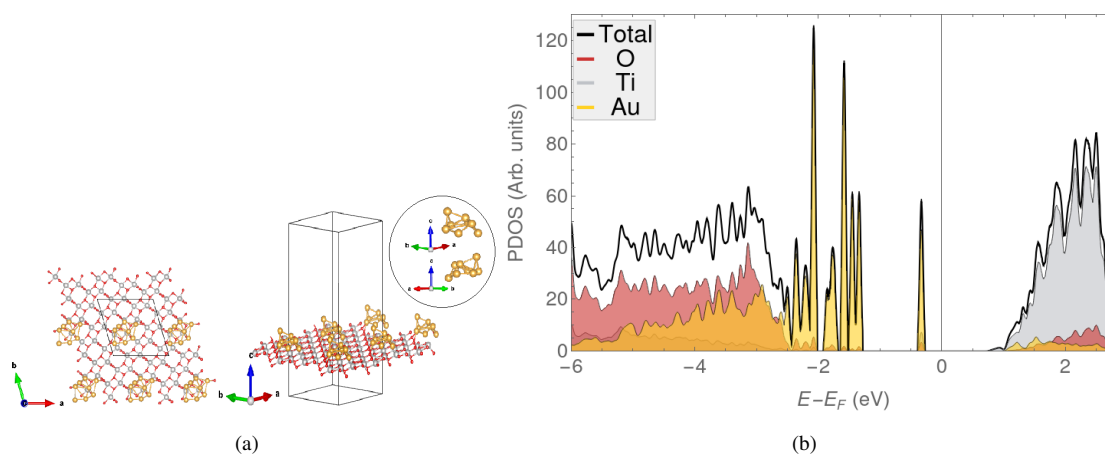


Figure 4.21: (a) Top view of the outermost layer and side view of the optimized geometry. (b) Partial Density of States (PDOS) of Au_8 cluster supported on oxygen defective $A\text{-TiO}_2(101)\text{-}c(4 \times 2)$ computed with SCAN+rVV10+U.

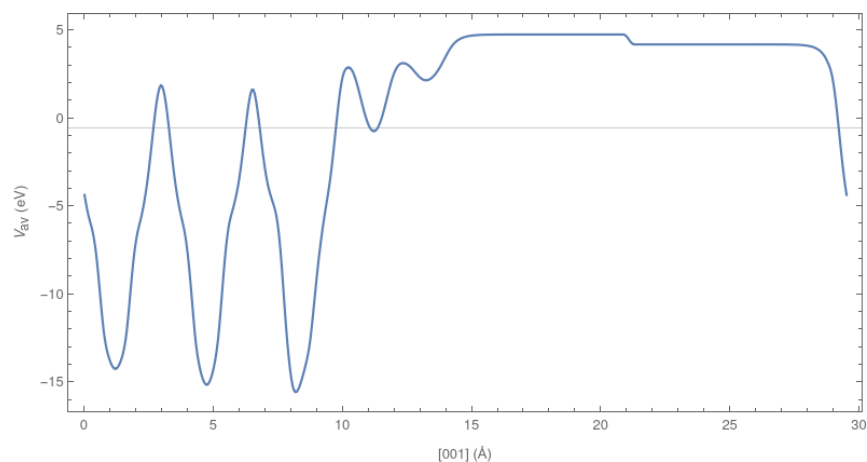


Figure 4.22: Planar average potential plot derived from the local potential of the $Au_8@A-TiO_2(101)-c(4 \times 2)+V_{O-sur}$ system calculated using SCAN+rVV10+U functional.

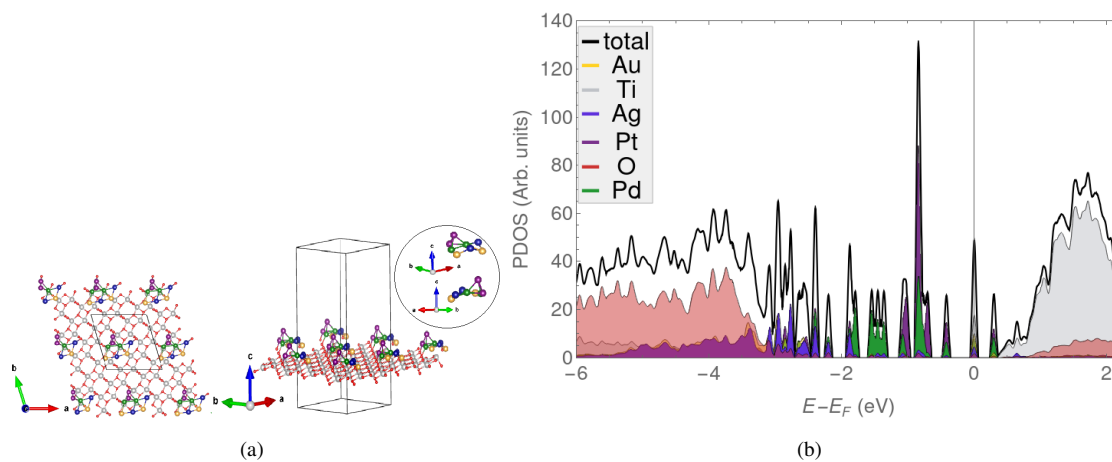


Figure 4.23: (a) Top view of the outermost layer and side view of the optimized geometry. (b) Partial Density of States (PDOS) of tetrametallic $Au_2Pt_2Ag_2Pd_2$ cluster supported on oxygen defective $A-TiO_2(101)-c(4 \times 2)$ computed with SCAN+rVV10+U.

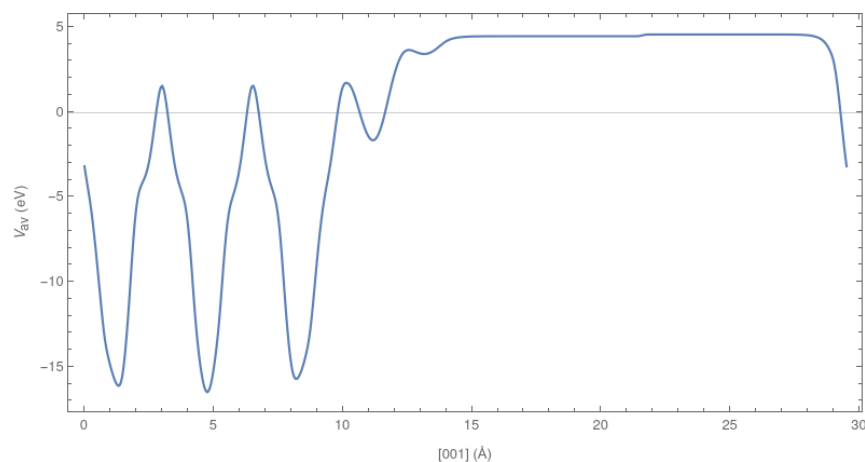


Figure 4.24: Planar average potential plot derived from the local potential of the $Au_2Pt_2Ag_2Pd_2@A-TiO_2(101)-c(4 \times 2)+V_{O-sur}$ system calculated using SCAN+rVV10+U functional.

4.3.2 r^2 SCAN functional-based calculations

The PDOS for bare $A-TiO_2(101)-c(4 \times 2)$ is shown in Fig. 4.25. This surface resulted in a band gap of 3.23 eV, with the conduction band edge at 3.29 eV.

The Pd_{11} cluster (Fig. 4.26) adopted the morphology of a truncated pyramid. The shortest distance of the Pd atom to surface oxygen is $d_{Pd-O} = 2.05 \text{ \AA}$, resulting in a value shorter than that of Pd_8 cluster obtained with DFTB. The metal-metal shortest bond is $d_{Pd-Pd} = 2.52 \text{ \AA}$, while the longest distance between Pd-Pd atoms is $d_{Pd-Pd} = 5.39 \text{ \AA}$. The metal-Ti shortest bond is $d_{Pd-Ti} = 2.33 \text{ \AA}$. The Pd_{11} cluster supported on oxygen-defective anatase gave rise to a narrow band gap of 0.34 eV. The conduction band edge is at 0.17 eV, and the closest localized state near the Fermi level is at -0.11 eV.

The bimetallic Au_3Pd_3 cluster (Fig. 4.28) shows a configuration in which the atoms are arranged in a "core-shell type", with the gold atoms covering the palladium atoms. The shortest metal-O bond distances are $d_{Au-O} = 2.08 \text{ \AA}$ and $d_{Pd-O} = 2.04 \text{ \AA}$. The metal-metal shortest bond are $d_{Pd-Au} = 2.55 \text{ \AA}$, $d_{Au-Au} = 2.53 \text{ \AA}$, and $d_{Pd-Pd} = 2.57 \text{ \AA}$. The Pd atom is preferentially located near the oxygen vacancy. It resulted in a band gap of 0.59 eV. The major contribution to the defect state near the fermi level is given by Au orbitals, followed by Pd orbitals. Near the conduction band edge, there is a higher contribution from palladium, while in the valence region there is a higher contribution from gold. The bottom of the conduction part is shifted at least $\sim 0.3 \text{ eV}$ in comparison to that of the Pd_{11} cluster.

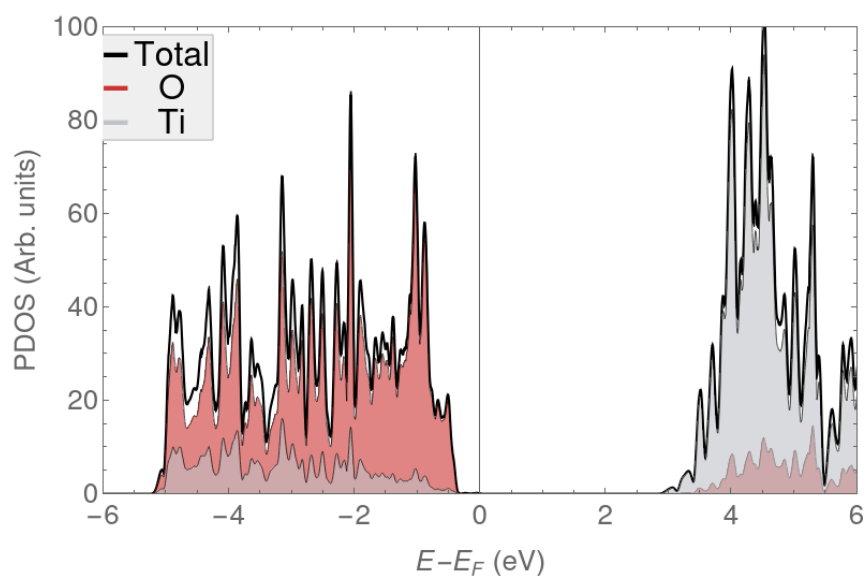


Figure 4.25: Partial Density of States (PDOS) of $A\text{-TiO}_2(101)\text{-}c(4 \times 2)$ computed with $r^2\text{SCAN+rVV10+U}$.

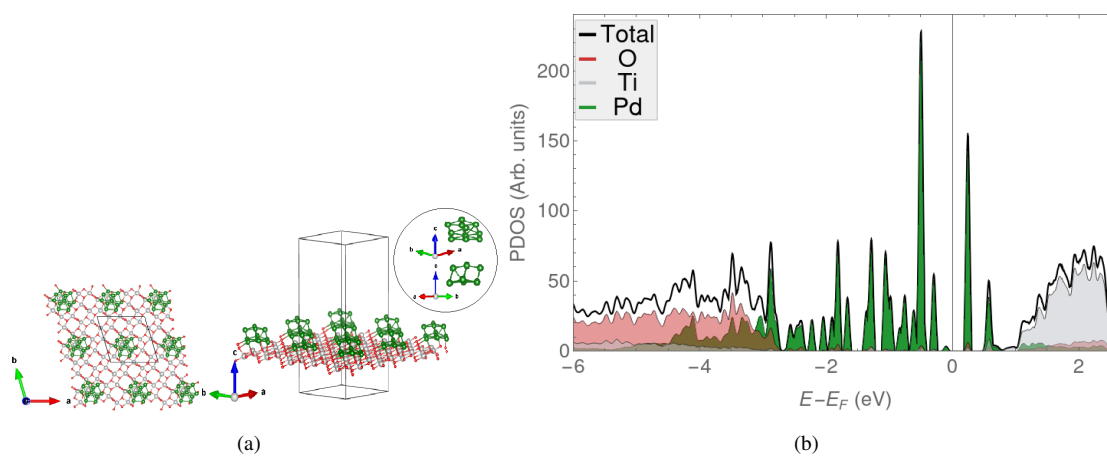


Figure 4.26: (a) Top view of the outermost layer and side view of the optimized geometry. (b) Partial Density of States (PDOS) of Pd_{11} cluster supported on oxygen defective $A\text{-TiO}_2(101)\text{-}c(4 \times 2)$ computed with $r^2\text{SCAN+rVV10+U}$.

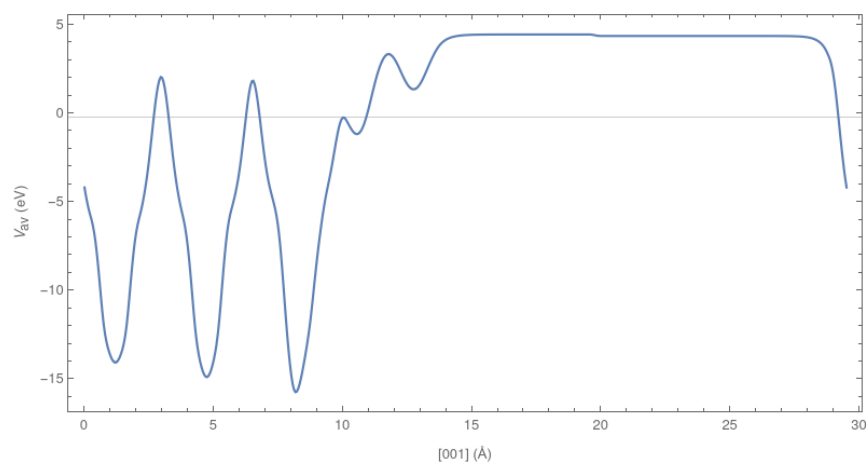


Figure 4.27: Planar average potential plot derived from the local potential of the $Pd_{11}@A-TiO_2(101)-c(4\times 2)+V_{O-sur}$ system calculated using $r^2SCAN+rVV10+U$ functional.

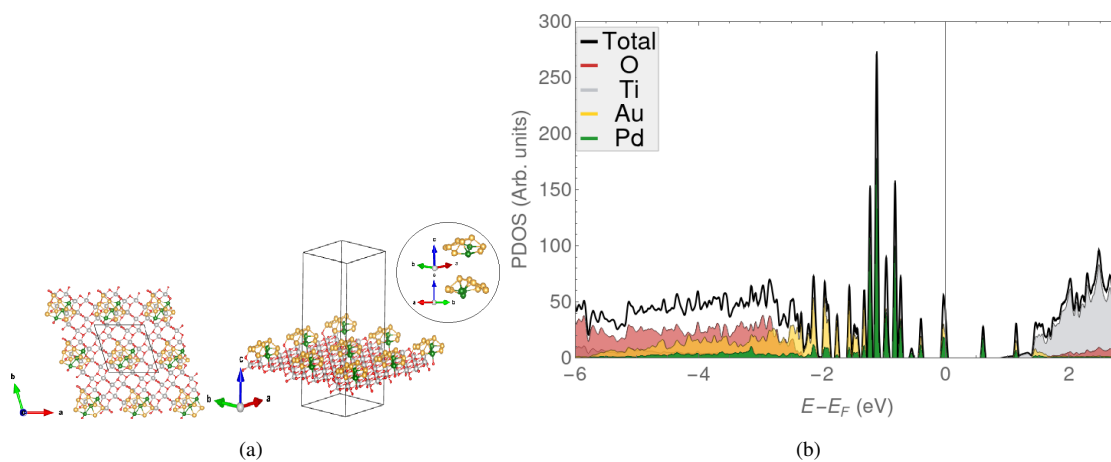


Figure 4.28: (a) Top view of the outermost layer and side view of the optimized geometry. (b) Partial Density of States (PDOS) of Au_8Pd_3 cluster supported on oxygen defective $A-TiO_2(101)-c(4\times 2)$ computed with $r^2SCAN+rVV10+U$.

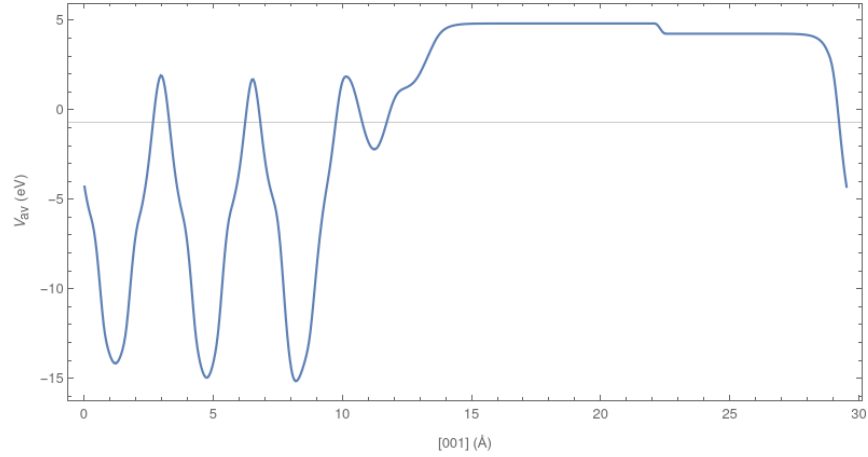


Figure 4.29: Planar average potential plot derived from the local potential of the $Au_8Pd_3@A-TiO_2(101)-c(4 \times 2)+V_{O-sur}$ system calculated using $r^2SCAN+rVV10+U$ functional.

The results of the electronic properties are summarized in Table 4.3. The Au_8Pd_3 bimetallic cluster system achieved the highest work function. In comparison, the lowest work function was obtained with the $Au_2Pt_2Ag_2Pd_2$ tetrametallic cluster system, with a difference of almost 1 eV between them. As for the band gap, the descending order is (from semiconductor to metallic behavior): $Au_8 > Au_8Pd_3 > Pd_{11} > Au_2Pt_2Ag_2Pd_2$.

Table 4.3: Energetic properties for cluster@A- $TiO_2(101)-c(4 \times 2)$ systems computed with DFT SCAN/ $r^2SCAN+rVV10+U$ functionals.

System Label	Fermi Level (eV)	Vacuum Potential (eV)	Work Function (eV)	Band Gap (eV)
$Au_8+TiO_2+V_{O-sur}$	-0.55	4.76	5.31	1.08
$Au_2Pt_2Ag_2Pd_2+TiO_2+V_{O-sur}$	-0.09	4.45	4.54	metallic
$Pd_{11}+TiO_2+V_{O-sur}$	-0.24	4.45	4.70	0.34
$Au_8Pd_3+TiO_2+V_{O-sur}$	-0.7	4.85	5.55	0.59

Chapter 5

Conclusions & Outlook

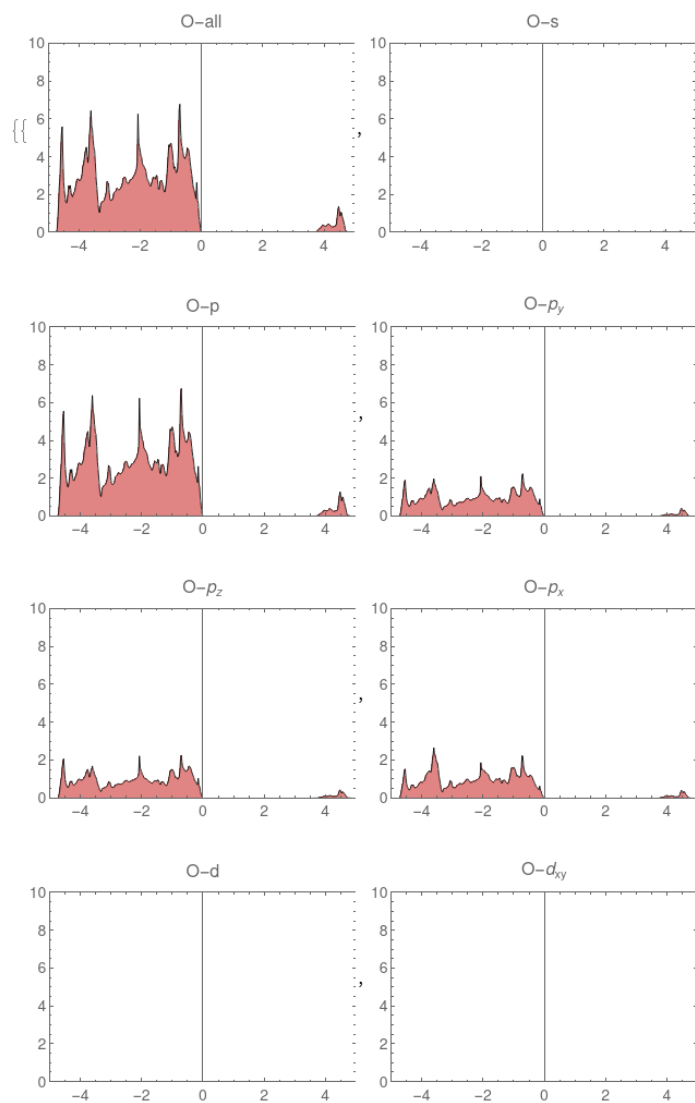
Using a computational approach, this thesis has studied the interactions of multicomponent nanoclusters of noble metals (Au, Ag, Pt, and Pd) supported on the surface of anatase TiO₂ (101). This work proposed a methodology to explore new TiO₂-based nanomaterials before the experimental phase. Studying the energetics of potential materials is key for a systematic design; therefore, using computational modeling tools can be consolidated as a great advantage. Most of the proposed systems turned out to be metallic or with a narrow band gap, except for the Au₈ gold cluster with oxygen vacancy on the anatase surface calculated with SCAN, which resulted in a band gap of 1.08 eV. As for the approaches considered, the functional with the most advantages is *r*²SCAN. The computation time was reduced to a minimum, and the results were comparable to those of SCANs. However, DFTB+ is a great alternative for structural relaxations that could be combined with the electronic structure calculation provided by DFT for better results. The implementation of Hubbard correction improved the accuracy of calculations regarding experimentally available data. It was found that a suitable U correction for SCAN was 5.3 eV, while for *r*²SCAN was 5.15 eV.

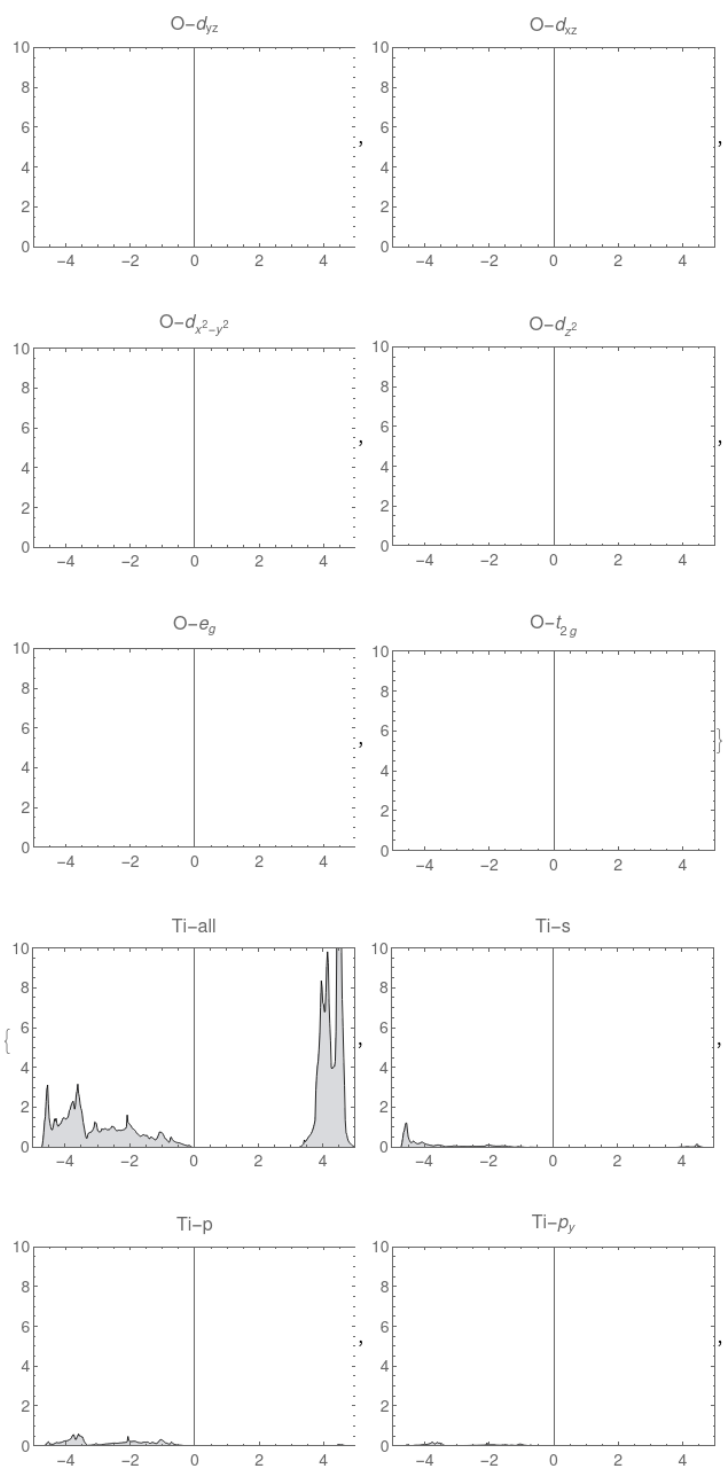
As previously mentioned, individual metal clusters with non-defective anatase configurations yielded lower energy than those of cluster systems supported on oxygen-defective anatase, which might suggest higher thermodynamic stability. According to the available literature, the oxygen vacancy site was expected to act as a cluster nucleation zone. The systems with the highest adsorption energy were those supported on oxygen-defective anatase. Specifically, the Ag₈ cluster system had the highest adsorption energy, $\Delta E_{Ads} = 16.54$ eV, followed by the Au₂Pt₂Ag₂Pd₂ tetrametallic cluster system, with $\Delta E_{Ads} = 15.79$ eV. These systems could be suitable for catalysis applications, as they are more likely to improve reaction rates and facilitate the binding of reactants close to the activation sites. Pd and Au atoms show a pattern of preference for occupying positions associated with the oxygen vacancy in most systems studied.

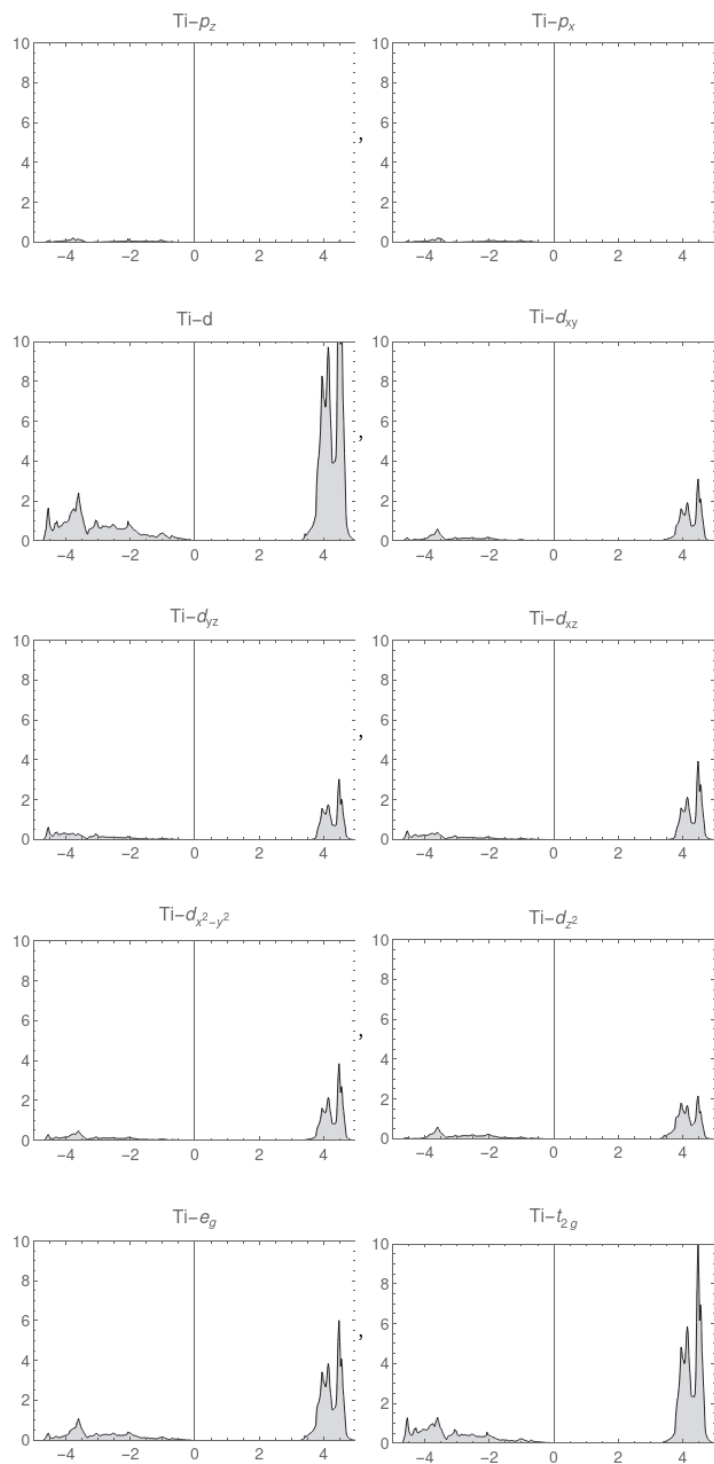
These preliminary results represent the first screening of various combinations of TiO₂-based materials. They provide insight into the intricate relationships between the various noble metals and anatase surfaces and lay the groundwork for further investigation of a wider range of configurations.

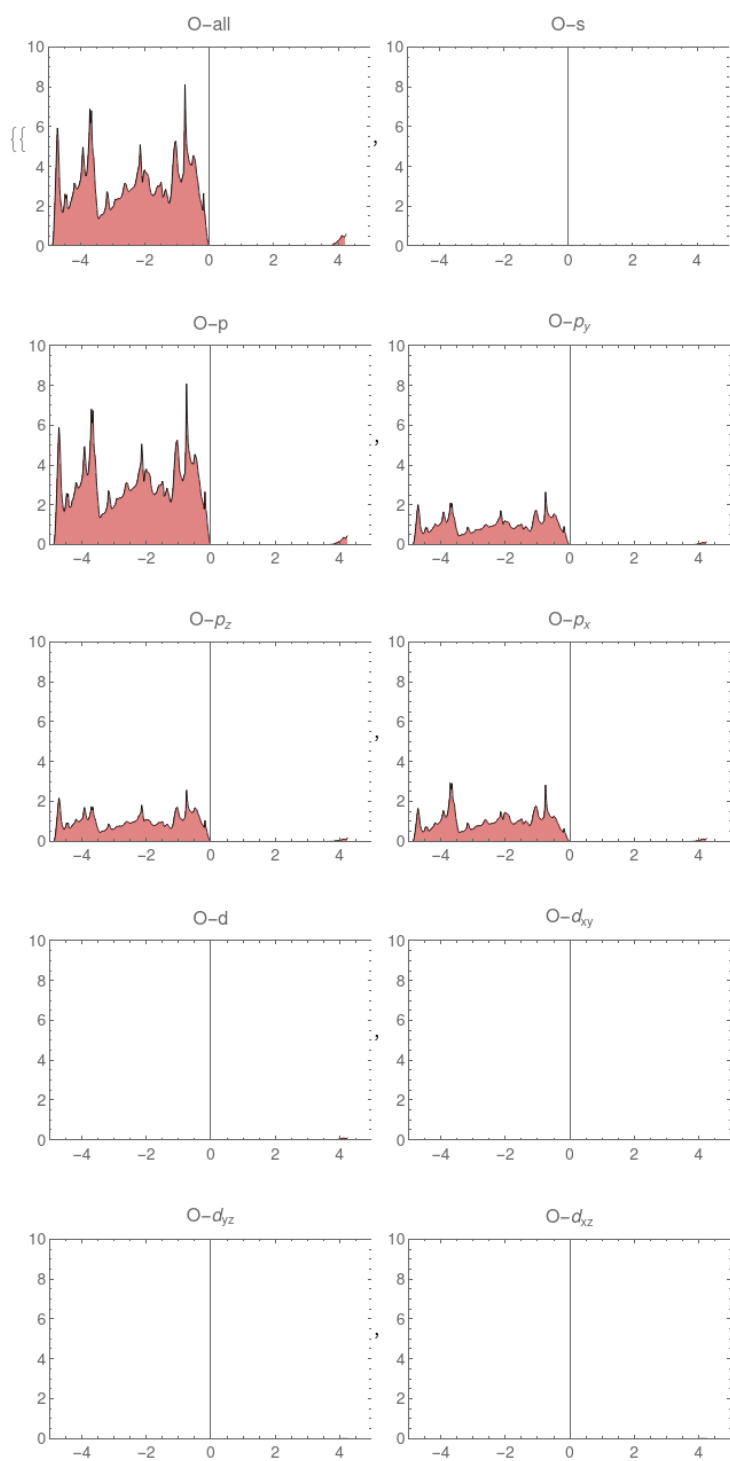
Appendix A

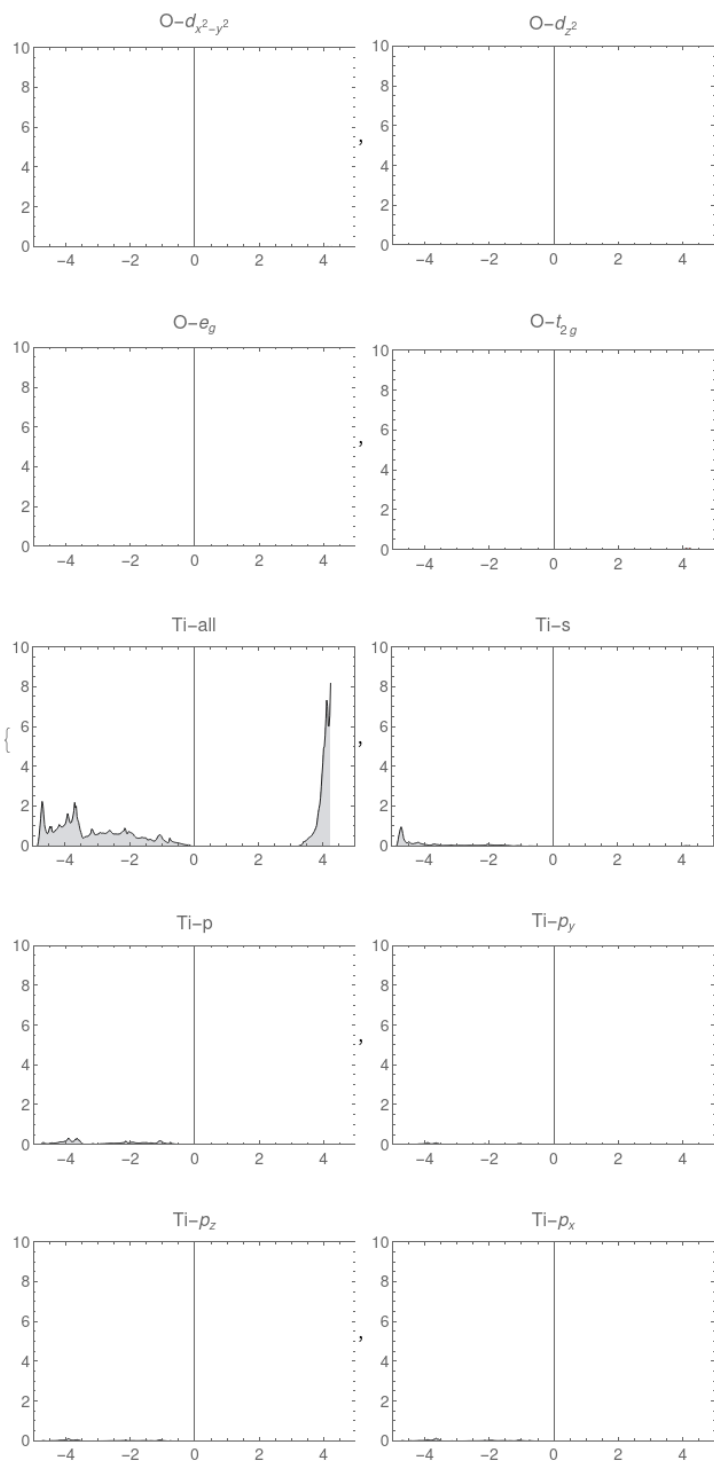
Detailed Orbital-resolved Partial Density of States





Figure A.1: Detailed orbital resolved PDOS for Bulk Anatase TiO_2 computed with r^2 SCAN+rVV10+U functional.





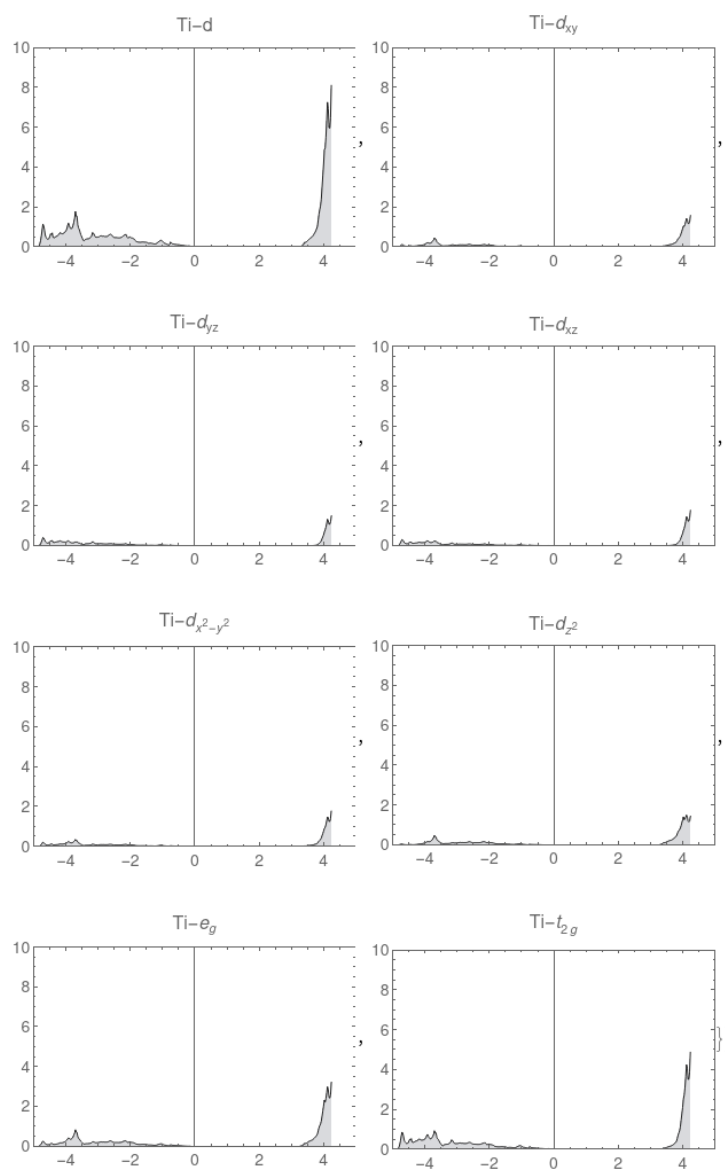


Figure A.2: Detailed orbital resolved PDOS for Bulk Anatase TiO_2 computed with SCAN+rVV10+U functional.

Bibliography

- [1] Sholl, D. S.; Steckel, J. A. *Density functional theory: a practical introduction*; John Wiley & Sons, 2022.
- [2] Momma, K.; Izumi, F. VESTA: a three-dimensional visualization system for electronic and structural analysis. *Journal of Applied crystallography* **2008**, *41*, 653–658.
- [3] Kavan, L.; Grätzel, M.; Gilbert, S.; Klemenč, C.; Scheel, H. Electrochemical and photoelectrochemical investigation of single-crystal anatase. *Journal of the American Chemical Society* **1996**, *118*, 6716–6723.
- [4] Perdew, J. P.; Ruzsinszky, A.; Tao, J.; Staroverov, V. N.; Scuseria, G. E.; Csonka, G. I. Prescription for the design and selection of density functional approximations: More constraint satisfaction with fewer fits. *The Journal of chemical physics* **2005**, *123*.
- [5] Palafox, M. A. DFT computations on vibrational spectra: Scaling procedures to improve the wavenumbers. *Physical Sciences Reviews* **2018**, *3*, 20170184.
- [6] Sun, J.; Ruzsinszky, A.; Perdew, J. P. Strongly constrained and appropriately normed semilocal density functional. *Physical review letters* **2015**, *115*, 036402.
- [7] Arun, J.; Nachiappan, S.; Rangarajan, G.; Alagappan, R. P.; Gopinath, K.; Lichtfouse, E. Synthesis and application of titanium dioxide photocatalysis for energy, decontamination and viral disinfection: A review. *Environmental Chemistry Letters* **2023**, *21*, 339–362.
- [8] Gogoi, D.; Namdeo, A.; Golder, A. K.; Peela, N. R. Ag-doped TiO₂ photocatalysts with effective charge transfer for highly efficient hydrogen production through water splitting. *International Journal of Hydrogen Energy* **2020**, *45*, 2729–2744.
- [9] Moradi, M.; Khorasheh, F.; Larimi, A. Pt nanoparticles decorated Bi-doped TiO₂ as an efficient photocatalyst for CO₂ photo-reduction into CH₄. *Solar Energy* **2020**, *211*, 100–110.
- [10] Nguyen, T. L.; Pham, T. H.; Viet, N. M.; Thang, P. Q.; Rajagopal, R.; Sathya, R.; Jung, S. H.; Kim, T. Improved photodegradation of antibiotics pollutants in wastewaters by advanced oxidation process based on Ni-doped TiO₂. *Chemosphere* **2022**, *302*, 134837.

- [11] David, T. M.; Gnanasekar, K.; Wilson, P.; Sagayaraj, P.; Mathews, T. Effect of Ni, Pd, and Pt nanoparticle dispersion on thick films of TiO₂ nanotubes for hydrogen sensing: TEM and XPS studies. *ACS omega* **2020**, *5*, 11352–11360.
- [12] Zhang, Y.-Q.; Ma, D.-K.; Zhang, Y.-G.; Chen, W.; Huang, S.-M. N-doped carbon quantum dots for TiO₂-based photocatalysts and dye-sensitized solar cells. *Nano Energy* **2013**, *2*, 545–552.
- [13] Liu, L.; Zhao, H.; Andino, J. M.; Li, Y. Photocatalytic CO₂ reduction with H₂O on TiO₂ nanocrystals: Comparison of anatase, rutile, and brookite polymorphs and exploration of surface chemistry. *Acs Catalysis* **2012**, *2*, 1817–1828.
- [14] De Angelis, F.; Di Valentin, C.; Fantacci, S.; Vittadini, A.; Selloni, A. Theoretical studies on anatase and less common TiO₂ phases: bulk, surfaces, and nanomaterials. *Chemical reviews* **2014**, *114*, 9708–9753.
- [15] Mohamad, M.; Haq, B. U.; Ahmed, R.; Shaari, A.; Ali, N.; Hussain, R. A density functional study of structural, electronic and optical properties of titanium dioxide: Characterization of rutile, anatase and brookite polymorphs. *Materials Science in Semiconductor Processing* **2015**, *31*, 405–414.
- [16] Yamakata, A.; Vequizo, J. J. M. Curious behaviors of photogenerated electrons and holes at the defects on anatase, rutile, and brookite TiO₂ powders: A review. *Journal of Photochemistry and Photobiology C: Photochemistry Reviews* **2019**, *40*, 234–243.
- [17] Zhang, J.; Zhou, P.; Liu, J.; Yu, J. New understanding of the difference of photocatalytic activity among anatase, rutile and brookite TiO₂. *Physical Chemistry Chemical Physics* **2014**, *16*, 20382–20386.
- [18] Luttrell, T.; Halpegamage, S.; Tao, J.; Kramer, A.; Sutter, E.; Batzill, M. Why is anatase a better photocatalyst than rutile?—Model studies on epitaxial TiO₂ films. *Scientific reports* **2014**, *4*, 4043.
- [19] Tran, H. T. T.; Kosslick, H.; Ibad, M. F.; Fischer, C.; Bentrup, U.; Vuong, T. H.; Nguyen, L. Q.; Schulz, A. Photocatalytic performance of highly active brookite in the degradation of hazardous organic compounds compared to anatase and rutile. *Applied Catalysis B: Environmental* **2017**, *200*, 647–658.
- [20] Lazzeri, M.; Vittadini, A.; Selloni, A. Structure and energetics of stoichiometric TiO₂ anatase surfaces. *Physical Review B* **2001**, *63*, 155409.
- [21] Chen, W.; Kuang, Q.; Wang, Q.; Xie, Z. Engineering a high energy surface of anatase TiO₂ crystals towards enhanced performance for energy conversion and environmental applications. *Rsc Advances* **2015**, *5*, 20396–20409.
- [22] Ye, L.; Mao, J.; Peng, T.; Zan, L.; Zhang, Y. Opposite photocatalytic activity orders of low-index facets of anatase TiO₂ for liquid phase dye degradation and gaseous phase CO₂ photoreduction. *Physical Chemistry Chemical Physics* **2014**, *16*, 15675–15680.

- [23] Wen, J.; Li, X.; Liu, W.; Fang, Y.; Xie, J.; Xu, Y. Photocatalysis fundamentals and surface modification of TiO₂ nanomaterials. *Chinese Journal of Catalysis* **2015**, *36*, 2049–2070.
- [24] Mazierski, P.; Mikolajczyk, A.; Grzyb, T.; Caicedo, P. N. A.; Wei, Z.; Kowalska, E.; Pinto, H. P.; Zaleska-Medynska, A.; Nadolna, J. On the excitation mechanism of visible responsible Er-TiO₂ system proved by experimental and theoretical investigations for boosting photocatalytic activity. *Applied Surface Science* **2020**, *527*, 146815.
- [25] Barkul, R. P.; Patil, M. K.; Patil, S. M.; Shevale, V. B.; Delekar, S. D. Sunlight-assisted photocatalytic degradation of textile effluent and Rhodamine B by using iodine doped TiO₂ nanoparticles. *Journal of Photochemistry and Photobiology A: Chemistry* **2017**, *349*, 138–147.
- [26] others,, *et al.* TiO₂ and NaTaO₃ decorated by trimetallic Au/Pd/Pt core-shell nanoparticles as efficient photocatalysts: experimental and computational studies. *ACS Sustainable Chemistry & Engineering* **2018**, *6*, 16665–16682.
- [27] Zhang, J.; Zhang, L.; Shi, Y.; Xu, G.; Zhang, E.; Wang, H.; Kong, Z.; Xi, J.; Ji, Z. Anatase TiO₂ nanosheets with coexposed {101} and {001} facets coupled with ultrathin SnS₂ nanosheets as a face-to-face npn dual heterojunction photocatalyst for enhancing photocatalytic activity. *Applied Surface Science* **2017**, *420*, 839–848.
- [28] Goulart, S.; Nieves, L. J. J.; Dal Bó, A. G.; Bernardin, A. M. Sensitization of TiO₂ nanoparticles with natural dyes extracts for photocatalytic activity under visible light. *Dyes and Pigments* **2020**, *182*, 108654.
- [29] Qiu, H.; Ma, X.; Sun, C.; Zhao, B.; Chen, F. Surface oxygen vacancies enriched Pt/TiO₂ synthesized with a defect migration strategy for superior photocatalytic activity. *Applied Surface Science* **2020**, *506*, 145021.
- [30] Mikolajczyk, A.; Malankowska, A.; Nowaczyk, G.; Gajewicz, A.; Hirano, S.; Jurga, S.; Zaleska-Medynska, A.; Puzyn, T. Combined experimental and computational approach to developing efficient photocatalysts based on Au/Pd–TiO₂ nanoparticles. *Environmental Science: Nano* **2016**, *3*, 1425–1435.
- [31] Mikolajczyk, A.; Gajewicz, A.; Mulkiwicz, E.; Rasulev, B.; Marchelek, M.; Diak, M.; Hirano, S.; Zaleska-Medynska, A.; Puzyn, T. Nano-QSAR modeling for ecosafe design of heterogeneous TiO₂-based nano-photocatalysts. *Environmental Science: Nano* **2018**, *5*, 1150–1160.
- [32] Klein, M.; Nadolna, J.; Gołębiewska, A.; Mazierski, P.; Klimczuk, T.; Remita, H.; Zaleska-Medynska, A. The effect of metal cluster deposition route on structure and photocatalytic activity of mono- and bimetallic nanoparticles supported on TiO₂ by radiolytic method. *Applied Surface Science* **2016**, *378*, 37–48.
- [33] Malankowska, A.; Mikolajczyk, A.; Mędrzycka, J.; Wysocka, I.; Nowaczyk, G.; Jarek, M.; Puzyn, T.; Mulkiwicz, E. The effect of Ag, Au, Pt, and Pd on the surface properties, photocatalytic activity and toxicity of multicomponent TiO₂-based nanomaterials. *Environmental Science: Nano* **2020**, *7*, 3557–3574.

- [34] Lisovski, O.; Chesnokov, A.; Piskunov, S.; Bocharov, D.; Zhukovskii, Y. F.; Wessel, M.; Spohr, E. Ab initio calculations of doped TiO₂ anatase (101) nanotubes for photocatalytical water splitting applications. *Materials Science in Semiconductor Processing* **2016**, *42*, 138–141.
- [35] Mikolajczyk, A.; Falkowski, D. One Step before Synthesis: Structure–Property–Condition Relationship Models to Sustainable Design of Efficient TiO₂-Based Multicomponent Nanomaterials. *International Journal of Molecular Sciences* **2022**, *23*, 13196.
- [36] Hafner, J.; Wolverton, C.; Ceder, G. Toward computational materials design: the impact of density functional theory on materials research. *MRS bulletin* **2006**, *31*, 659–668.
- [37] Jones, R. O. Density functional theory: Its origins, rise to prominence, and future. *Reviews of modern physics* **2015**, *87*, 897.
- [38] Nasr, M.; Eid, C.; Habchi, R.; Miele, P.; Bechelany, M. Recent progress on titanium dioxide nanomaterials for photocatalytic applications. *ChemSusChem* **2018**, *11*, 3023–3047.
- [39] Moma, J.; Baloyi, J. Modified titanium dioxide for photocatalytic applications. *Photocatalysts-Applications and Attributes* **2019**, *18*, 10–5772.
- [40] Blakemore, J. S. *Solid state physics*; Cambridge university press, 1985.
- [41] Inkson, J. C. *Many-body theory of solids: an introduction*; Springer Science & Business Media, 2012.
- [42] Giustino, F. *Materials modelling using density functional theory: properties and predictions*; Oxford University Press, 2014.
- [43] Fulde, P.; Stoll, H. Dealing with the exponential wall in electronic structure calculations. *The Journal of Chemical Physics* **2017**, *146*.
- [44] Born, M. Born-oppenheimer approximation. *Ann. Phys* **1927**, *84*, 457–484.
- [45] Gross, A. Theoretical surface science. *A Microscopic Perspective. Originally published in the series: Advanced Texts in Physics*, **2003**, 132.
- [46] Scherrer, A.; Agostini, F.; Sebastiani, D.; Gross, E.; Vuilleumier, R. On the mass of atoms in molecules: Beyond the Born-Oppenheimer approximation. *Physical Review X* **2017**, *7*, 031035.
- [47] Sutcliffe, B. T.; Woolley, R. G. On the quantum theory of molecules. *The Journal of chemical physics* **2012**, *137*.
- [48] Tiesinga, E.; Mohr, P. J.; Newell, D. B.; Taylor, B. N. CODATA recommended values of the fundamental physical constants: 2018. *Journal of Physical and Chemical Reference Data* **2021**, *50*.
- [49] Hartree, D. R. The wave mechanics of an atom with a non-Coulomb central field. Part I. Theory and methods. 1928.

- [50] Sutcliffe, B. To what question is the clamped-nuclei electronic potential the answer? *Theoretical Chemistry Accounts* **2010**, *127*, 121–131.
- [51] Kantorovich, L. *Quantum theory of the solid state: an introduction*; Springer Science & Business Media, 2004; Vol. 136.
- [52] Hohenberg, P.; Kohn, W. Inhomogeneous electron gas. *Physical review* **1964**, *136*, B864.
- [53] Kohn, W.; Sham, L. J. Self-consistent equations including exchange and correlation effects. *Physical review* **1965**, *140*, A1133.
- [54] Lieb, E. H. Thomas-Fermi and related theories of atoms and molecules. *Reviews of Modern Physics* **1981**, *53*, 603.
- [55] Harbola, M. K.; Banerjee, A. Many-electron problem in terms of the density: From Thomas-Fermi to modern density-functional theory. *Journal of Theoretical and Computational Chemistry* **2003**, *2*, 301–322.
- [56] Brink, D. Density functional theory. *Nuclear Physics News* **2002**, *12*, 27–32.
- [57] Parr, R. G. Density functional theory. *Annual Review of Physical Chemistry* **1983**, *34*, 631–656.
- [58] Kutzelnigg, W. Density Functional Theory (DFT) and ab-initio Quantum. *Trends and Perspectives in Modern Computational Science* **2006**, *6*, 23.
- [59] Sun, J.; Furness, J. W.; Zhang, Y. *Mathematical Physics in Theoretical Chemistry*; Elsevier, 2019; pp 119–159.
- [60] Sahni, V.; Sahni, V. The hohenberg-kohn theorems and kohn-sham density functional theory. *Quantal Density Functional Theory* **2004**, 99–123.
- [61] Kvaal, S.; Helgaker, T. Ground-state densities from the Rayleigh-Ritz variation principle and from density-functional theory. *The Journal of Chemical Physics* **2015**, *143*.
- [62] Kümmel, S.; Kronik, L. Orbital-dependent density functionals: Theory and applications. *Reviews of Modern Physics* **2008**, *80*, 3.
- [63] Wasserman, A.; Nafziger, J.; Jiang, K.; Kim, M.-C.; Sim, E.; Burke, K. The importance of being inconsistent. *Annual review of physical chemistry* **2017**, *68*, 555–581.
- [64] Yu, H. S.; Li, S. L.; Truhlar, D. G. Perspective: Kohn-Sham density functional theory descending a staircase. *The Journal of chemical physics* **2016**, *145*.
- [65] Bhattacharyya, A.; Furnstahl, R. The kinetic energy density in Kohn-Sham density functional theory. *Nuclear Physics A* **2005**, *747*, 268–294.
- [66] Kohn, W.; Sham, L. Density functional theory. 1996.

- [67] Perdew, J. P. Climbing the ladder of density functional approximations. *MRS bulletin* **2013**, *38*, 743–750.
- [68] Kohn, W.; Becke, A. D.; Parr, R. G. Density functional theory of electronic structure. *The journal of physical chemistry* **1996**, *100*, 12974–12980.
- [69] Tsuneda, T. Exchange–Correlation Functionals. *Density Functional Theory in Quantum Chemistry* **2014**, 101–124.
- [70] Perdew, J. P.; Schmidt, K. Jacob’s ladder of density functional approximations for the exchange–correlation energy. 2001.
- [71] Zhang, I. Y.; Xu, X. On the top rung of Jacob’s ladder of density functional theory: Toward resolving the dilemma of SIE and NCE. *Wiley Interdisciplinary Reviews: Computational Molecular Science* **2021**, *11*, e1490.
- [72] Johansson, M. P.; Kaila, V. R.; Sundholm, D. Ab initio, density functional theory, and semi-empirical calculations. *Biomolecular Simulations: Methods and Protocols* **2013**, 3–27.
- [73] Dal Corso, A.; Pasquarello, A.; Baldereschi, A.; Car, R. Generalized-gradient approximations to density-functional theory: A comparative study for atoms and solids. *Physical Review B* **1996**, *53*, 1180.
- [74] Perdew, J. P.; Chevary, J. A.; Vosko, S. H.; Jackson, K. A.; Pederson, M. R.; Singh, D. J.; Fiolhais, C. Atoms, molecules, solids, and surfaces: Applications of the generalized gradient approximation for exchange and correlation. *Physical review B* **1992**, *46*, 6671.
- [75] Perdew, J. P.; Burke, K.; Ernzerhof, M. Generalized gradient approximation made simple. *Physical review letters* **1996**, *77*, 3865.
- [76] Perdew, J. P.; Kurth, S.; Zupan, A.; Blaha, P. Accurate density functional with correct formal properties: A step beyond the generalized gradient approximation. *Physical review letters* **1999**, *82*, 2544.
- [77] Yang, J. H.; Kitchaev, D. A.; Ceder, G. Rationalizing accurate structure prediction in the meta-GGA SCAN functional. *Physical Review B* **2019**, *100*, 035132.
- [78] Tran, F.; Baudesson, G.; Carrete, J.; Madsen, G. K.; Blaha, P.; Schwarz, K.; Singh, D. J. Shortcomings of meta-GGA functionals when describing magnetism. *Physical Review B* **2020**, *102*, 024407.
- [79] Sabatini, R.; Gorni, T.; De Gironcoli, S. Nonlocal van der Waals density functional made simple and efficient. *Physical Review B* **2013**, *87*, 041108.
- [80] Bartók, A. P.; Yates, J. R. Regularized SCAN functional. *The Journal of chemical physics* **2019**, *150*, 161101.
- [81] Furness, J. W.; Kaplan, A. D.; Ning, J.; Perdew, J. P.; Sun, J. Accurate and numerically efficient r2SCAN meta-generalized gradient approximation. *The journal of physical chemistry letters* **2020**, *11*, 8208–8215.

- [82] Becke, A. D. A new mixing of Hartree–Fock and local density-functional theories. *The Journal of chemical physics* **1993**, *98*, 1372–1377.
- [83] Becke, A. D. Density-functional thermochemistry. IV. A new dynamical correlation functional and implications for exact-exchange mixing. *The Journal of chemical physics* **1996**, *104*, 1040–1046.
- [84] Perdew, J. P.; Ernzerhof, M.; Burke, K. Rationale for mixing exact exchange with density functional approximations. *The Journal of chemical physics* **1996**, *105*, 9982–9985.
- [85] Marques, M. A.; Vidal, J.; Oliveira, M. J.; Reining, L.; Botti, S. Density-based mixing parameter for hybrid functionals. *Physical Review B* **2011**, *83*, 035119.
- [86] Becke, A. D. Density-functional thermochemistry. III. The role of exact exchange. *The Journal of Chemical Physics* **1993**, *98*, 5648–5652.
- [87] Chen, Z.-y.; Yang, J.-l. The B3LYP hybrid density functional study on solids. *Frontiers of Physics in China* **2006**, *1*, 339–343.
- [88] Paier, J.; Marsman, M.; Kresse, G. Why does the B3LYP hybrid functional fail for metals? *The Journal of chemical physics* **2007**, *127*.
- [89] Dudarev, S. L.; Botton, G. A.; Savrasov, S. Y.; Humphreys, C.; Sutton, A. P. Electron-energy-loss spectra and the structural stability of nickel oxide: An LSDA+ U study. *Physical Review B* **1998**, *57*, 1505.
- [90] Anisimov, V. I.; Zaanen, J.; Andersen, O. K. Band theory and Mott insulators: Hubbard U instead of Stoner I. *Physical Review B* **1991**, *44*, 943.
- [91] Himmetoglu, B.; Floris, A.; De Gironcoli, S.; Cococcioni, M. Hubbard-corrected DFT energy functionals: The LDA+ U description of correlated systems. *International Journal of Quantum Chemistry* **2014**, *114*, 14–49.
- [92] Tolba, S. A.; Gameel, K. M.; Ali, B. A.; Almossalami, H. A.; Allam, N. K. The DFT+ U: Approaches, accuracy, and applications. *Density Functional Calculations-Recent Progresses of Theory and Application* **2018**, *1*, 5772.
- [93] Evarestov, R. A. *Quantum chemistry of solids: the LCAO first principles treatment of crystals*; Springer Science & Business Media, 2007; Vol. 153.
- [94] Spiegelman, F.; Tarrat, N.; Cuny, J.; Dontot, L.; Posenitskiy, E.; Martí, C.; Simon, A.; Rapacioli, M. Density-functional tight-binding: basic concepts and applications to molecules and clusters. *Advances in physics: X* **2020**, *5*, 1710252.
- [95] Elstner, M.; Seifert, G. Density functional tight binding. *Philosophical Transactions of the Royal Society A: Mathematical, Physical and Engineering Sciences* **2014**, *372*, 20120483.

- [96] Gaus, M.; Cui, Q.; Elstner, M. Density functional tight binding: application to organic and biological molecules. *Wiley Interdisciplinary Reviews: Computational Molecular Science* **2014**, *4*, 49–61.
- [97] Hafner, J.; Kresse, G. *Properties of Complex Inorganic Solids*; Springer, 1997; pp 69–82.
- [98] Kresse, G.; Furthmüller, J. Efficiency of ab-initio total energy calculations for metals and semiconductors using a plane-wave basis set. *Computational materials science* **1996**, *6*, 15–50.
- [99] Bloch, F. Quantum mechanics of electrons in crystal lattices. *Z. Phys* **1928**, *52*, 555–600.
- [100] Bylaska, E. J. *Annual Reports in Computational Chemistry*; Elsevier, 2017; Vol. 13; pp 185–228.
- [101] Kitchin, J. Modeling materials using density functional theory. *Boston, Free Software Foundation* **2008**,
- [102] Hafner, J. Ab-initio simulations of materials using VASP: Density-functional theory and beyond. *Journal of computational chemistry* **2008**, *29*, 2044–2078.
- [103] Garrity, K. F.; Bennett, J. W.; Rabe, K. M.; Vanderbilt, D. Pseudopotentials for high-throughput DFT calculations. *Computational Materials Science* **2014**, *81*, 446–452.
- [104] Brown, I. D. Bond valence theory. *Bond Valences* **2014**, 11–58.
- [105] Troullier, N.; Martins, J. L. Efficient pseudopotentials for plane-wave calculations. *Physical review B* **1991**, *43*, 1993.
- [106] Vanderbilt, D. Soft self-consistent pseudopotentials in a generalized eigenvalue formalism. *Physical review B* **1990**, *41*, 7892.
- [107] Blöchl, P. E. Projector augmented-wave method. *Physical review B* **1994**, *50*, 17953.
- [108] Blöchl, P. E.; Först, C. J.; Schimpl, J. Projector augmented wave method: ab initio molecular dynamics with full wave functions. *Bulletin of Materials Science* **2003**, *26*, 33–41.
- [109] Kresse, G.; Joubert, D. From ultrasoft pseudopotentials to the projector augmented-wave method. *Physical review b* **1999**, *59*, 1758.
- [110] Mortensen, J. J.; Hansen, L. B.; Jacobsen, K. W. Real-space grid implementation of the projector augmented wave method. *Physical review B* **2005**, *71*, 035109.
- [111] Hodak, M.; Wang, S.; Lu, W.; Bernholc, J. Implementation of ultrasoft pseudopotentials in large-scale grid-based electronic structure calculations. *Physical Review B* **2007**, *76*, 085108.
- [112] others,, *et al.* DFTB+, a software package for efficient approximate density functional theory based atomistic simulations. *The Journal of chemical physics* **2020**, *152*.

- [113] Bannwarth, C.; Caldeweyher, E.; Ehlert, S.; Hansen, A.; Pracht, P.; Seibert, J.; Spicher, S.; Grimme, S. Extended tight-binding quantum chemistry methods. *Wiley Interdisciplinary Reviews: Computational Molecular Science* **2021**, *11*, e1493.
- [114] others,, *et al.* Commentary: The Materials Project: A materials genome approach to accelerating materials innovation. *APL materials* **2013**, *1*.
- [115] Mikolajczyk, A.; Pinto, H.; Gajewicz, A.; Puzyn, T.; Leszczynski, J. Ab initio studies of anatase TiO₂ (101) surface-supported Au₈ clusters. *Current Topics in Medicinal Chemistry* **2015**, *15*, 1859–1867.
- [116] others,, *et al.* Enhanced photocatalytic properties of lanthanide-TiO₂ nanotubes: An experimental and theoretical study. *Applied Catalysis B: Environmental* **2017**, *205*, 376–385.
- [117] Gabriel, J. J.; Congo, F. Y. C.; Sinnott, A.; Mathew, K.; Allison, T. C.; Tavazza, F.; Hennig, R. G. Uncertainty Quantification for Materials Properties in Density Functional Theory with k-Point Density. *arXiv preprint arXiv:2001.01851* **2020**,
- [118] Pack, J. D.; Monkhorst, H. J. " Special points for Brillouin-zone integrations"—a reply. *Physical Review B* **1977**, *16*, 1748.
- [119] Birch, F. Finite elastic strain of cubic crystals. *Physical review* **1947**, *71*, 809.
- [120] Long, O. Y.; Gautam, G. S.; Carter, E. A. Evaluating optimal U for 3 d transition-metal oxides within the SCAN+ U framework. *Physical Review Materials* **2020**, *4*, 045401.
- [121] Grimme, S.; Bannwarth, C.; Shushkov, P. A robust and accurate tight-binding quantum chemical method for structures, vibrational frequencies, and noncovalent interactions of large molecular systems parametrized for all spd-block elements (Z= 1–86). *Journal of chemical theory and computation* **2017**, *13*, 1989–2009.
- [122] Ehlert, C.; Hamilton, I. P. Iron doped gold cluster nanomagnets: ab initio determination of barriers for demagnetization. *Nanoscale Advances* **2019**, *1*, 1553–1559.
- [123] Gong, X.-Q.; Selloni, A.; Dulub, O.; Jacobson, P.; Diebold, U. Small Au and Pt clusters at the anatase TiO₂ (101) surface: behavior at terraces, steps, and surface oxygen vacancies. *Journal of the American Chemical Society* **2008**, *130*, 370–381.
- [124] Vittadini, A.; Selloni, A. Small gold clusters on stoichiometric and defected TiO₂ anatase (101) and their interaction with CO: A density functional study. *The Journal of chemical physics* **2002**, *117*, 353–361.
- [125] Harnett-Caulfield, L.; Walsh, A. Assessment of interstitial potentials for rapid prediction of absolute band energies in crystals. *The Journal of Chemical Physics* **2021**, *155*.
- [126] Ramirez, I. G.; Varilla, L. A.; Montoya, J. A DFT study about the effects of exchange-correlation functional on the structural and electronic properties of Anatase. 2019.

- [127] Arrigoni, M.; Madsen, G. K. A comparative first-principles investigation on the defect chemistry of TiO₂ anatase. *The Journal of chemical physics* **2020**, *152*.
- [128] Araujo-Lopez, E.; Varilla, L. A.; Seriani, N.; Montoya, J. A. TiO₂ anatase's bulk and (001) surface, structural and electronic properties: A DFT study on the importance of Hubbard and van der Waals contributions. *Surface Science* **2016**, *653*, 187–196.
- [129] others,, *et al.* Comparative study of structural and electronic properties of TiO₂ at GGA and GGA+ U level. *Journal of Optoelectronics and Advanced Materials* **2014**, *16*, 117–122.
- [130] Khan, M.; Xu, J.; Chen, N.; Cao, W. Electronic and optical properties of pure and Mo doped anatase TiO₂ using GGA and GGA+ U calculations. *Physica B: Condensed Matter* **2012**, *407*, 3610–3616.
- [131] Badalov, S.; Bocchini, A.; Wilhelm, R.; Kozub, A.; Gerstmann, U.; Schmidt, W. Rutile, anatase, brookite and titania thin film from Hubbard corrected and hybrid DFT. *Materials Research Express* **2023**, *10*, 075501.
- [132] Rasul, S. M.; Saber, D. R.; Aziz, S. B. Role of Titanium replacement with Pd atom on band gap reduction in the anatase Titanium Dioxide: First-Principles calculation approach. *Results in Physics* **2022**, *38*, 105688.
- [133] Roldan, A.; Boronat, M.; Corma, A.; Illas, F. Theoretical confirmation of the enhanced facility to increase oxygen vacancy concentration in TiO₂ by iron doping. *The Journal of Physical Chemistry C* **2010**, *114*, 6511–6517.
- [134] Arlt, T.; Bermejo, M.; Blanco, M.; Gerward, L.; Jiang, J.; Olsen, J. S.; Recio, J. High-pressure polymorphs of anatase TiO₂. *Physical Review B* **2000**, *61*, 14414.
- [135] Sotoudeh, M.; Abbasnejad, M.; Mohammadzadeh, M. R. First principles study of hydrogen doping in anatase TiO₂. *The European Physical Journal-Applied Physics* **2014**, *67*, 30401.
- [136] Wu, X.; Holbig, E.; Steinle-Neumann, G. Structural stability of TiO₂ at high pressure in density-functional theory based calculations. *Journal of Physics: Condensed Matter* **2010**, *22*, 295501.
- [137] Kanoun, M. B.; Ahmed, F.; Awada, C.; Jonin, C.; Brevet, P.-F. Band gap engineering of Au doping and Au–N codoping into anatase TiO₂ for enhancing the visible light photocatalytic performance. *International Journal of Hydrogen Energy* **2024**, *51*, 907–913.
- [138] Iida, K.; Noda, M.; Ishimura, K.; Nobusada, K. First-principles computational visualization of localized surface plasmon resonance in gold nanoclusters. *The Journal of Physical Chemistry A* **2014**, *118*, 11317–11322.
- [139] Garcia-Toral, D.; Báez, R. M.; Sanchez S, J. I.; Flores-Riveros, A.; Cocolletzi, G. H.; Rivas-Silva, J. Encapsulation of Pollutant Gaseous Molecules by Adsorption on Boron Nitride Nanotubes: A Quantum Chemistry Study. *ACS omega* **2021**, *6*, 14824–14837.